The Abdus Salam
International Centre for Theoretical Physics

United Nations
Educational, Scientific and
Cultural Organization

IAEA
International Atomic Energy Agency

1936-23

Advanced School on Synchrotron and Free Electron Laser Sources and their Multidisciplinary Applications

7 - 25 April 2008

Small angle x-ray scattering
(Basic Aspects)

Aldo Craievich
University de Sao Paulo
Brazil

Small-Angle X–ray Scattering by Nanostructured Materials

Aldo Craievich
Institute of Physics, University of São Paulo craievich@if.usp.br

"When scientists have learned how to control the arrangement of matter at very small scale, they will see materials take an enormously richer variety of properties." R. Feymman (1959)

1.Basic introduction.

The description of the characteristics of the small-angle X-ray scattering by materials will be introduced trough the simple example of an optical diffraction experiment in which a visible light beam passes through a small hole of a few microns on an opaque or semi-opaque mask. This experiment can be performed using a simple laser source, as those commonly utilized as a pointer in class-rooms (wavelength $\lambda \approx 0.65$ μm). What we may expect to see in a flat screen located at a distance D much larger than λ (say D=5m) from the mask? (Fig.1a). Classical physical optics tells us that a isotropic diffuse spot should be observed, centered in the intersection of the transmitted beam with the screen. Since the spot has a circular symmetry, the scattering intensity is a function only of the scattering angle ε or of the distance on the screen defined by x ($x \approx \varepsilon . D$). The scattering intensity function, $I_1(\varepsilon)$, exhibits a maximum at $\varepsilon=0$ and its half maximum intensity width, $\Delta\varepsilon$, increases for decreasing hole sizes. These effects are qualitatively illustrated in Fig. 1b, 1c and 1d, which display a series of three schematic profiles of the light scattering intensity produced by holes of different sizes.

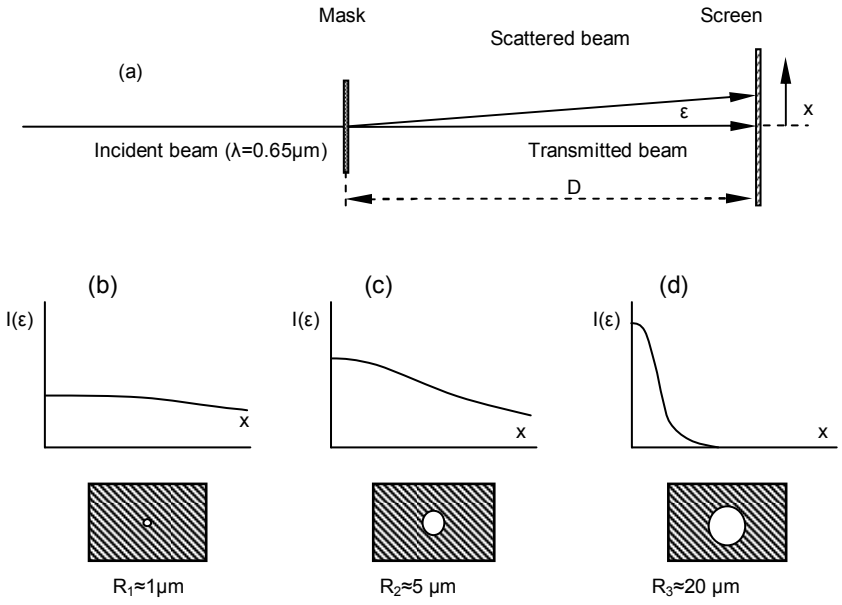

Fig. 1: (a) Setup of an experiment of small angle light scattering. (b), (c) and (d) are schematic intensity curves corresponding to circular holes of different sizes.

In practice, the scattering intensity produced by a single hole is very weak and therefore the masks that are used in actual experiments contain many holes. How the fact of having a number of holes, instead of only one, may affect the profile of the scattered intensity? In order to answer this question, the relevant features of the scattering intensity produced by different types of masks, containing a number of identical circular holes, arranged in different ways, will be described.

(i) Randomly located holes (2D ideal gas structure, Fig. 2a).

The randomness condition can only be approximately fulfilled if the holes are very far apart from each other. A (very) dilute set of N randomly located holes produces a scattering intensity simply given by $I(\varepsilon)= N.I_1(\varepsilon)$. This result implies that the hole positions are completely uncorrelated and, consequently, the total scattering intensity is the sum of the individual intensities; i. e. no interference between wavelets generated by different holes occurs.

(ii)Holes with short range spatial correlation (2D liquid-like structure, Fig. 2b).

The scattered wavelet produced by each hole interferes with the others and thus the simple equation $I(\varepsilon)= NI_1(\varepsilon)$ is not longer obeyed. The interference effects due to the spatial correlation in hole positions are accounted for by the "structure function" $S(\varepsilon)$, so that $I(\varepsilon)=NI_1(\varepsilon)S(\varepsilon)$. The structure function for a set of holes with short-range order is different from 1 at small scattering angles and tends to 1 at high angles.

(iii)Periodically arranged holes (2D crystal-like structure, Fig. 2c).

In this case, for particular values of the angle ε ($\varepsilon=\varepsilon_n$), the wavelets corresponding to the scattering produced by all holes are in phase. Thus the total scattering amplitude is $A(\varepsilon_n)=NA_1(\varepsilon_n)$, where A_1 refers to the amplitude produced by each hole, and $A(\varepsilon\neq\varepsilon_n)=0$. The total intensity, $I(\varepsilon)=|A(\varepsilon)|^2$, is then given by $I(\varepsilon=\varepsilon_n)=N^2I_1(\varepsilon_n)$ and $I(\varepsilon\neq\varepsilon_n)=0$. The structure function S(q) is composed of narrow peaks with non zero values (S(q)=N) for well-defined angles, $\varepsilon\approx\varepsilon_n$, which only depend on the geometry of the arrangement of holes. This is analogous to the effects described by the well-known Bragg law corresponding to the X-ray diffraction by 3D crystals.

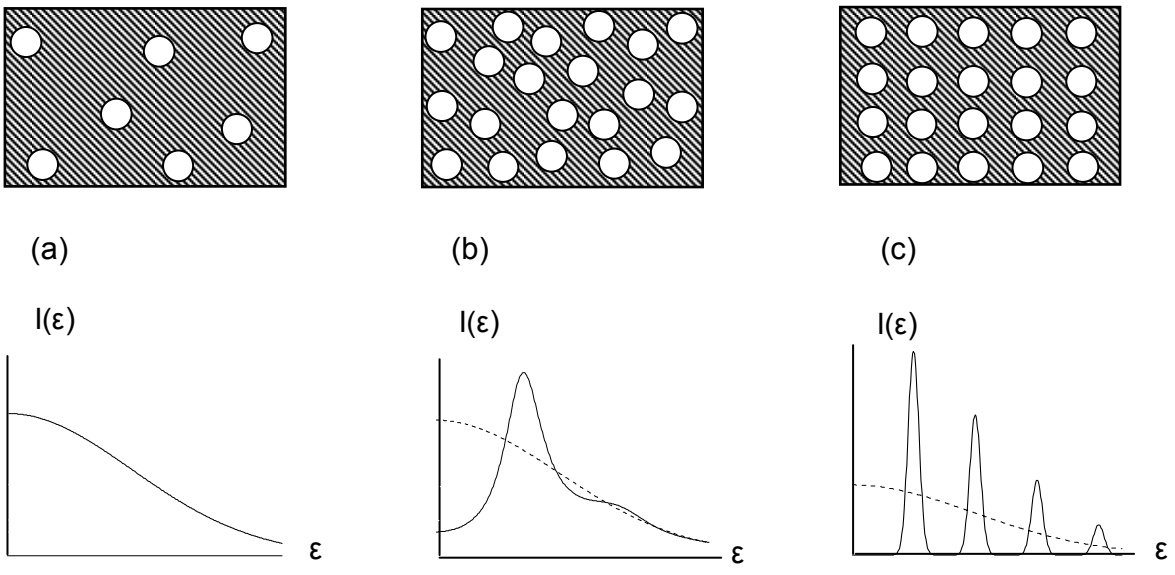

Fig. 2: Schematic masks and corresponding light scattering intensity for (a) a gas-like (dilute) set of holes, (b) a liquid-like (concentrated) set of holes with short range spatial order, and (c) a crystal-like concentrated set of holes with long range spatial order.

All previous considerations also apply to the case where, instead of circular holes on a plane, we have spheres located in the three dimensional space.

Elastic scattering of X-rays by nanostructured materials is a phenomenon similar to the described scattering of visible light by a mask with micrometric holes. A 3D analogous of the mask may be a material containing nano-pores or an arrangement of nano-clusters. The individual pores or clusters play the same role in X-ray scattering experiments as the microscopic holes in the mask. The small-angle scattering is produced by electron density heterogeneities at nanometric level such as, in the mentioned example, the clusters or pores. As it will be seen, the small-angle X-ray scattering technique provides relevant information about the shape, size, size distribution and spatial correlation of heterogeneities in electron density.

The properties of nanostructured materials are often very different from those of the same materials in bulk state. They depend not only on the structure at atomic scale but also, and often strongly, on the structure at nanometric scale. For example, relatively small variations in the shape and/or size of metal or semiconductor nanocrystals embedded in a glass matrix induce dramatic changes in the optical properties of these nanocomposites. This example illustrates why the characterization of materials at a nanometric scale is a relevant issue for materials scientists. Furthermore, it will be demonstrated along this chapter that small-angle scattering technique actually is a very useful technique for structural characterizations at a nanometric scale.

2. Small-angle X-ray scattering by nanostructured materials with an arbitrary structure.

The basic process of the scattering of X-ray by materials is the photon-electron interaction. As it will be seen, the X-ray scattering intensity produced by any material varies with the scattering angle and the characteristics of this function directly depend on the electron density function $\rho(\vec{r})$. The electron density function contains all the information that is practically needed in order to fully describe the material structure.

X-ray scattering by materials is named as "small-angle X-ray scattering" (or SAXS) when the measurements are confined to angles smaller than ~10 degrees. These measurements provide relevant information if the average radius of the clusters and/or inter-cluster distances are about 5-500 times the wavelength used in the experiment (typically λ=1.5 Å). On the contrary, if the objects are very large as compared to the X-ray wavelength (with sizes above say 1μm), the scattering intensity is concentrated within a extremely small angle domain, close to the direct X-ray beam, that is hidden by the narrow direct beam stopper placed close to the detector. On the other hand, the X-ray scattering at small-angles does not contain any information about the oscillations in electron density associated to the atomic nature of the structure. This information can only be found at wide scattering angles. These comments imply that the window of sizes that are probed by the small-angle X-ray scattering technique ranges from about 10 Å up to 1000 Å.

The experiments of small-angle X-ray scattering are usually performed in transmission mode. Thus, for a wavelength much larger than 1.5 Å, photons would be strongly absorbed by the sample. On the other hand, if a much smaller wavelength is used, the scattering would concentrate at too small angles making practical analyses difficult. Therefore, most of the SAXS experiments reported in the literature are performed using X-ray wavelengths ranging from 0.7 to 1.7 Å .

2.1. Scattering of x-rays by an electron.

The elastic scattering produced by an isolated electron was derived by Thompson. The amplitude of the wave scattered by each electron has a well-defined phase relation with the amplitude of the incident wave, thus making interference effects possible. In the particular case of a non-polarized X-ray beam, such as those produced by a classical X-ray tube, the scattering power of one electron per solid detection angle, I_e, is a function of the angle between the incident and the scattered beam, 2θ:

$$I_e(2\theta) = I_0 r_e^2 (\frac{1+\cos^2 2\theta}{2}) \quad (1)$$

where I_0 is the intensity of the incident beam (power/cm^2) and r_e is the classical radius of the electron, $r_e^2 = 7.90.10^{-26} cm^2$. For small scattering angles $\cos^2 2\theta \approx 1$ so as the scattering intensity per electron is simply given by

$$I_e(2\theta) = I_0 r_e^2 \quad (2)$$

If a crystal monochromator is inserted in the beam path, the X-ray beam becomes partially polarized and Eq (1) does not longer hold but, at small angles, Eq. (2) remains still valid as a good approximation.

In addition to the coherent or elastic X-ray scattering, the electrons also produce inelastic Compton scattering. Compton scattering being incoherent (i. e. no phase relationship exists between incident and scattered waves), the scattered waves do not interfere and thus the scattering intensity is not modulated by structure correlation effects. On the other hand, since the intensity of Compton scattering within the small-angle range is weak, its contribution can in practice be neglected.

As the scattering intensity per electron, I_e, will later appear in all the equations defining the scattering intensity produced by materials, it will be omitted for brevity.

2.2 General equations.

The scattering amplitude and intensity related to the elastic interaction between a narrow monochromatic X-ray beam – with a wavelength λ - and an arbitrary material are functions of the scattering vector $\vec{q}$, which is usually defined as the difference between the wave-vectors $\vec{Q}$ and $\vec{Q}_0$ - both with modulus equal to $2\pi/\lambda$ - having the directions of the scattered and incident beam, respectively (Fig. 3). Since $\vec{Q}$ and $\vec{Q}_0$ are proportional to the linear momentum of the scattered and incident photons ($\vec{p} = h\vec{Q}$, h being the Plank constant), respectively, the difference $\vec{q} = \vec{Q} - \vec{Q}_0$ is proportional to the photon momentum transfer, $\Delta\vec{p} = h\vec{q}$, associated to the photon scattering process. As illustrated in Fig. 3, the modulus of $\vec{q}$ is 4π sin θ/λ, θ being half the scattering angle.

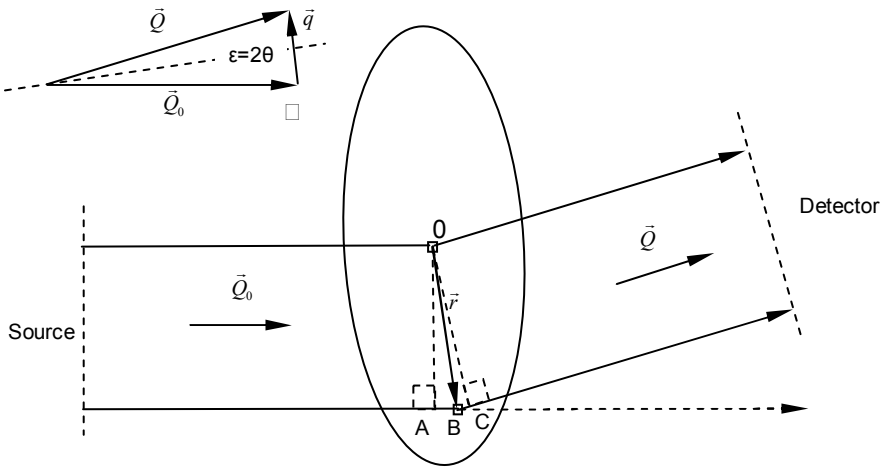

Fig. 3: X-ray beam paths from the source to the detector, both elements located far away from the sample. The segment $\overline{AB} + \overline{BC}$ is the optical path difference from which the phase shift is determined.

The basic theory of X-ray scattering by a 3D material whose structure is defined by an electron density function $\rho(\vec{r})$ will be presented. The electron density function may represent the *high resolution* structure – including its successive more or less high peaks corresponding to single atoms of different types - or only the *low resolution* structure – exclusively accounting for the nanometric features of the material. A low resolution electron density function describes, for example, the shape and size of nano-precipitates embedded in a solid or liquid matrix but not their detailed crystallographic structure.

The amplitude of the X-ray wavelet produced by the scattering of the electrons located inside a particular volume element dv is

$$dA(q) = A_e \rho(\vec{r}) dv . e^{i\Delta\varphi} \tag{3}$$

where A_e is the amplitude of the wavelet scattered by one electron and $\rho(\vec{r})dv$ is the number of electrons in the volume element dv. $A_e \rho(\vec{r})dv$ is the modulus of the amplitude of the scattered wavelet and $e^{i\Delta\varphi}$ is a phase factor that accounts for the phase difference, $\Delta\varphi$, between the wavelets associated to the scattering by electrons in a volume element located at $\vec{r} = 0$ and in another arbitrary volume element dv. The amplitude A_e will be set equal to 1 in the following equations for brevity.

The optical path difference, Δs, associated with two wavelets corresponding to the X-ray scattering by electrons inside a volume element at $\vec{r} = 0$ and another at $\vec{r}$ (Fig. 3) is

$$\Delta s = \overline{AB} + \overline{BC} = -(\hat{Q}_0 . \vec{r} - \hat{Q} . \vec{r}) \tag{4}$$

where $\hat{Q}_0$ and $\hat{Q}$ are unit vectors in the directions defined by $\vec{Q}_0$ and $\vec{Q}$, respectively. Thus the phase shift defined as $\Delta\varphi = 2\pi \Delta s / \lambda$ becomes

$$\Delta\varphi = -2\pi \frac{(\hat{Q} - \hat{Q}_0).\vec{r}}{\lambda} = -(\vec{Q} - \vec{Q}_0).\vec{r} = -\vec{q}.\vec{r} \tag{5}$$

Substituting $\Delta\varphi$ in Eq. (3) and integrating over the whole volume V, the total scattering amplitude (setting A_e=1) is given by

$$A(\vec{q}) = \int_V \rho(\vec{r}) e^{-i\vec{q}.\vec{r}} dv \tag{6}$$

This is the amplitude of the scattered waves under the assumptions of the kinematical theory of X-ray scattering disregarding multiple scattering and absorption effects [1]. Eq. (6) indicates that $A(\vec{q})$ simply is the Fourier transform of the electron density $\rho(\vec{r})$. The amplitude $A(\vec{q})$ is defined in the reciprocal or Fourier space ($\vec{q}$ space) and is a complex function, i. e. its value is specified by the real and imaginary parts or, alternatively, but the modulus and phase.

Inversely, the electron density $\rho(\vec{r})$ can mathematically be obtained by a Fourier transformation of the amplitude function $A(\vec{q})$:

$$\rho(\vec{r}) = \frac{1}{(2\pi)^3} \int A(\vec{q}) e^{i\vec{q}.\vec{r}} dv_q \tag{7}$$

Taking into account the mathematical properties of the Fourier transformation, we know that the electron density, $\rho(\vec{r})$, defining the *high-resolution* material structure (i. e. the atomic configuration), can only be determined if the complex function $A(\vec{q})$ (modulus and phase) is known over a large volume in $\vec{q}$ space. On the other hand, if the amplitude $A(\vec{q})$ is known only within a rather small volume in $\vec{q}$ space close to $\vec{q}$=0, Eq (7) yields the *low-resolution* features of the structure.

Nevertheless, a fundamental difficulty arises in the analysis of the results of scattering experiments because the X-ray detectors count photons, i.e. what is experimentally determined is the scattering intensity $I(\vec{q})$ and not the complex amplitude $A(\vec{q})$. Since $I(\vec{q}) = A(\vec{q}).A(\vec{q})^* = |A(\vec{q})|^2$, the square root of the measured $I(\vec{q})$ function provides only the modulus of the scattering amplitude:

$$|A(\vec{q})| = [I(\vec{q})]^{1/2} \tag{8}$$

Thus Eq. (7) cannot be directly applied to derive neither the electron density function $\rho(\vec{r})$ and, consequently, nor the material structure. This is the known *phase problem* that crystallographers and materials scientists always face when they try to determine the detailed material structure from the results of X-ray scattering experiments.

A procedure that can be applied to determine simple low resolution structures, circumventing the phase problem, is to begin with a proposed structure model providing an initial, guessed, electron density function $\rho(\vec{r})$. The scattering amplitude is determined using Eqs. (6) and then the trial intensity $I(\vec{q}) = |A(\vec{q})|^2$ is compared to the experimental intensity. The use of ad-hoc iterative computer packages allows for many and fast modifications of the structure model, until a good fit of the calculated function to the experimental curve is achieved. This procedure is currently applied to the determination of the low-resolution structure (envelope function) of proteins in solution.

Another procedure that is often applied to the study of materials transformations starts from the theoretical calculation of the scattering functions I(q) that are predicted from basic thermodynamic or statistical models and is followed by their direct comparison with the experimental results. This procedure is generally applied to verify the correctness of newly proposed theoretical models for different structural transformations. This topic will be discussed in section 7.

Since the amplitude of the scattered wave, $A(\vec{q})$, cannot be experimentally determined, it seems that it would be useful to deduce a relationship connecting the scattered intensity defined in reciprocal space, $I(\vec{q})$, to a function related to the structure in real space, both functions related by a Fourier transformation.

The electron density $\rho(\vec{r})$ can be written as the sum of an average density ρ_a and its local deviations defined by $\Delta\rho(\vec{r})$:

$$\rho(\vec{r}) = \rho_a + \Delta\rho(\vec{r}) \tag{9}$$

Substituting this form for $\rho(\vec{r})$ in Eq. (6) the scattering amplitude becomes

$$A(\vec{q}) = \int_V \rho_a e^{-i\vec{q}.\vec{r}}\, dv + \int_V \Delta\rho(r) e^{-i\vec{q}.\vec{r}}\, dv \tag{10}$$

For a macroscopic sample (with a very large volume compared to the X-ray wavelength), the first integral yields non-zero values only over an extremely small q range, close to q=0, that is not reached in typical SAXS experiments. Thus the scattering amplitude $A(\vec{q})$ over the accessible $\vec{q}$ range is given by

$$A(\vec{q}) = \int_V \Delta\rho(\vec{r}) e^{-i\vec{q}.\vec{r}}\, dv \tag{11}$$

so as the scattering intensity $I(\vec{q})$ becomes

$$I(\vec{q}) = \int_V \int_V \Delta\rho(\vec{r}_1)\Delta\rho(\vec{r}_2).e^{-i\vec{q}.(\vec{r}_1-\vec{r}_2)}.dv_1 dv_2 \tag{12}$$

Making $\vec{r}_1 - \vec{r}_2 = \vec{r}$, Eq. (12) can be written as

$$I(\vec{q}) = \int_V \int_V \Delta\rho(\vec{r}_2 + \vec{r})\Delta\rho(\vec{r}_2).e^{-i\vec{q}.\vec{r}}\, dv_2 dv \tag{13}$$

or

$$I(\vec{q}) = V\int_V \gamma(\vec{r}) e^{-i\vec{q}.\vec{r}}\, dv \tag{14}$$

where

$$\gamma(\vec{r}) = \frac{1}{V}\int_{V'} \Delta\rho(\vec{r}').\Delta\rho(\vec{r}'+\vec{r}).dv' = \overline{\Delta\rho(\vec{r}').\Delta\rho(\vec{r}'+\vec{r})} \tag{15}$$

the bar indicating the average over the analyzed sample volume (*).

The function $\gamma(\vec{r})$ - named correlation function [2] - is the volume average of the product of $\Delta\rho(\vec{r})$ in two volume elements dv located at $\vec{r}_1$ and $\vec{r}_2$ connected by a vector $\vec{r}$. The function $\gamma(\vec{r})$ can directly be determined from an experimental scattering intensity function $I(\vec{q})$ by a Fourier transformation:

$$\gamma(\vec{r}) = \frac{1}{(2\pi)^3 V}\int I(\vec{q}).e^{i\vec{q}.\vec{r}}\, dv_q \tag{16}$$

The correlation function $\gamma(\vec{r})$ is related to the structure (i. e. to the $\rho(\vec{r})$ electron density function) and can easily be determined, provided $\rho(\vec{r})$ is known, by applying Eq. (15). But, inversely, from a known $\gamma(\vec{r})$ function, $\rho(\vec{r})$ cannot generally be unambiguously inferred.

2.3. Small-angle scattering by a macroscopically isotropic system

In the particular case of a isotropic system, the correlation function is independent of the direction of the vector $\vec{r}$, i. e. $\gamma(\vec{r})$ can be written as $\gamma(r)$. Consequently, the scattering intensity is also isotropic. In this case the function $e^{-i\vec{q}.\vec{r}}$ is replaced in Eq. (14) by its spherical average < >:

$$\left\langle e^{-i\vec{q}.\vec{r}} \right\rangle = \frac{\sin qr}{qr} \tag{17}$$

(*) Three types of averages will be mentioned along this chapter, (i) $\overline{f(\vec{r})}$: spatial average over the whole object or irradiated sample volume ; (ii) $< f(\vec{r}) >$: angular average for all object orientations; and (iii) {f(R)}: average over the radius distribution for spherical objects.

Thus, for isotropic systems, Eq. (14) becomes

$$I(q) = V\int_0^\infty 4\pi r^2 \gamma(r)\frac{sinq.r}{q.r}dr \tag{18}$$

and Eq. (15) is given by

$$\gamma(r) = \frac{1}{(2\pi)^3 V}\int_0^\infty 4\pi q^2 I(q)\frac{sinq.r}{q.r}dq \tag{19}$$

From Eq. (15) the correlation function for r=0 is

$$\gamma(0) = \frac{1}{V}\int_V \Delta\rho(\vec{r}).\Delta\rho(\vec{r}).dv = \overline{\Delta\rho(\vec{r})^2} \tag{20}$$

so as implying that $\gamma(0)$ is equal to the spatial average of the square electron density fluctuations over the whole volume. Taking in Eq. (19) the limit for r→0, we have sin(qr)/qr→1 and thus the integral of the scattering intensity in reciprocal space $Q = \int_0^\infty 4\pi q^2 I(q)dq$ becomes equal to $(2\pi)^3 V\gamma(0)$. From Eq. (19) and (20) one finds that $\gamma(0)$, Q and $\overline{\Delta\rho(\vec{r})^2}$ are related by

$$\gamma(0) = \frac{1}{(2\pi)^3 V}Q = \overline{\Delta\rho(\vec{r})^2} \tag{21}$$

Thus, the integral of the scattering intensity in reciprocal space, Q, is proportional to the spatial average of the square electron density fluctuations over the whole sample volume $\overline{\Delta\rho(\vec{r})^2}$.

3. Small-angle scattering by a isotropic two-electron density structure

3.1 The characteristic function

The X-ray scattering by isotropic nanostructured systems composed of two well-defined homogeneous phases will now be described. The volume fractions of the two phases are defined by φ_1 and φ_2 and the constant electron density within each of them by ρ_1 and ρ_2, respectively (Fig. 4a and 4b). The correlation function γ(r) for a isotropic two-electron density model can be expressed as [2, 3]

$$\gamma(r) = \varphi_1\varphi_2(\rho_1 - \rho_2)^2\gamma_0(r) \tag{22}$$

where $\gamma_0(r)$ is a isotropic function - named as characteristic function - that only depends on the geometrical configuration of the two-phases.

The characteristic function $\gamma_0(r)$ has a precise meaning for the particular case of a single isolated nano-object (that may be anisotropic) with a volume V. In this case $\gamma_0(\vec{r})$ is

$$\gamma_0(\vec{r}) = \frac{\tilde{V}(\vec{r})}{V} \tag{23}$$

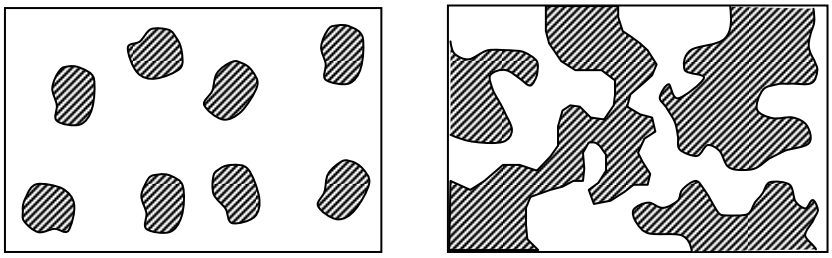

(a) (b)

Fig. 4: Schematic examples of two-electron density systems. (a) A set of isolated objects with a constant electron density embedded in a homogeneous matrix. (b) Continuous and interconnected phases, both with a constant electron density.

$\tilde{V}(\vec{r})$ being the volume common to the nano-object and its "ghost" displaced by a vector $\vec{r}$, as illustrated in Fig. 5. If the system is composed of many isolated nano-objects with random orientations, the isotropic characteristic function is given by $\gamma_0(r) = \langle \gamma_0(\vec{r}) \rangle$.

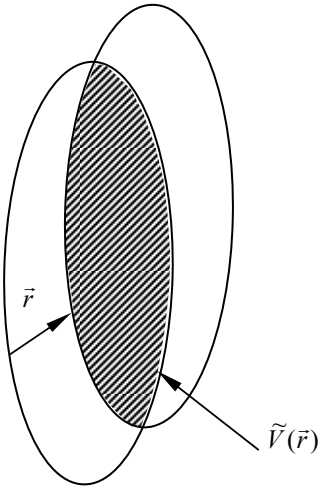

Fig. 5: Colloidal particle and its "ghost" displaced by a vector $\vec{r}$.

Taking into account Eq. (22), Eqs. (18) and (19) can, respectively, be rewritten as

$$I(q) = V\varphi_1\varphi_2(\rho_1 - \rho_2)^2 \int_0^\infty 4\pi r^2 \gamma_0(r) \frac{sinq.r}{q.r} dr \tag{24}$$

and

$$\gamma_0(r) = \frac{1}{(2\pi)^3 V\varphi_1\varphi_2(\rho_1 - \rho_2)^2} \int_0^\infty 4\pi q^2 I(q) \frac{sinq.r}{qr} dq \tag{25}$$

The characteristic function $\gamma_0(r)$ can be defined for any type of two-density systems including those with bicontinuous geometries. It can be demonstrated that $\gamma_0(r)$ exhibits a asymptotic behavior within the small r range - that is independent of the detailed configuration of the interfaces - given b [1]

$$\gamma_0(r) = 1 - \frac{S/V}{4\varphi_1\varphi_2} r + \ldots \qquad r \to 0 \qquad (26)$$

where S is the total interface area of the two-density system within the sample volume V.

3.2. The integral of the scattering intensity in reciprocal space

From the expression for $\gamma_0(r)$ (Eq. 25) for r=0 and taking into account that $\gamma_0(0)= 1$ (Eq. 26), the integral of the scattering intensity in reciprocal space, Q, can be written as

$$Q = \int_0^\infty 4\pi q^2 I(q) dq = (2\pi)^3 V \varphi_1 \varphi_2 (\rho_1 - \rho_2)^2 \qquad (27)$$

Thus the integral Q only depends on the electron density contrast factor $(\rho_1 - \rho_2)^2$ and on the volume fractions occupied by both phases, but not on their detailed geometrical configuration. For example, in structural transformations that maintain constant the electron densities and the volume fractions of both phases, even thought the structure and, consequently, the shape of the scattering intensity curves vary, the integral Q remains constant. The integral Q (or $Q/4\pi$) is often named as Porod invariant. Examples of transformations that occur without significantly affecting the value of the integral Q are the processes of growth of nano-clusters by coarsening or coalescence.

3.3. Asymptotic behavior of scattering curves at high q. Porod law

The general properties of Fourier analysis tell us that the asymptotic trend, at high q, of the scattering intensity I(q) is connected to the behavior of the $\gamma(r)$ function at small r. Taking into account Eq. (26), the correlation function $\gamma(r)$ can be approximated at small r by

$$\gamma(r) = \varphi_1\varphi_2(\rho_1 - \rho_2)^2 \left(1 - \frac{S}{4V\varphi_1\varphi_2} r\right) \qquad (28)$$

This relation implies that the value of the first derivative of $\gamma(r)$ at r=0 is

$$\gamma'(0) = -(\rho_1 - \rho_2)^2 \frac{S}{4V} \qquad (29)$$

Moreover, Eq. (18) can be rewritten as

$$I(q) = -\frac{4\pi V}{q} \frac{d}{dq} \int_0^\infty \gamma(r) \cos(qr) dr \qquad (30)$$

A first integration by parts of the integral in Eq. (30) yields

$$\int_0^\infty \gamma(r) \cos(qr) dr = \left. \frac{\gamma(r) sin(qr)}{q} \right|_{r=0}^{\infty} - \frac{1}{q} \int_0^\infty \gamma'(r) . sin(qr) dr \qquad (31)$$

Since $\gamma(r) \to 0$ as $r \to \infty$ and $\sin(qr) \to 0$ as $r \to 0$, the first term is equal to zero. The remaining one can be written as

$$-\frac{1}{q}\int_0^\infty \gamma'(r).sin(qr)dr = \frac{\gamma'(r)\cos(qr)}{q^2}\Big|_{r=0}^{\infty} - \frac{1}{q^2}\int_0^\infty \gamma''(r)\cos(qr)dr = -\frac{\gamma'(0)}{q^2} - \frac{1}{q^2}\int_0^\infty \gamma''(r)\cos(qr)dr \quad (32)$$

In Eq. (32), provided γ''(r) is a continuous function, the second term decreases for q→∞ faster than the first one. It has been shown that this condition is always fulfilled unless the interface surface contains portions that are each other parallel, as it happens in the case of spheres and cylinders [4]. Assuming this condition is met, Eq. 30 becomes

$$I(q) = -\frac{4\pi}{q}\frac{d}{dq}\left[-\frac{\gamma'(0)}{q^2}\right] = -\frac{8\pi\gamma'(0)}{q^4} \quad (33)$$

and, reminding that γ′(0) is given by Eq. (29), the asymptotic behavior of I(q) is given by

$$I(q) = \frac{2\pi(\rho_1 - \rho_2)^2.S}{q^4} \qquad q\to\infty \quad (34)$$

Eq. (34), named as Porod law, holds for most types of isotropic two-electron density systems with sharp interfaces. This equation is often applied to the study of disordered porous materials and to other two-phase systems whose relevant structure feature is the surface area.

The behavior of I(q) at high q is analyzed using a Porod plot ($I(q)q^4$ versus q^4) that is expected to be asymptotically constant. This plot allows one to determine (i) the asymptotic value of $I(q)q^4$ and, from it, the interface surface area and (ii) eventual positive or negative deviations from Porod law. Density fluctuations in the phases produce a deviation of Porod's law evidenced by a positive slope of the linear part of Porod' s plots and a smooth (not sharp) transition in the electron density between the two phases leads to a negative slope [5].

The determination of the interface surface area using Eq. (34) requires the measurement of the scattering intensity in absolute units (section 8.2.3). If the scattering intensity is only known in relative scale, it is still possible to obtain the surface area using together Porod' s law (Eq. 34) and the Porod invariant (Eq. 27). The surface area per unit volume is then determined from

$$\frac{S}{V} = 4\pi^2\varphi_1\varphi_2\frac{[I(q)q^4]_{q\to\infty}}{Q} \quad (35)$$

For the very particular case of identical spherical or cylindrical nano-objects, the oscillations remain, even for very high q values. In these cases, the Porod plot asymptotically show undamped oscillations superposed to a constant plateau. From the features of such oscillations, it is possible to determine the distance between the parallel portions of the interface [4]. However, if the spherical or cylindrical nano-objects exhibit a wide size distribution, the mentioned oscillations smear out.

For anisotropic two-electron density systems, Ciccariello et al. [6] demonstrated that the Porod law still holds along all q directions but, in this case, the parameter S (Eq. 34 and 35) has a different meaning. Porod' s law applies to either, dilute or concentrated systems of isolated nano-objects, provided they are not very thin sheets or very narrow cylinders; in these particular cases the asymptotic intensity is proportional to $1/q^2$ and $1/q$, respectively [7].

4. Small-angle scattering of a dilute system of isolated nano-objects. General equations

4.1 The characteristic function for a single isolated object

In the particular case of a dilute and isotropic system composed of a large number, N, of randomly oriented and isolated nano-objects, all having the same shape and size, the total intensity is

$$I(q) = \sum_{i=1}^{N} [I_1(\vec{q})]_i = N\left[\frac{1}{N}\sum_{i=1}^{N} [I_1(\vec{q})]_i\right] \tag{36}$$

The intensity I(q) is N times the individual intensity $I_1(q)$ produced by one nano-object of volume V_1 averaged for all orientations:

$$I(q) = N\langle I_1(\vec{q})\rangle \tag{37}$$

Thus one can derive the scattering intensity, $\langle I_1(q)\rangle$, from the characteristic function for a single object averaged for all orientations, $\gamma_0(r) = \langle \gamma_0(\vec{r})\rangle$, both functions being connected through a Fourier transformation (Eq. 19). The spherically averaged characteristic function, $\gamma_0(r)$, for a single isolated and homogeneous object with an electron density ρ_1 embedded in an also homogeneous matrix with a density ρ_0, has the following properties [1]:

i) It can be expressed as

$$\gamma_0(r) = \gamma(r)/\left[N(V_1/V)(\rho_1 - \rho_0)^2\right] \tag{38}$$

ii) It is a positive and decreasing function.

iii) The asymptotic behavior at low r can be approximated by

$$\gamma_0(r) = 1 - (S_1/4V_1)r \tag{39}$$

where S_1 and V_1 are the object surface area and volume, respectively.

iii) $\gamma_0(r)=0$ for $r>D_{max}$, D_{max} being the maximum diameter of the scattering object.

iv) The volume integral of $\gamma_0(r)$ is $\int_0^{D_{max}} 4\pi . r^2 \gamma_0 dr = V_1$

v) The scattering intensity is given by

$$I_1(q) = \langle I_1(\vec{q})\rangle = (\rho_1 - \rho_0)^2 V_1 \int_0^{D_{max}} 4\pi r^2 \gamma_0(r) \frac{sinq.r}{q.r} dr \tag{40}$$

The properties of $\gamma_0(r)$ for a spherically averaged single object, listed above, were derived from the general characteristics of the $\gamma_0(r)$ function for arbitrary isotropic two-electron density systems (section 3), assuming the basic conditions inherent to an isolated nano-object immersed in a macroscopic volume, namely $\varphi_1 = NV_1/V$ and $\varphi_2 \approx 1$.

4.2. Scattering intensity at q=0

From Eq. (40) and taking into account the property (iv) mentioned in the preceding section, the extrapolated value to q=0 of the scattering intensity produced by a single nano-object and by a dilute set of N identical objects are, respectively, given by

$$I_1(0) = (\rho_1 - \rho_0)^2 V_1^2 \quad \text{(a)} \qquad I(0) = N(\rho_1 - \rho_0)^2 V_1^2 \quad \text{(b)} \qquad (41)$$

The differences in the X-ray path length in the forward scattering direction (q=0), associated to the wavelets scattered by each electron inside a nano-object, is zero. Consequently, all of them scatter in phase so that the amplitude is $A_1(0) = \Delta n$, Δn being the excess in electron number inside the objects with respect to the matrix. Thus the scattering intensity results $I_1(0)=[A_1(0)]^2=\Delta n^2$ which is equivalent to Eq. (41a).

The invariant Q (Eq. 27), for a dilute set of nano-objects of same size and shape, becomes $Q = 8\pi^3 N(\rho_1 - \rho_0)^2 V_1$. Thus the volume V_1 can be derived, regardless the object shape, from the quotient I(0)/Q as follows

$$V_1 = 8\pi^3 \frac{I(0)}{Q} \qquad (42)$$

4.3. Asymptotic trend of the scattering intensity at small q. Guinier law

4.3.1. Dilute and monodispersed set of identical nano-objects

The scattering intensity produced by a dilute set of N identical and randomly oriented nano-objects is N times the intensity scattered by one object averaged for all orientations, $I_1(q)$, (Eq. 40) so that

$$I(q) = N(\rho_1 - \rho_0)^2 V_1 \int_0^{D_{\max}} 4\pi r^2 \gamma_0(r) \frac{sinqr}{qr} dr \qquad (43)$$

The $\sin qr/qr$ factor in Eq. (43) can be substituted, for small q, by its approximated form $(\sin qr/qr) = 1 - (q^2 r^2/6) + \ldots$. Keeping only the two first terms of the series, Eq. (43) becomes

$$I(q) = N(\rho_1 - \rho_0)^2 V_1 \int_0^{D_{\max}} 4\pi r^2 \gamma_0(r).(1 - \frac{q^2 r^2}{6})]dr \qquad (44)$$

Eq. (44) can be rewritten as

$$I(q) = N(\rho_1 - \rho_0)^2 V_1^2 \left[1 - \frac{q^2}{6}\frac{1}{V_1}\int_0^{D_{\max}} 4\pi r^4 \gamma_0(r) dr\right] = N(\rho_1 - \rho_0)^2 V_1^2 \left[1 - \frac{q^2}{3} R_g^2\right] \qquad (45)$$

where

$$R_g = \left[\frac{1}{2V_1}\int_0^{D_{\max}} 4\pi r^4 \gamma_0(r) dr\right]^{1/2} \qquad (46)$$

R_g being the radius if gyration with respect to the "center of mass" of the electron density function that is defined for a homogeneous object as

$$R_g = \left[\frac{1}{V_1} \int_{V_1} r^2 dv \right]^{1/2} = \overline{r^2} \qquad (47)$$

Since the parabolic shape of I(q) within the small q range (Eq. 45) is also described by the first two terms of the series representing a Gaussian function, the scattering intensity in the limit of small q can be written as

$$I(q) = N(\rho_1 - \rho_0)^2 V_1^2 . e^{-\frac{R_g^2 q^2}{3}} \qquad (48)$$

that is the well-known Guinier law [8]. Guinier plots of the scattering intensity (log I versus q^2) are commonly used in order to derive the radius of gyration R_g from the slope of the straight line that is experimentally observed within a more or less wide q range at small q. This linear plot is also used to determine extrapolated scattering intensity I(0).

Guinier law also holds for dilute sets of objects with arbitrary and variable electron density $\rho(\vec{r})$ embedded in a homogeneous matrix with density ρ_0. In this case the radius of gyration R_g is defined as

$$R_g = \left\{ \frac{\int_{V_1} \rho(\vec{r}) . r^2 . dv}{\int_{V_1} \rho(\vec{r}) dv} \right\}^{1/2} \qquad (49)$$

The radius of gyration of a homogeneous and spherical object is related to its radius R by $R_g = \sqrt{3/5} R$. In the case of a cylinder with radius R and height H, the radius of gyration is given by $R_g = \sqrt{(D^2/8) + (H^2/12)}$.

We will now focus the features of the small-angle X-ray scattering produced by a two-electron density system composed of a set of N spatially uncorrelated and anisotropic objects, all of them with a common orientation. For this system the scattering is obviously anisotropic so as the intensity function depends on the direction of the vector $\vec{q}$. In the limit of small $\vec{q}$, Guinier law becomes [8]

$$I_1(q_D) = N(\rho_1 - \rho_0)^2 V_1^2 e^{-R_D^2 . q_D^2} \qquad (50)$$

where q_D refers to the direction along which the scattering intensity is measured and R_D is the average inertia distance from a plane containing the center of "mass" of the electron density function, along the q_D direction. R_D is so defined as

$$R_D = \frac{1}{V_1} \int_{V_1} r_D^2 . dv = \overline{r_D^2} \qquad (51)$$

The features of the small-angle scattering intensity function corresponding to a dilute set of highly anisotropic objects with the same orientation are schematically illustrated in Fig. 6.

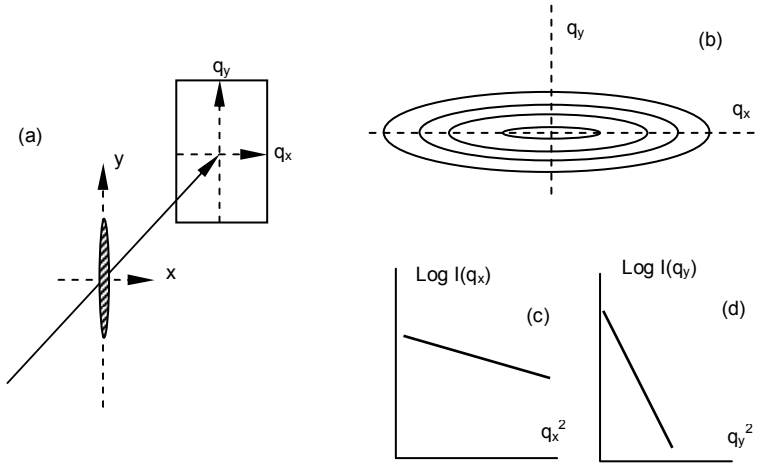

Fig. 6: (a) Schematic setup for a 2D recording of the scattering intensity. The nano-object is a long ellipsoid with its major axis along the y direction. (b) Iso-intensity lines indicating a anisotropic scattering intensity growing toward the origin. (c) and (d) Schematic Guinier plots along the directions x and y, respectively.

Fig 6a displays the geometry of the setup for the determination of the scattering intensity in two dimensions using a 2D gas detector or an image plate. A long nano-object (Fig. 6a) yields a anisotropic scattering pattern whose main features are shown in Fig 6b. The inertia distances along two perpendicular directions, parallel to axes q_x and q_y (Fig. 6b), can be determined using Guinier plots (Fig 6c and 6d, respectively). A rotation of the object of 90 degrees around the y axis allows for the derivation of the inertia distance along the third perpendicular direction.

4.3.2. Dilute and isotropic system composed of very anisotropic nano-objects

For a dilute set of very elongated cylinders with a nanometric radius R and for large and very thin platelets with a thickness T, Eq. (48) only applies within a small range, at very low q, that is not in practice attained in typical SAXS experiments. For very long and thin cylinders the function that exhibits a Gaussian q-dependence within the accessible small q-range is qI(q) [1,7,8]:

$$qI(q) \propto e^{-\frac{1}{2}R_c^2 q^2} \qquad (52)$$

where R_c is the radius of gyration of the circular section, $R_c = R/\sqrt{2}$. On the other hand, for very thin platelets with a nanometric thickness T and large lateral dimensions, the function that obeys a Guinier-type q dependence at small q is:

$$q^2 I(q) \propto e^{-R_t^2 q^2} \qquad (53)$$

with $R_t = T/\sqrt{12}$.

4.3.3. Dilute and isotropic system of polydispersed nano-objects

A dilute and isotropic system composed of nano-objects with a distribution of radii of gyration defined by $N(R_g)$ yields a total scattering intensity I(q), at small q, given by the sum of the individual contributions of each of them (Eq. 48):

$$I(q) = (\rho_1 - \rho_0)^2 \int N(R_g) V_1^2(R_g).e^{-\frac{R_g^2 q^2}{3}} dR_g \qquad (54)$$

Substituting the Gaussian function $\exp\left(-R_g^2 q^2/3\right)$, that is valid for small q by the parabolic function $1-\left(R_g^2 q^2/3\right)$, Eq. (54) can be rewritten as

$$I(q) = N(\rho_1 - \rho_0)^2 \left[\frac{1}{N} \int N(R_g) V_1^2(R_g).dR_g - \frac{q^2}{3} \frac{1}{N} \int N(R_g) V_1^2(R_g).R_g^2 dR_g \right] \qquad (55)$$

or again

$$I(q) = N(\rho_1 - \rho_2)^2 . \{V_1^2\} . e^{-\frac{\{R_g\}_G^2 q^2}{3}} \qquad (56)$$

where $\{V_1^2\}$ is the average value of V_1^2 given by

$$\{V_1^2\} = \frac{1}{N} \int N(R_g) V_1^2(R_g) dR_g \qquad (57)$$

and $\{R_g\}_G$ is a weighted average value of R_g (named Guinier average) defined by

$$\{R_g\}_G = \left[\frac{\int N(R_g).V_1^2 R_g^2 dR_g}{\int N(R_g).V_1^2 dR_g} \right]^{1/2} \qquad (58)$$

$\{R_g\}_G$ is an average that weight much more the large objects than small ones. For the simple case of a polydisperse set of spherical nano-objects, Eq. 58 becomes

$$\{R\}_G = \left[\frac{\int N(R).R^8 dR}{\int N(R).R^6 dR} \right]^{1/2} = \left[\frac{\{R^8\}}{\{R^6\}} \right]^{1/2} \qquad (59)$$

Guinier law (Eq. 56) is in practice applied to dilute sets of polydisperse nano-objects only when the size distribution has a moderate width. For very polydisperse systems, the q-range over which Guinier law holds is very small. On the other hand, Guinier plots yield in this case an average radius of gyration far from the arithmetic average and strongly biased towards those of the biggest objects. This effect is schematically illustrated for spherical objects in Fig. 7. Radius distributions with the same average but with different widths (Fig. 7a) lead to different Guinier average radius. On the other hand, the extrapolated intensity I(0) for a polydisperse system, being proportional to the average $\{V_1^2\}$, also depends on the detailed shape of the size distribution function. Both effects are schematically illustrated in Fig. 7b.

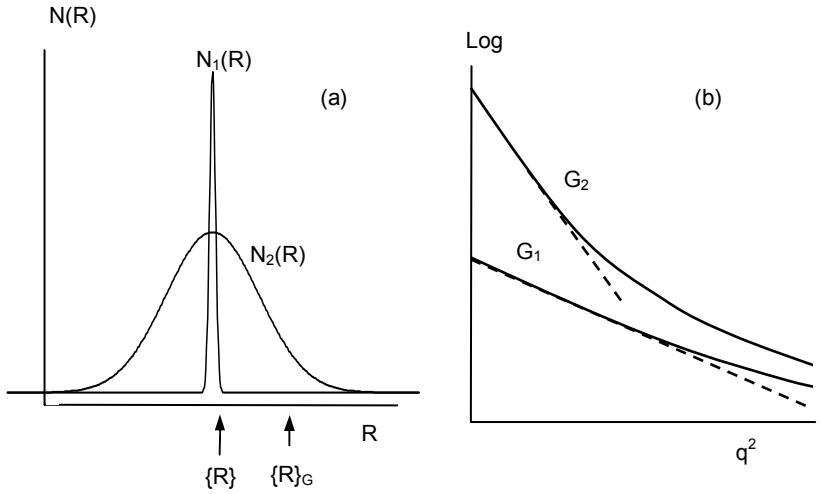

Fig. 7: (a) Narrow, $N_1(R)$, and wide, $N_2(R)$, radius distribution functions for spheres, both with the same radius average {R}. The $\{R\}_G$ arrow indicates the Guinier radius average corresponding to the wide distribution $N_2(R)$. (b) Schematic Guinier plots corresponding to the radius distributions $N_1(R)$ and $N_2(R)$. The magnitude of the slope of the linear part, at small q, and the extrapolated intensity I(0) for $N_2(R)$ are larger than for $N_1(R)$.

5. Small-angle scattering by a dilute system of nano-objects of simple geometry

The scattering intensity produced by two types of nanostructured materials consisting of a dilute set of colloidal particles embedded in a homogeneous matrix will be discussed in this section. These systems are (i) nano-objects of constant electron density ρ_1 embedded in a matrix with a constant density ρ_0 and (ii) nano-objects with a centro-symmetrical electron density, defined by its density function $\rho(r)$, also embedded in a homogeneous matrix of electron density ρ_0.

5.1. Homogeneous spherical nano-objects embedded in a homogeneous matrix

The total scattering intensity produced by a dilute set of N identical homogeneous objects with electron density ρ_1 embedded in a homogeneous matrix with density ρ_0 is N times the scattering intensity produced by each nano-object (Eq. 40). In the particular simple case of a isolated spherical nano-object with radius R, the characteristic function γ_0 is given by [1, 8] :

$$\gamma_0(r) = 1 - \frac{3r}{4R} + \frac{1}{16}\left(\frac{r}{R}\right)^3 \qquad (60)$$

and thus the scattering intensity per nano-object, $I_1(q)$ (Eq. 40), becomes

$$I_1(q) = (\rho_1 - \rho_0)^2 V_1 \int_0^{D_{\max}} \left[1 - \frac{3r}{4R} + \frac{1}{16}\left(\frac{r}{R}\right)^3\right] 4\pi . r^2 \, \frac{sin.qr}{qr} \, dr \qquad (61)$$

with D_{max}=2R. Solving the integral of Eq. (61), $I_1(q)$ becomes

$$I_1(q) = (\rho_1 - \rho_0)^2 . \left(\frac{4\pi R^3}{3} \right)^2 [\Phi(qR)]^2 \tag{62}$$

where

$$\Phi(qR) = 3 \frac{sin.qR - qR\cos qR}{(qR)^3} \tag{63}$$

Instead of starting from the characteristic function $\gamma_0(r)$, as described above, the scattering intensity produced by a single sphere can be alternatively derived from the amplitude $A_1(q)$ as follows

$$I_1(q) = |A_1(q)|^2 = \left| (\rho_1 - \rho_0) \int_0^R 4\pi . r^2 \frac{sin.qr}{qr} dr \right|^2 \tag{64}$$

Since the integral in Eq. (64) is equal to $(4\pi/3)R^3\Phi(q)$, the same result as Eq. (62) follows.

Intensity functions predicted by Eq. (62) or 64 are plotted in Fig. 8 for two sphere radii, namely R_1=22 Å and R_2=28 Å. As expected, the intensity I(0) (being proportional to R^6) is higher for the larger sphere. At small q the intensity functions satisfies Guinier law (inset in Fig. 8), the radius of the spheres being related to their radius of gyration by $R = (5/3)^{1/2} R_g$. At high q the intensity functions exhibit several maxima and zeros, the zeros being located at qR=4.52, 7.54, 10.87,... These oscillations were actually observed in a number of experimental SAXS studies of monodisperse or nearly monodisperse systems such as, for example, for nano-composites consisting of spherical PbTe nano-crystals embedded in a homogeneous matrix [9] that will be described in section 5.5.1.

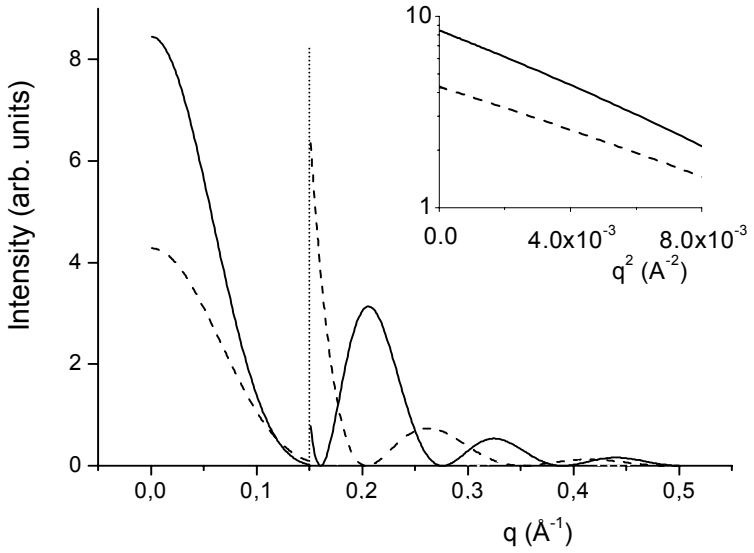

Fig. 8: Scattering intensity curves corresponding to identical spherical objects with radius R=22 Å (---) and 28 Å (—). Both curves are multiplied x 50 for q>0.15 Å^{-1} in order to clearly display the secondary maxima. Inset: Guinier plots of both curves.

5.2. Isotropic system of polydisperse nano-objects with simple shapes

The scattering intensity function related to a dilute set of N spherical nano-objects with a radius distribution defined by N(R) – schematically illustrated for two particular cases in Fig. 9 a and b - is calculated by solving the following equation

$$I(q) = \int N(R).I_1(q,R)dR \qquad (65)$$

where N(R)dR is the number of spheres with a radius between R and R+dR ($\int N(R)dR = N$), and I_1(q,R) is the scattering intensity produced by an isolated sphere (Eq. 62). Thus the total scattering intensity is

$$I(q) = (\rho_1 - \rho_0)^2 \left(\frac{4\pi}{3}\right)^2 \int N(R).R^6 \left[3\frac{sinqR - qR\cos qR}{(qR)^3}\right]^2 dR \qquad (66)$$

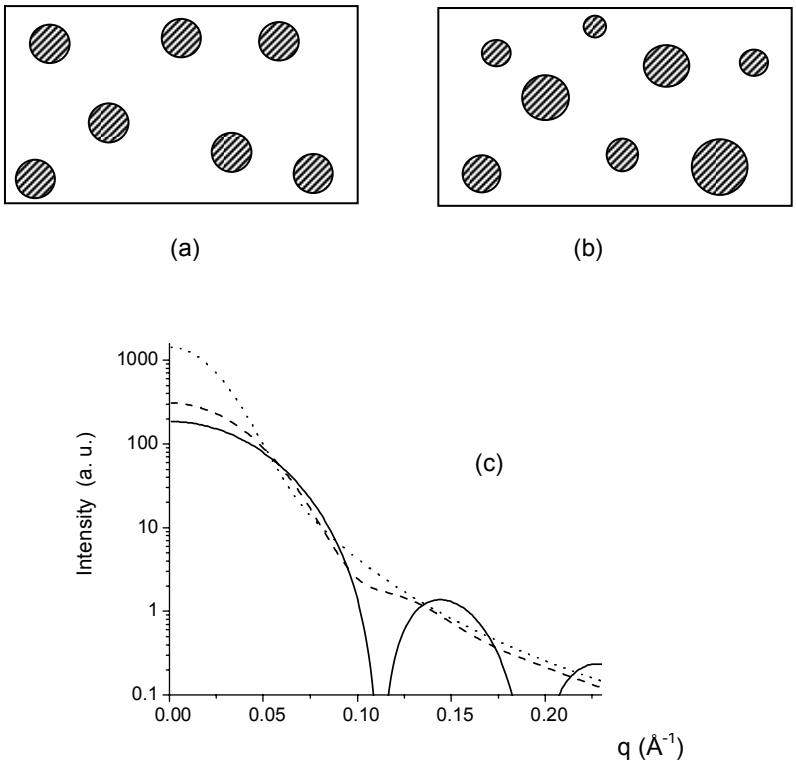

Fig. 9: Schematic views of a system composed of a dilute set of (a) monodisperse and (b) polydisperse spherical nano-objects. (c) Scattering intensities corresponding to three samples containing spherical objects with the same average radius {R}=40 Å and a Gaussian distribution with three different standard deviations: σ = 0 (——), σ = 10 (-----) and σ= 25 Å (⋯⋯).

In Fig. 9c the scattering intensity curves related to three sets of spherical objects with Gaussian radius distributions, with the same average radius {R}=40 Å, are plotted. The standard deviations of the three Gaussians are σ=0 Å, 10 Å and 25 Å, respectively. For the polydisperse sets of spheres (σ=10 and 25Å) the secondary maxima and zeros, exhibited by the set of identical spheres (σ=0), smear out. On the other hand, the intensity I(0), being proportional to {R^6} (Eq. 56) is, as expected, higher for larger σ values.

The issue generally addressed by materials scientists is the derivation of the radius distribution N(R) from the measured I(q) functions. A package named GNOM, developed by D. Svergun and collaborators [10], numerically solves the integral equation connecting I(q) and N(R) (Eq. 66). The output of GNOM program yields the volume distribution function, D(R), related to N(R) for spheres by

$$D(R) = \frac{4\pi}{3} R^3 .N(R) \qquad (67)$$

The GNOM package can be applied to determine the volume distribution function of other types of nano-objects with simple shapes. The intensity function $I_1(q)$ related to objects of complex shapes can be independently determined and used as an input file. In all these cases, provided the system is dilute and all nano-objects have the same shape, the output yields the volume distribution function. Other programs that also solve Eq. (66) were developed.

5.3. Heterogenous isotropic nano-objects

The small angle X-ray scattering by a centro-symmetrical nano-object, embedded in a matrix with a constant density ρ_0, will now be focused. Since the electron density of this object only depends on the modulus of the position vector, the SAXS intensity can be written, analogously to Eq. (64), as

$$I_1(q) = \left| \int_0^R 4\pi r^2 \left[\rho(r) - \rho_0\right] \frac{sinq.r}{q.r} dr \right|^2 \qquad (68)$$

where R is the radius corresponding to the external boundary of the nano-object

For an electron density ρ(r) modeled by a multi-step function, Eq. (68) has a simple solution. In the case of n steps defining different shells with densities ρ_i, it becomes

$$I_1(q) = \left[\sum_{i=1}^{n} \left(\rho_i - \rho_{i+1}\right) \int_0^{R_i} 4\pi r^2 \frac{sin.qr}{qr} dr \right]^2 \qquad (69)$$

with $\rho_{n+1}=\rho_0$, ρ_0 being the electron density of the matrix, or of the solvent in case of colloidal particles immersed in a liquid. The integral in Eq. (69) is equal to the function Φ(q) given by Eq (63) so as

$$I_1(q) = \left[\sum_{i=1}^{n} \left(\rho_i - \rho_{i+1}\right) (4/3)\pi R_i^3 3 \frac{sin.qR_i - qR_i \cos.qR_i}{\left(qR_i\right)^3} \right]^2 \qquad (70)$$

Eq. (70) has been applied to an investigation aiming at modeling the scattering intensity produced by a dilute set of spherical PbTe nano-crystals embedded in a silicate glass during the early stages of nucleation and growth. For this simple two-step model (Fig 10a) the intensity $I_1(q)$ is given by

$$I_1(q) = \left[A_1(q) + A_2(q)\right]^2 = \left[\left(\rho_1 - \rho_2\right) \frac{4}{3} \pi R_1^3 3 \frac{\sin .qR_1 - qR_1 \cos .qR_1}{\left(qR_1\right)^3} + \left(\rho_2 - \rho_0\right) \frac{4}{3} \pi R_2^3 3 \frac{\sin .qR_2 - qR_2 \cos .qR_2}{\left(qR_2\right)^3} \right]^2 \qquad (71)$$

The scattering intensity function $I_1(q)$ and the two partial amplitudes between brackets, $A_1(q)$ and $A_2(q)$, are plotted in Fig. 10b. Since $\rho_1 > \rho_2$ and $\rho_2 < \rho_0$, $A_1(q)$ and $A_2(q)$ are in opposite phase.

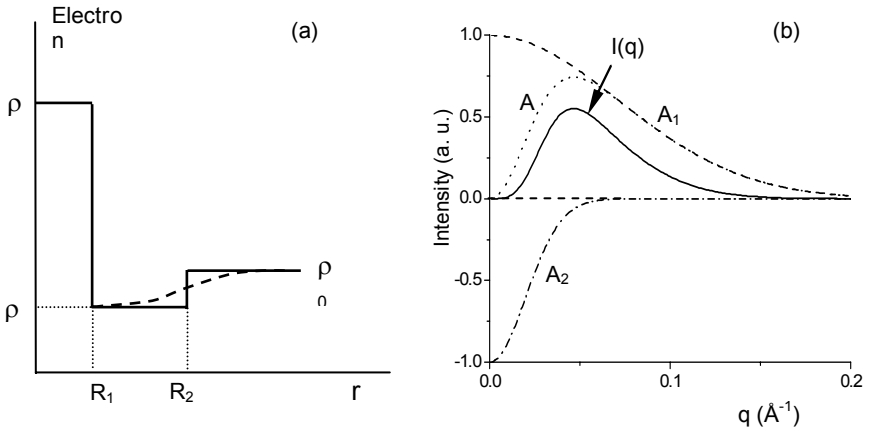

Fig. 10: (a) The solid line represents the electron density as a function of the radius for a simple isotropic two-step model of a spherical nano-object surrounded by a depleted shell. The dashed line corresponds to a more realistic model for the density profile inside the depleted shell around the spherical object. (b) Schematic scattering intensity under Guinier approximation, I(q), produced by the two-step model defined in Fig 10a. Scattering amplitudes associated with the nano-object (A_1) and with the depleted shell (A_2). The curve A is the sum of both amplitudes.

The different parameters in Eq. 70 or 71 are determined by non-linear fitting procedures. In the case in which the shell with an electron density ρ_2 corresponds to the depleted zone produced by up-hill migration of atoms from the matrix toward segregated spherical clusters, the following relations are obeyed:

$$\frac{4}{3}\pi R_1^3(\rho_1-\rho_0)=\frac{4}{3}\pi\left(R_2^3-R_1^3\right)(\rho_0-\rho_2) \qquad \text{and} \qquad R_1^3(\rho_1-\rho_2)=R_2^3(\rho_0-\rho_2) \qquad (72)$$

Eqs. (72) implies that all atoms inside the central cluster came from the surrounding depleted shell so that the initial state corresponds to a homogeneous material. This approach was applied in order to characterize Guinier-Preston zones in Al-Ag alloys [11].

Simple smooth functions were also used to model the electron density of depleted shells around growing spherical nano-crystals embedded in a supersaturated solid solution. For a Gaussian profile characterized by a radius of gyration R_g much larger than R, the scattering intensity can be written as [12]

$$I_1(q)=(\rho_1-\rho_2)^2\left(\frac{4}{3}\pi R^3\right)^2\left[\Phi(qR)-e^{-R_g^2q^2/6}\right]^2 \qquad (73)$$

where $\Phi(qR)$ is given by Eq. (63).

The model of spherically symmetric nano-objects, with a r-dependent electron density, was also successfully applied to studies of isotropic colloidal micelles composed of macromolecules, with hydrophilic head and hydrophobic tail, embedded in water.

The functions $I_1(q)$ presented above also describe the q dependence of the scattering intensity produced by a dilute set of N identical nano-objects. As it will be described in section 6, and similarly to the function plotted in Fig. 10c, scattering curves with a maximum at $q\neq 0$ are also observed for concentrated systems of simple colloidal particles, the peak in this case being a consequence of

interference effects produced by inter-particle spatial correlation or close packing. Therefore a peak eventually observed in an experimental scattering curve can safely be exclusively assigned to intra-particle interference effects, as described in this section, only if the system is dilute.

5.4. Polydispersed nano-objects with irregular shapes

Dilute sets of nano-objects with different shapes and some polydispersivity yield a scattering intensity function with known asymptotic behaviours at small and high q. At small q, Guinier law applies and, at high q, Porod law holds for a variety of object geometries. A semi-empirical equation for the whole scattering intensity function that obeys both - Guinier and Porod - asymptotic trends was proposed by Beaucage [13]:

$$I(q) = G.e^{-\frac{1}{3}R_g^2 q^2} + B.\left(\frac{1}{q^*}\right)^P \qquad (74)$$

where $q^* = \dfrac{q}{[erf\left(kqR_g / 6^{1/2}\right)^3]}$

The error function is a cut-off of the Porod regime for the low q range. The parameters G, B, k and P depend on the electron density contrast, size and shape of the objects. For simple two-electron density systems composed of globular nano-objects (nor flat disk neither thin cylinders) these parameters are: $G = N(\rho_1 - \rho_0)^2 V_1^2$, $B = 2\pi N(\rho_1 - \rho_0)^2 S_1$, P=4 and k=1. Thus Eq. (74) becomes

$$I(q) = N(\rho_1 - \rho_0)^2 V_1^2 .e^{-\frac{1}{3}R_g^2 q^2} + 2\pi N(\rho_1 - \rho_0)^2 S_1.\left(\frac{1}{q^*}\right)^4 \qquad (75)$$

The semi-empirical Eq. (74) can also be applied to dilute sets of other more complex objects such as fractals, polymers and low dimensional objects (such as flat disks and narrow cylinders). For these systems, Eq. (74) also holds, but in these cases the set of parameters G, B, P and k are defined from the particular features of the proposed models or experimentally determined by adequate fitting procedures [13].

5.5 Examples of structure characterization of dilute systems of isolated objects embedded in a homogeneous matrix.

5.5.1 Spherical nano-objects with approximately same size. Growth of PbTe nano-crystals embedded in a silicate glass

Many investigations demonstrated that SAXS is a useful technique for the study of the process of formation of nano-crystals or liquid nano-droplets in a homogeneous matrix. For systems containing spherical nano-objects with a high contrast in electron density (e. g. metal nano-crystals in glass), the experimental results generally provide a precise characterization.

A SAXS study of a particular system composed of PbTe nanocrystals embedded in a silicate glass [9] will be now described. This nano-material exhibits interesting non-linear optical properties in the infrared making it potentially useful for applications to telecommunication devices. An initially homogeneous silicate glass, doped at high temperature with Pb and Te, was quenched and then submitted to an isothermal annealing at 650C. The initially isolated Pb and Te species diffuse through the supersaturated glass and nucleate PbTe nanocrystals which progressively grow. In the meantime a set of SAXS intensity curves were successively recorded.

The experimental results, displayed in Fig.11, indicate that the SAXS intensity progressively increases for increasing annealing time. At high q, the curves exhibit an oscillation and a secondary maximum that are characteristic of a set of spheres of nearly identical size. This maximum

progressively shifts towards smaller q as expected for growing nano-spheres. The position and intensity of the observed secondary maximum are consistent with the theoretical prediction (Eq. 62). We can notice that the secondary maximum is not clearly apparent in the early stages of crystal growth because of the high statistical dispersion in scattering intensities at high q. The positive deviation of the experimental points from the theoretical model at very small q indicates the existence of rather large heterogeneities of the electron density in the glass matrix.

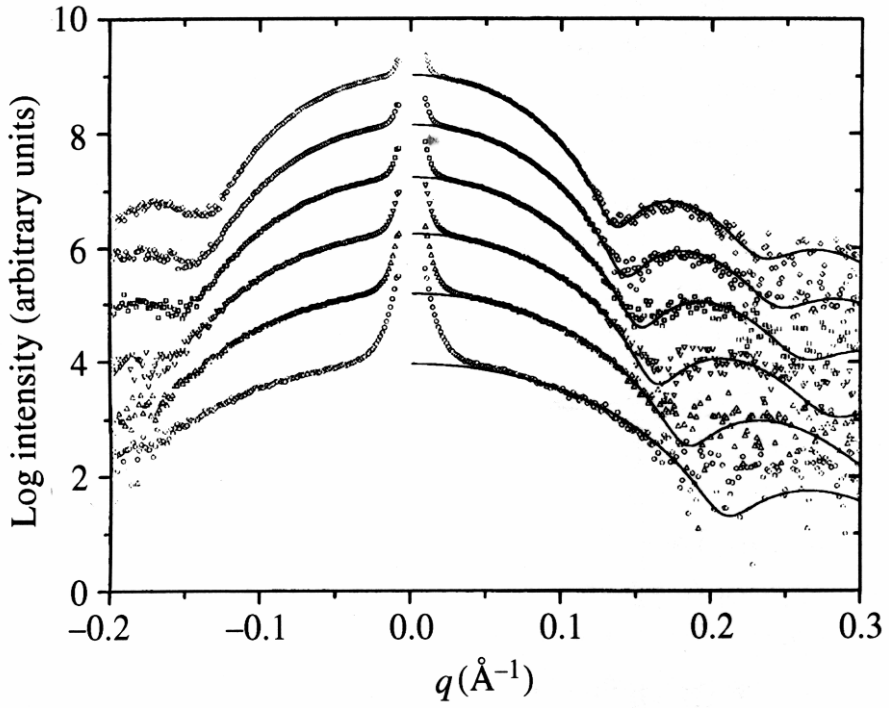

Fig 11: PbTe nano-crystals embedded in a homogeneous silicate glass. Scattering intensity curves corresponding to a dilute set of spherical PbTe nano-crystals during isothermal growth (T=650C) [9]. The continuous line is the best fit of Eq. (66) using a Gaussian N(R) function with a time varying radius average and a constant relative standard deviation [σ /{R}] =0.08. The curves were vertically displaced for clarity

The curves displayed in Fig 11 were fitted using Eq. 66, which applies to a dilute set of spherical objects, assuming a time-varying average nano-crystal radius and a Gaussian radius distribution, N(R), with a time-independent relative standard deviation σ/{R}= 0.08. For an annealing time of 2 hours the best fit lead to {R}=32.5 Å and σ=2.6 Å. Finally, it was demonstrated that the time dependence of the average radius {R} agrees with the prediction of the classical theory of nucleation and growth of spherical precipitates in a homogeneous matrix.

5.5.2 Spheroidal nano-objects with a time-varying size distribution. First stages of the aggregation of colloidal ZnO clusters in a liquid suspension

Powders composed of ZnO nano-particles obtained by the sol-gel route are used as precursors for the development of materials with interesting properties. The first step of sol-gel processing leading to ZnO nano-particles is the formation of a liquid suspension of zinc acetate in ethanol in which LiOH is added under ultrasound treatment. Maintaining the solution inside a close cell at a constant temperature, the dissolved molecules start to aggregate, yielding colloidal particles of progressively increasing size. Tokumoto et al [14] performed an in situ SAXS study in order to study the first steps of the aggregation process. The different experimental scattering functions obtained after increasing periods of time were analyzed assuming that the system is dilute and that the colloidal particles are

nearly spherical. In order to determine the radius distribution of the colloidal particles, the integral Eq. 66 was solved by using the GNOM package [10].

The mentioned numerical procedure was applied to all the recorded experimental scattering curves of the studied ZnO based suspension, corresponding to different periods of aggregation time, thus yielding the set of particle volume distribution functions D(R) (Eq. 67) plotted in Fig. 12. The shape of D(R) and its time variation demonstrated that the kinetics formation of the ZnO colloidal particles is characterized by two main stages. During the first one, a growing peak centered at R= 17 Å is apparent,indicating a continuous formation of small particles. The number of these olygomers increases monotonously for increasing reaction time, while their average size, {R}=17 Å, remains constant. In a second stage, the volume distribution function exhibits a still growing peak at 17 Å and the appearance and growth of a second one corresponding to an initial average particle radius {R}= 60 Å. The position of this peak shifts continuously toward higher R values up to 110 Å for a period of time of 2 hours. The described time variation of the volume distribution function clearly indicates the continuous formation of colloidal primary particles and their simultaneous aggregation and consequent growth.

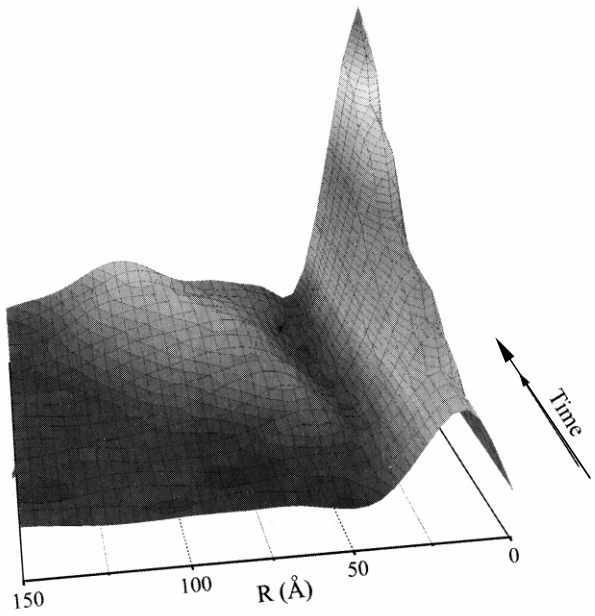

Fig 12: ZnO based colloidal suspensions. Time-dependent volume distribution functions D(R) of ZnO colloidal particles maintained inside a sealed cell during SAXS measurements [14]. The time increases from 10 up to 120 min. The volume functions were derived, using the GNOM package [10], from the set of experimental SAXS curves.

6. Small-angle scattering of a concentrated set of nano-objects

Many nano-materials consist of a concentrated set of isolated nano-phases embedded in a homogeneous matrix, e.g. colloidal sols (solid nano-clusters embedded in a liquid matrix) and nano-hybrid materials (solid inorganic clusters embedded in a solid polymeric matrix). Often these systems cannot be considered as dilute in the sense that the scattering intensity is not simply given by $I(q)=N.I_1(q)$ (Eq. 37) over the whole q range. It will be described in this section how to analyze SAXS results corresponding to materials whose structure can be described by simple models, namely (i) concentrated systems composed of isolated nano-objects with spherical shape and (ii) fractal structures built up by the aggregation of primary nano-objects in solid or liquid solutions.

6.1 The hard sphere model

For a concentrated system of N of nano-objects Eq. (37), $I(q) = N < I_1(\vec{q}) >$, does no longer hold over the whole q range. In the case of simple isotropic systems consisting of centro-symmetrical and spatially correlated objects, it is possible decoupling the function defining the q dependence of the total scattered intensity I(q) in two terms: the intensity produced by an isolated object, $I_1(q)$ (often named as form factor) and the structure function, S(q), which accounts for interference effects between the elementary scattered wavelets. Thus the scattering intensity expected from this model can be written as

$$I(q) = N.I_1(q).S(q) \tag{76}$$

Eq. (76) is rigorously obeyed only when the scattering system is composed of identical spheres (or more generally of centro-symmetrical objects) and can be used as a more or less good approximation for not too anisometric structure units. Obviously, for dilute systems, S(q)=1 holds over the whole q range.

The structure function corresponding to a isotropic set of spherical objects, like those schematically shown in Fig. 13a and 13b, is given by [8]

$$S(q) = 1 + \frac{1}{V_p}\int_0^\infty [g(r) - 1] 4\pi r^2 \frac{\sin qr}{qr} dr \tag{77}$$

where V_p=V/N is the volume available per object and g(r) is a function defined in such a way that $4\pi r^2 dr.g(r)/V_p$ yields the average number of nano-objects, N(r), at a distance between r and r+dr from an object located at the origin. From this definition, we notice that g(r) equal to 1 corresponds to a random spatial distribution. For a set of completely disordered objects (an "ideal gas") g(r)=1 for all r. For any type of system with short-range correlation, g(r) tends to 1 in the high r limit.

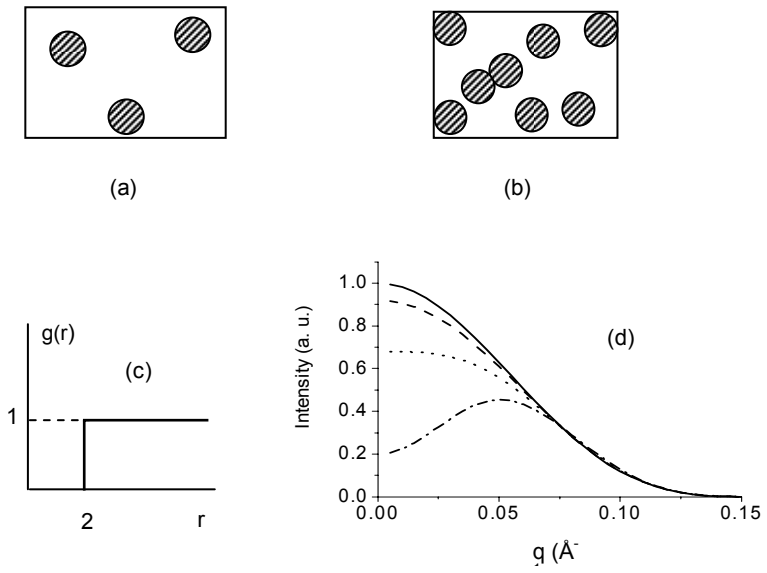

Fig. 13: Schematic dilute (a) and concentrated (b) systems of hard spheres. (c) g(r) function for the hard sphere model. (d) Scattering intensity determined using Eq. (76) with S(q) defined by Eq.(78), for different quotients v_1/v_p starting from 0 (top) up to 0.05 (bottom).

In the simple case of a ideal solution of spherical nano-objects, in which the only correlation is a hard sphere interaction due to impenetrability, g(r) is a step function as shown in Fig. 13c. Substituting this function in Eq. (77) the structure function S(q) results [8]

$$S(q) = 1 - 8\left(\frac{V_1}{V_p}\right)\Phi(q,R) \tag{78}$$

where V_1 is the volume of the sphere, $V_1 = (4\pi/3)R^3$, and Φ(q,R) is a function similar to that already used to define the scattering amplitude produced by spherical particles (Eq. 63):

$$\Phi(q,R) = 3\frac{\sin(2qR) - 2qR\cos(2qR)}{(2qR)^3} \tag{79}$$

The scattering intensity given by Eq. (76) with the structure function S(q) and the function Φ(q,R) defined by Eq. (78) and (79), respectively, are displayed in Fig. 13d for several ratios V_1/V_p. This equation leads to physically acceptable results only for low concentrations. For example, for V_1/V_p>0.12, the intensity becomes negative at very small q. This happens because the step function g(R) displayed in Fig. 13c does not apply for high values of the concentration factor (V_1/V_p). These results indicate that the direct application of Guinier law (Eq. 48) to concentrated systems may lead to an apparent radius of gyration smaller than the real one. A general conclusion from this is that a linear behavior eventually observed in Guinier plots does not guarantee that Guinier law can safely be applied. In order to determine the average radius of gyration of concentrated nano-objets an equation including the structure function should be fitted to the whole scattering intensity curves.

6.2 Spherical nano-objects embedded in a solid matrix

A class of hybrid materials prepared by the sol-gel procedure are composed of inorganic nano-clusters embedded in a polymeric matrix. The nanoheterogenous structure of these materials can be characterized using a simple two-electron density model consisting of high electron density clusters embedded in a homogeneous matrix [15]. Certainly, the polymeric phase exhibits electron density fluctuations at molecular level that produces small-angle scattering but its contribution to the total scattering intensity is assumed to be weak and/or not strongly varying with q. The basic assumption is that the dominant contribution to small angle scattering intensity comes from the electron density contrast between the rather heavy inorganic nano-clusters and the light polymeric matrix.

A semi-empirical structure function that describes the spatial correlation of colloidal spherical objects, derived using the Born-Green approximation, is given by [8]

$$S(q) = \frac{1}{1 + k\Phi(q,d)} \tag{80}$$

where k, named as packing factor, refers to the degree of correlation of the structure and d is the average distance between the spatially correlated nano-objects. The maximum value of k is expected for the closest packing of spheres (k_{max}= 5.92). The function Φ(q,d) is a defined as

$$\Phi(q,d) = 3\frac{\sin(qd) - qd\cos(qd)}{(qd)^3} \tag{81}$$

Some examples of theoretical scattering functions, I(q), are displayed in Fig. 14a and 14b for different values of d and k. Increasing values of the packing factor k yield more pronounced and well-

defined peaks. The q value corresponding to the maximum of the scattering curves, q_{max}, decreases for increasing average distances d. This last property justifies the semi-quantitative simple equation

$$d = \frac{2\pi}{q_{\max}} \tag{82}$$

that is often applied in the literature in order to derive an estimate of the average distance between clusters.

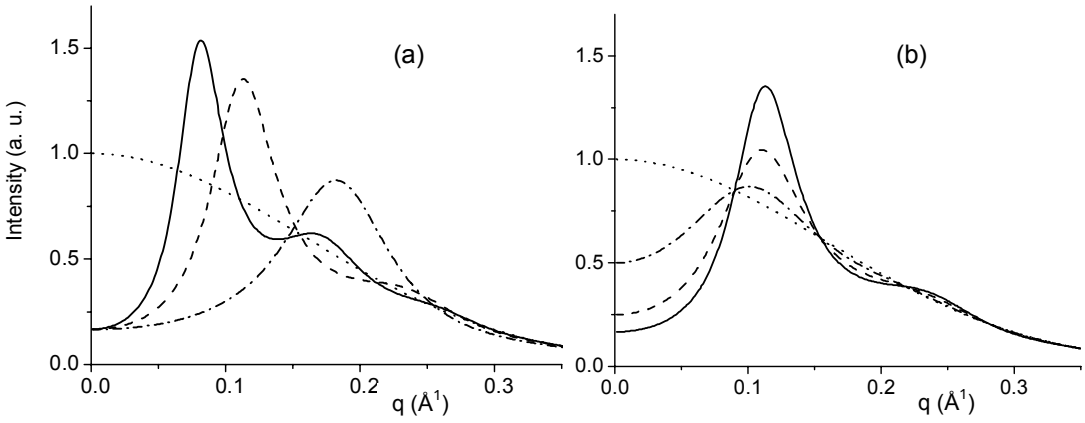

Fig. 14: Scattering intensity curves corresponding to different systems containing spatially correlated spheres. The spheres have all them the same radius, R=10 Å. (a) Packing factor k=5 and average distances d=30 Å(-.-.-.-), d=50 Å(-----) and d=70 Å (—). (b) Average distance d=50 Å and packing factor k=1 (-·-·), k=3 (------) and k=5 (—).

Even if the nano-objects are not spherical but they have a globular shape, the structure function given by Eq. (80) is in many cases assumed to be valid as a good approximation. The total scattering intensity, $I(q)=NI_1(q)S(q)$ (Eq. 76), is thus determined using the intensity $I_1(q)$ defined by Eq. (62) for spherical colloidal objects or by Eq. (75) (with N=1) for non-spherical (globular) nano-objects. This model also approximately applies to materials composed of moderately polydisperse nano-objects.

Eq. (82) is only a rough approximation for the determination of the average distance between nano-objects. As a matter of fact, the trend of the curves plotted in Fig. 14a and b, indicates that, instead of 2π in Eq. (82), a value 5.6 yields a more precise estimate of d for a wide range of typical R and k values. Thus we should remind that Eq. (82) only yields a rough estimate of the average inter-object distance and that a more precise evaluation can only be achieved by fitting realistic model functions to the whole experimental scattering curve.

6.3 Fractal structures

The fractal model has been applied to describe the structure of many materials generated by clustering processes in a liquid or solid medium. Many sols (gel precursors) that have been studied by small-angle scattering in situ exhibit this type of structure. Fractal objects can be characterized by three relevant structural parameters: (i) a radius r_0, which corresponds to the size of the individual primary particles (basic nano-objects that build up the fractal structure), (ii) a fractal dimension D that depends on the mechanism of clustering or aggregation, and (iii) a correlation length ξ that defines the whole aggregate size if the fractal objects are isolated or a cut-off distance of the fractal structure for percolated systems such as, for example, fractal gels.

For a homogenous object or for a fractal aggregate, such as those schematically illustrated in Fig. 15a and 15b, respectively, the total N of primary objects or building blocks located inside a sphere of radius r, measured from the center of mass, is given by

$$N(r) = \left(\frac{r}{r_0} \right)^D \tag{83}$$

This equation implies that the mass function M(r) is also proportional to r^D.

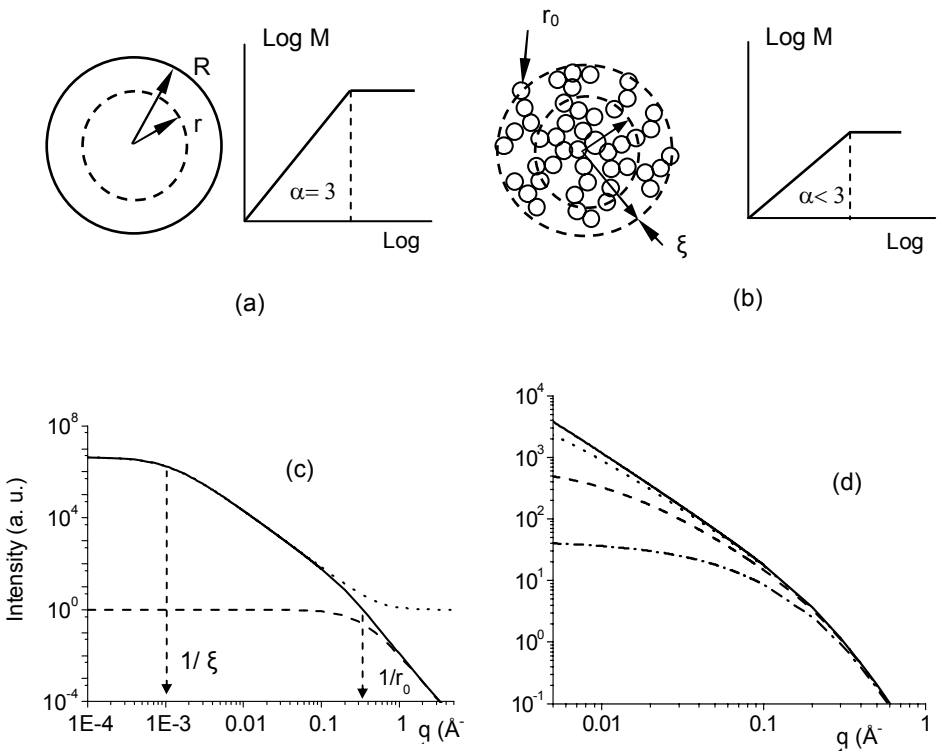

Fig. 15: (a) Schematic log-log plot of the mass M(r) of a homogeneous object. (b) The same for a fractal object. (c) Scattering intensity (Eq. 88) corresponding to a fractal object with r_0=3 Å, ξ=1000 Å and D=2 (——). Scattering intensity produced by a basic particle (form factor) defined by Eq. 87 (------) and structure function S(q) defined by Eq. 86 (…….). (d) Scattering intensity curves (Eq. 88) for r_0=3 Å, D=1.8 and ξ ranging from 20 Å (bottom) up to (2500 Å) (top).

The exponent in Eq. (83) for homogeneous objects is D=3, while D<3 for fractal structures. The particular values of D, the fractal dimension, depend on the particular mechanism of aggregation. Many mechanisms were theoretically analyzed and the respective fractal dimensions of the resulting structures were determined. This implies that the experimental evaluation of the dimension D may yield a useful insight about the predominant mechanism that governs the aggregation process.

In order to define the radial distribution function g(r) associated to a fractal structure, Sinha et al [16] included a cut-off function that makes the number density of primary objects at high r to be equal to the average number density. Later on, Chen and Teixeira [17] have used the general theory of liquids in order to define the function g(r) as follows

$$\frac{N}{V}g(r) = \frac{N}{V} + \left(\frac{D}{4\pi r_0^D} r^{D-3}\right) e^{-r/\xi} \tag{84}$$

Thus, substituting Eq. (84) in the general Eq. (77), the structure function S(q) becomes

$$S(q) = 1 + \frac{D}{r_0^D} \int_0^\infty r^{D-1} e^{-\frac{r}{\xi}} \frac{\sin qr}{qr} dr \tag{85}$$

and, solving Eq. (85), S(q) results [18]

$$S(q) = 1 + \frac{1}{(qr_0)^D} \frac{D.\Gamma(D-1)}{\left[1 + 1/(q^2\xi^2\right]^{(D-1)/2}} \sin\left[(D-1)\tan^{-1}(q\xi)\right] \tag{86}$$

Since the primary particles are much smaller than the fractal aggregates, $I_1(q)$ is a constant within a wide q range, so as the variation of the scattering intensity at small and intermediate q´s is dominated by the structure function. At high q, S(q) becomes a constant and so, over this q range, the variation in the scattering intensity is governed by $I_1(q)$. Several simple functions have been used for $I_1(q)$, such as the intensity produced by spherical particles (Eq. 62), the Beaucage function (Eq. 75) or the Debye-Bueche function given by

$$I(q) = \frac{A}{\left(1 + r_0^2 q^2\right)^2} \tag{87}$$

A being a constant.

Thus, selecting $I_1(q)$ defined by Eq. (87), the scattering intensity produced by a fractal aggregate becomes

$$I(q) = \frac{A}{\left(1 + r_0^2 q^2\right)^2} \cdot \left\{1 + \frac{1}{(qr_0)^D} \frac{D.\Gamma(D-1)}{\left[1 + 1/(q^2\xi^2)\right]^{(D-1)/2}} \sin\left[(D-1)\tan^{-1}(q\xi)\right]\right\} \tag{88}$$

Several scattering intensity functions defined by Eq (88) for different structural parameters are plotted in log-log scale in Fig. 15c and d. If the condition $\xi >> r_0$ is obeyed, the scattering intensity exhibits three distinct and simple q dependences over different q ranges (Fig. 15c). The main features of the scattering curves are directly and simply connected to the relevant structure parameters of the fractal nano-objects as described below.

(i)The scattering intensity extrapolated to q=0 is related to ξ and R_g by

$$I(0) \propto \xi^D \qquad \text{and} \qquad I(0) \propto {R_g}^D \qquad \text{with} \qquad R_g = \left[\frac{D(D+1)}{2}\right]^{1/2} \xi \tag{89}$$

(ii) Over the small q range ($q<1/\xi$) the scattering intensity exhibits a behavior similar to Guinier law (Eq. 48):

$$I(q) = I(0)\left\{1 - \left[\frac{D(D+1)}{6}\right]\xi^2 q^2\right\} \cong I(0).e^{-\frac{R_g^2 q^2}{3}} \qquad (90)$$

iii) In the intermediate q range, i. e. for $1/\xi << q << 1/r_0$, the scattering intensity exhibits a simple power q-dependence (a linear behavior in a log-log plot), the magnitude of the exponent being the fractal dimension:

$$I(q) \propto q^{-D} \qquad (91)$$

iv) At high q ($q>>1/r_o$) the scattering intensity asymptotically satisfies Porod's law (Eq. 34):

$$I(q) \propto \frac{1}{q^4} \qquad (92)$$

v) Two crossovers of the straight lines in the log I vs. log q plot, at $q=q_1$ and $q=q_2$ ($q_2>q_1$) are apparent. The radius of the primary particle r_o is simply related to q_2 by $r_o=1/q_2$ and the size parameter of the fractal aggregate or correlation length is given by $\xi=1/q_1$.

Thus, if $\xi >> r_o$, the relevant structure parameters ξ, D and r_o can be directly and easily determined from log-log plots of the scattering intensity. If the two crossovers are not well defined - as in the two first curves displayed in Fig. 15d - the fit of the I(q) function defined by Eq. 88 to the whole experimental data is the only way to determine ξ, D and r_o. However, one should be cautious about the physical meaning of a proposed "fractal" model when the condition $\xi >> r_o$ is not obeyed. It is a general consensus that, in order to safely establish the fractal nature of the aggregates, the quotient ξ/r_o should be larger than about 10.

On the other hand, as power q-dependences with an exponent leading to a D value smaller than 3 are also expected for non-fractal objects of low dimensionality (linear chains or thin platelets), it is useful to add independent arguments in order to give a stronger support to a proposed fractal model. If the aggregation process is studied by SAXS in situ - during the growth of the aggregates - many successive scattering intensity curves can be determined (Fig. 15d). In this case, an alternative method for evaluating the fractal dimension can be applied. Displaying the several scattering curves as Guinier plots (log I(q) versus q^2) and applying the relations given by Eq. (90), the correlation length of the aggregates, ξ, the radius of gyration, R_g, and the extrapolated intensity, I(0), can be determined for the different scattering curves. A log-log plot of I(0) versus ξ (or log I(0) versus log R_g) is expected to be linear (Eq. 89) and the fractal dimension D is thus determined as the slope of the straight line. Eventual variations of the exponent D along the growth process indicate changes in the characteristics of the mechanism of aggregation. An example of the use of this approach will be described in section 6.5.1 [19].

6.4. Hierarchical structures

Materials may contain heterogeneities at multiple structural levels. For example, nanometric clusters can be formed in a homogeneous phase and these nano-objets may segregate and form domains of tenth or hundredth nanometers (Fig. 16a). Often, for these complex systems, the scattering intensity curves in log-log scale exhibit a smooth step-like shape as schematically shown in Fig. 16b. The scattering intensity produced by this type of materials can, in many cases, be described by a semi-empirical equation proposed by Beaucage et al [20]:

$$I(q) = \left[G_1.e^{-\frac{1}{3}R_{g1}^2 q^2} + B_1.e^{-\frac{1}{3}R_c^2 q^2}\left\{erf\left(qR_{g1}/6^{1/2}\right)\right\}^3/q\right)^{P_1}\Bigg] + \left[G_2.e^{-\frac{1}{3}R_{g2}^2 q^2} + B_2.\left\{erf\left(qR_{g2}/6^{1/2}\right)\right\}^3/q\right)^{P_2}\Bigg] \qquad (93)$$

where the index 1 corresponds to the first - coarse - structure level and the index 2 to the fine substructure. Both main terms are analogous to Eq. (74), the first one having a high-q cut-off described by a Gaussian function $\exp(-R_c^2 q^2/3)$ with a cut-off radius R_c equal to the parameter R_{g2} (R_c=R_{g2}). A schematic overall shape of the I(q) function that may be expected for a two-level structure is displayed in the log-log plot shown in Fig. 16b.

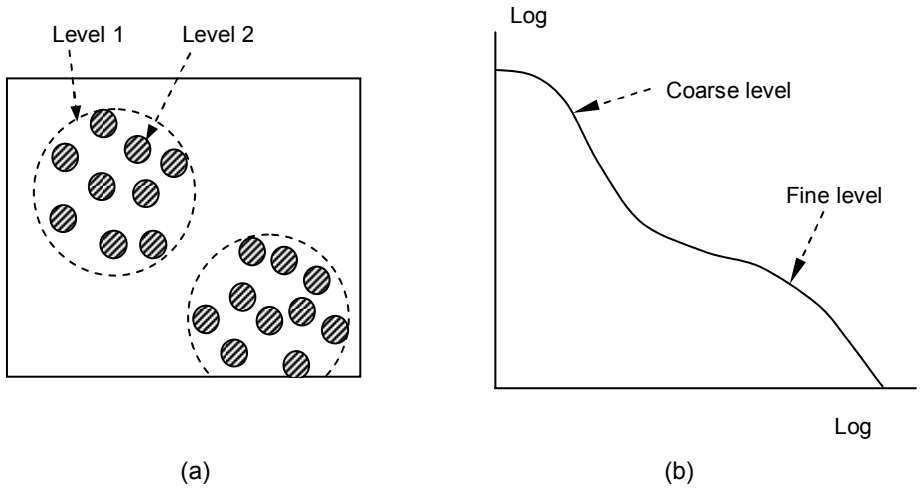

Fig. 16: (a) Two-level hierarchical structure. (b) Schematic scattering intensity showing the two q ranges from which the relevant information related to each structure level is derived

If the scattering experiment covers a very wide q range, more than two structural levels can be characterized. In addition, the scattering objects in each structural level may be spatially correlated. Eq. (93) can be generalized for multiple (n) structural levels also including correlation effects thus becoming

$$I(q) = \sum_{i=1}^{n} \left[\left(G_i . e^{-\frac{1}{3} R_{gi}^2 q^2} + B_i . e^{-\frac{1}{3} R_{g(i+1)}^2 q^2} \left\{ \left[erf\left(qR_{gi} / 6^{1/2} \right) \right]^3 / q \right\}^{P_i} \right) . S_i(q) \right] \qquad (94)$$

where the structure functions $S_i(q)$ may be one of those described in section 6.2 (Eq. 78 or 80).

Since the q range that are to be covered for the study of many-level structures is very wide, several experimental studies of the same sample using different setup collimation conditions and/or wavelengths are required. Typical studies include ultra-small angle X-ray scattering and light scattering measurements. Reference [20] reports several examples that illustrate satisfactory fits of Eq. 94 to experimental scattering curves corresponding to materials with many structural levels.

6.5 Examples of investigations of fractal aggregates and hierarchical structures.

6.5.1. Fractal structures. Aggregation process in zirconia-based sols and gels

Zirconia–based sols and gels were investigated by SAXS by many authors. Lecomte et al [21] studied this material in situ, during the aggregation process in the sol state. All scattering curves, plotted as log.I(q) vs. log.q in Fig. 17, exhibit a well-defined linear regime. The magnitude of the slope of the straight line (1.7) was assigned to the fractal dimension D of the growing aggregates (Eq. 91). The low-q limit of the linear portion of the scattering curves displayed in Fig. 17 progressively shifts toward lower q for increasing periods of time. This indicates that $\xi \propto 1/q_1$ - the magnitude of the aggregates size - grows continuously. The high-q limit of the linear range, near q_2, is not apparent in the main set of curves displayed in Fig. 17, but in the inset, corresponding to the final gel state and

measured up to a higher maximum q value, the high q cross over toward a Porod behavior ($I(q) \propto q^{-4}$) can be noticed. This suggests that the primary sub-units have a smooth and well-defined external surface.

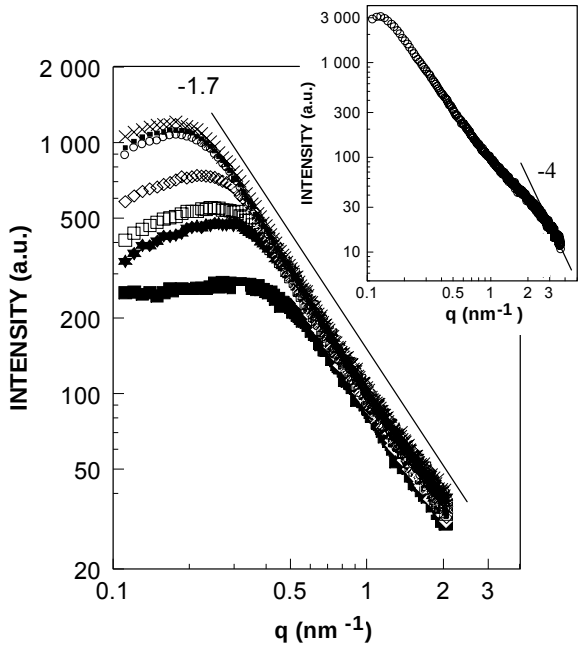

Fig. 17: Zirconia-based sols. Log I vs. log q plots for increasing periods of time from 4 hours (bottom) up to 742 hours (top) [21]. The inset is the scattering intensity curve of the final gel obtained after a period of about twice the gelling time.

The described results indicate that the fractal clusters in the studied zirconia-based sol result from the aggregation of very small colloidal particles formed at the beginning of the hydrolysis and condensation reactions. On the other hand, the maximum observed in the scattering curves is related to the existence of spatial correlation between the fractal aggregates, which could be analytically described by an inter-aggregate structure function S'(q) (Eq. 78 or 80) included as an additional factor in Eq. 88. A fractal dimension close to 1.7, as that experimentally determined, was theoretically derived by computer simulation for the mechanism of growth named diffusion limited cluster aggregation. Since the fractal dimension is time independent, it was concluded that the mechanism of aggregation is the same during the whole growth process.

A SAXS study of sulfate-zirconia sols with many compositions (different HNO_3, H_2O and H_2SO_4 contents) was performed by Riello et al [19]. In order to characterize the aggregation mechanisms, these authors determined the scattering curves, maintaining the sols in an open cell, after progressively increasing time periods. Firstly, applying Guinier, I(0) and R_g were determined for each scattering curve and then these values were plotted as log I(0) vs. log R_g. This plot is expected to be linear (Eq. 89). The experimental results indicated two successive different linear regimes: for Rg<20 Å the slope is D≈1 while, for Rg>20 Å, D ranges from 1.73 to 1.93 depending on the chemical composition of the sol.

The same authors also studied several sulfate-zirconia sols with different compositions in sealed cells [19]. Since in sealed condition the reactions in the sols are very fast, only the scattering curves corresponding to the final states were determined (Fig. 18a). The log I(0) vs. log R_g plot corresponding to the final states of all the studied samples is displayed in Fig. 18b. It can be noticed that the

experimental points also lie on two straight lines with similar slopes as those observed for the in situ studies during the growth in open cells.

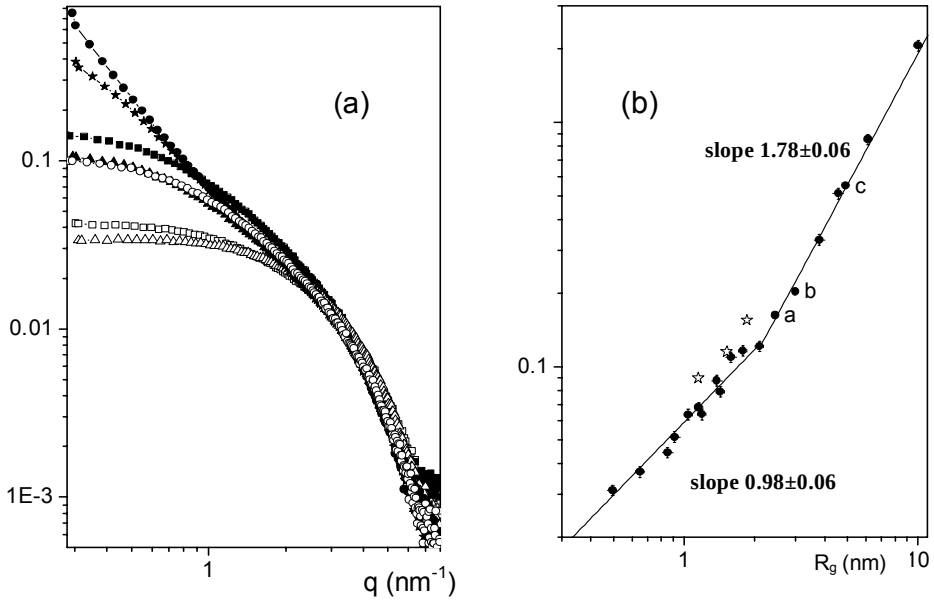

Fig. 18: Sulfate-zirconia sols with different HNO_3, H_2SO_4 and H_2O contents. (a) Scattering intensity of a few selected samples inside a sealed cell in their final aggregation state. (b) Plot of I(0) vs. R_g, in log-log scale, corresponding to the final states of sols with different H_2SO_4 contents [19].

The slope D≈1 of the log I vs log R_g plots, for small R_g, suggested that the aggregation process in all the studied sulfate-zirconia sols starts by the formation of short linear chains. This precursor regime is followed by another involving the cross-linking of the chains that leads to a three-dimensional fractal structure. Values of D close to 1.8, as those experimentally determined, are expected for diffusion limited cluster aggregation (DLCA). It was also concluded that, even though the sizes of the final aggregates in sols with a number of different compositions are different, the mechanism of growth in all of them is essentially the same.

6.5.2. Multilevel hierarchical structure. Structure of Fe doped organic-inorganic nano-hybrids

A SAXS study of organic-inorganic nanohybrid materials named di-ureasils doped with Fe(II) was reported by Silva et al [22]. These nanostructured materials have interesting magnetic properties that can be tailored by an adequate control of the preparation conditions, their structural characterization being necessary in order to explain the magnetic behavior. The structure of the undoped hybrids can be well described by a two-electron density model consisting of isolated and spatially correlated siliceous colloidal particles or clusters embedded in a polymeric matrix [15]. The associated SAXS patterns are characterized by a correlation peak located at a decreasing q value for increasing molecular weight of the polymer molecule.

Fig. 19 displays the scattering intensity produced by a di-ureasil hybrid doped with 0.76 weight % Fe(II). In order to describe the structure of the Fe(II) doped nano-hybrids, the multilevel model proposed by Beaucage [20] was applied. The SAXS intensity corresponding to the fine structure level

is dominated by a cluster-cluster correlation peak centered at q=0.15 $Å^{-1}$ that is also observed for the undoped samples. For the doped hybrid, this peak is slightly shifted towards higher q. For q<0.1 $Å^{-1}$ the scattering intensity is mainly associated with a coarser structure. The modeled scattering curve given by Eq. 94 for two structure levels, including the structure function S(q) for the fine structure given by Eq. (80), is indicated in Fig. 19 as a continuous line. Fig. 19 also displays the Guinier and Porod contributions to the total scattering intensity corresponding to both levels and the oscillatory structure function. The radii of gyration R_g obtained by the best fit procedure are 7.5 Å for the small clusters and 54 Å for the coarse domains.

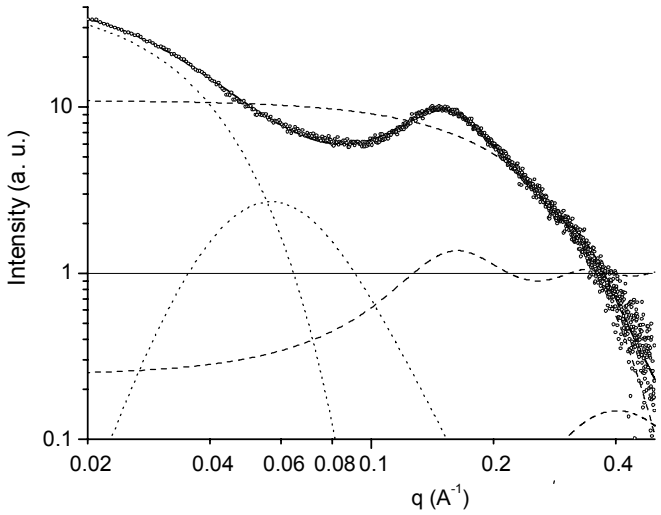

Fig. 19: Fe(II) doped di-ureasil hybrids. Experimental scattering intensity from a sample containing 0.76 weight % Fe(II). The continuous line is the best fit of Eq. 94 to the experimental curve. The dashed lines indicate the Guinier and Porod contributions to the scattering intensity produced by siliceous clusters and the structure function (oscillatory curve). The point lines are the Guinier and Porod contributions to the scattering intensity yielded by the coarse domains [22].

Similar analyses of several SAXS curves for different Fe(II) doping levels, up to 4.5 weight%, indicated that the average distance between silicious clusters decreases for increasing Fe(II) doping [22]. The reported results suggested that the Fe(II) ions are dispersed in the polymeric matrix and that they induce a retraction effect that leads to the observed decrease in the average inter-cluster distance. The formation of the coarse domains was assigned to a phase separation process promoted by the addition of Fe(II) ions. The domains with relatively high silicious particle and Fe(II) concentrations (and thus with a high electron density) are assumed to be embedded in a silicious/Fe(II) depleted region. An alternative interpretation would be the independent segregation of Fe(II) ions forming rather large Fe(II)-rich aggregates of high electron density dominating the scattering intensity below q=0.15 $Å^{-1}$.

7. Nano-phase separation

Nanohetereogeneous materials are formed by phase separation processes starting from a unstable supersaturated solution brought into a miscibility gap by fast quenching. When the supersaturated solution is close to the binodal curve (the solubility limits), the transformation occurs through the mechanism of nucleation and growth of a minor new phase. This leads to a two-phase material composed of isolated amorphous or crystalline clusters embedded in the solid matrix. The growth of these clusters can generally be characterized by SAXS, using a model of either a dilute or concentrated set of spherical clusters, as described in previous sections.

The issue is more difficult when the composition of the quenched material lies close to the center of the miscibility gap. In this case, the final two-phase system exhibits a bicontinuous geometry, both phases occupying about the same volume fraction, and thus the structure cannot be modeled by a set of isolated nano-objects. Under this condition, a theoretical model that was suggested to describe the nano-phase transformation is named spinodal decomposition [23]. At advanced stages, even after nearly reaching the equilibrium concentrations, both phases still evolve by a coarsening process.

The subject to be addressed now is how the results of in situ SAXS measurements during phase separation can be applied in order to verify the correctness of the proposed theoretical models.

7.1. Early stage of nano-phase separation.

Spinodal decomposition is a diffusion process that describes nano-phase separation under isothermal conditions in an initially homogeneous material brought by fast quenching into the central part of a miscibility gap. A linear diffusion equation was derived by Cahn [23] that is expected to hold for the early stages of the process. This equation applies to isotropic materials and includes a composition gradient term that accounts for a "surface" energy contribution coming from the incipient interfaces that start to develop during the first stages of phase separation. Cahn equation yields the time dependence of the Fourier components $\eta(k,t)$ of the time varying electron density function, characterized by a wave-number k. As we have seen in section 2 (Eq. 6 and 11) the magnitude of the Fourier wave-vector k is equal to the modulus of the scattering vector q. On the other hand, the function $\eta(k,t)$ is proportional to the X-ray scattering amplitude A(q,t). Thus the time dependence of the experimental SAXS intensities I(q,t), for each q value, is proportional to $[\eta(k,t)]^2$.

According to the solution of the linear Cahn equation, and taken into account the arguments stated above, the time dependence of the small-angle scattering intensity for each q value results

$$I(q,t) = I(q,0).e^{2R(q)t} \qquad (95)$$

where R(q) is an amplification factor given by

$$R(q) = -D.q^2\left(1 - \frac{q^2}{q_c^2}\right) \qquad (96)$$

D being an effective atomic diffusion coefficient, which is negative for phase separating systems ("up-hill" diffusion). Eqs (95) and (96) indicate that the function R(q) is positive within the range $0<q<q_c$ and negative for $q>q_c$, as shown in Fig. 20a. Thus the scattering intensity is expected to grow exponentially for for $q<q_c$ and to decrease also exponentially for $q>q_c$,. The maximum growth rate occurs at $q=q_m$, q_m being related to q_c by

$$q_c = \sqrt{2}.q_m \qquad (97)$$

For $q=q_c$ the growth rate is zero so that, for this particular q value, the intensity is time invariant. For a series of SAXS curves, corresponding to increasing isothermal annealing times, the existence of a critical q value $q=q_c$ can clearly be observed as a crossover of all scattering intensity curves (Fig. 20b). Another feature that is expected from the linear Cahn theory for a set of successive scattering curves is a well-defined maximum at a time independent q value, $q=q_m$, this value corresponding to the maximum of the amplification factor R(q). These features were experimentally observed in phase separation processes of many materials. At more advanced stages, a continuous shift of the maximum of the SAXS curves toward small q values is experimentally observed, so implying that the structure coarsens and the linear Cahn equation does not longer apply.

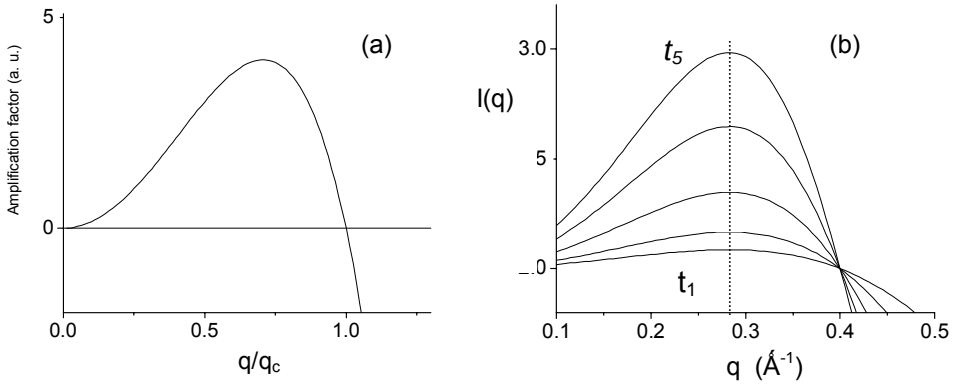

Fig. 20: Spinodal decomposition. (a) Amplification factor R (Eq. 96). (b) Scattering curves for a model system during early times of isothermal nano-phase separation. Time periods increase from bottom to top.

For a number of materials, the simple relation $q_c = \sqrt{2}.q_m$ (Eq. 97) was not experimentally verified. Instead, it was observed that q_c is larger than $\sqrt{2}.q_m$, this deviation being later accounted for by a modified Cahn equation that includes an additional term corresponding to the contribution of statistical fluctuations in electron density.

7.2. Advanced stages of nano-phase separation.

In order to describe the advanced stages of nano-phase separation (i.e the coarsening regime) a statistical model has been proposed [24]. This model assumes that the binary system is composed of A and B atoms arranged in a simple cubic lattice and is described by an occupation function $\eta(r_i)$ that takes the value +1 or –1 when the site r_i is occupied by an atom A or B, respectively. A probability function for atom interchanges and a simple equation for the energy of the system were proposed. This model is analogous to that used for ferromagnetic Ising spin systems. Finally, the theoretical time-dependent structure function for isotropic systems, S(q,t), has been calculated by computer simulation. Taking into account that in this model the scattering objects are atoms, $I_1(q)$ can be approximated *at small q* by a constant value, so that the SAXS intensity can be written as

$$I(q,t) \propto S(q,t) \qquad (98)$$

This statistical model leads to remarkably simple results for advanced stages of phase separation, when the two phases have nearly reached the final electron concentration and volume fractions. Under these conditions the integral of the scattering intensity Q (Eq. 27) becomes time independent and the pure coarsening process starts. The results of computer simulations [24] for the coarsening regime indicate that the time dependent structure function, and thus the experimental scattering intensity, the different moments $S_n(q,t)$ and $I_n(t)$, and the normalized moments $q_n(t)$ defined by

$$I_n(t) = \int_0^\infty q^n(t).I(q,t)dq\,, \quad S_n(t) = \int_0^\infty q^n(t).S(q,t)dq \quad \text{and} \quad q_n(t) = \left[\frac{\int_0^\infty q^n(t).I(q,t)dq}{\int_0^\infty I(q,t)dq}\right]^{1/n} \qquad (99)$$

exhibit the following properties:

i)The scattering intensity curves I(q,t) and the structure functions S(q,t) corresponding to different annealing times (Fig. 21a) display a so-called dynamical scaling property evidenced by the existence of a characteristic time-independent function F(x) (Fig. 21b) expressed as

$$F(x) = \frac{S(q,t)}{S_2}\left[q_1(t)\right]^3 \qquad \text{or} \qquad F(x) = \frac{I(q,t)}{I_2}\left[q_1(t)\right]^3 \tag{100}$$

where $x = (q/q_1)$. Since I_2 and S_2 are proportional to the invariant Q (Eq. 27), these moments are time-independent.

ii)The normalized first moment of the scattering intensity function, $q_1(t)$, has a power time dependence:

$$q_1(t) \propto t^{-a} \tag{101}$$

the exponent *a* depending on the detailed mechanism of aggregation.

iii)The maximum of the structure function $S(q_m,t)$ and thus that of the scattering intensity $I(q_m, t)$ exhibit a time dependence given by

$$S(q,t) \propto I(q_m,t) \propto t^{a'} \qquad \text{with } (a'/a)=3 \tag{102}$$

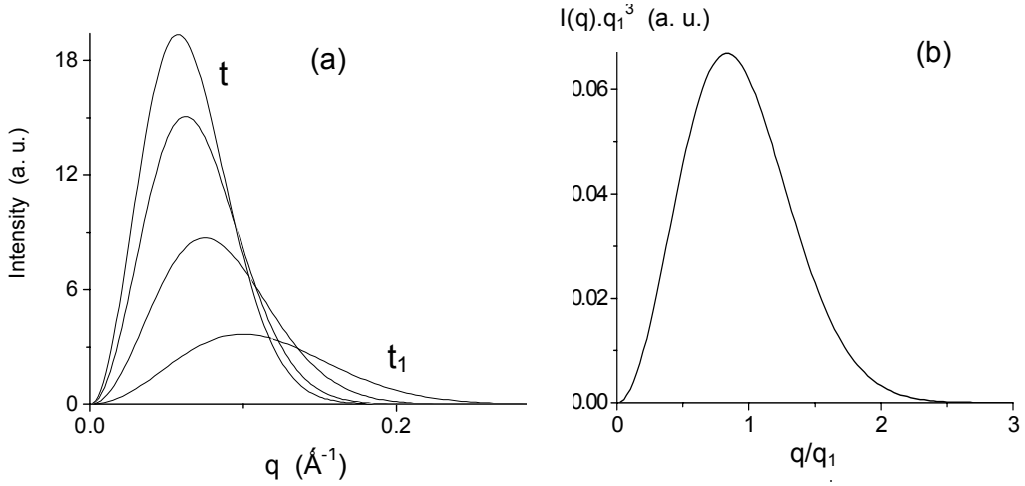

Fig. 21: Dynamical scaling property. (a) Different scattering intensity curves from a system in advanced stages of nano-phase separation for increasing periods of isothermal annealing from t_1 to t_4. (b) Scaled structure function, $\left[I(q)q_1^3\right]$ vs. (q/q_1).

In addition, all other moments and normalized moments are also connected by simple relations. A number of investigations using small-angle (X-ray or neutron) scattering have demonstrated the dynamical scaling properties for a number of different nanoheterogeneous systems, such as crystalline-crystalline [25], amorphous-amorphous [26] and nanoporous materials [27].

7.3. In situ study of nanoporous SnO_2-based xerogels

The theories that were described in section 7.2 referring to classical phase separation processes were applied by Santilli et al [27] to an in situ SAXS study of the time evolution under isothermal condition of the nano-porosity developed in SnO_2 xerogels. This nanoporous material, after a short period, preserves its apparent density thus suggesting that the total fraction of porous volume remains constant during the advanced stages of isothermal annealing.

The series of scattering intensity curves corresponding to a SnO_2 xerogel isothermally annealed at 400C, displayed in Fig. 22a, exhibit a peak whose q position progressively shifts toward smaller q values indicating the coarsening of the nanoporous structure [27]. This qualitative feature is expected from the statistical model that predicts the dynamical scaling property (section 7.2). The SAXS results displayed in Fig. 22b, in which the scattering curves shown in Fig. 22a are replotted in a $[S(q,t)q_1^3/S_2]$ versus (q/q_1) scale, indicate that the dynamical scaling property of the nanoporous structure is quantitatively verified.

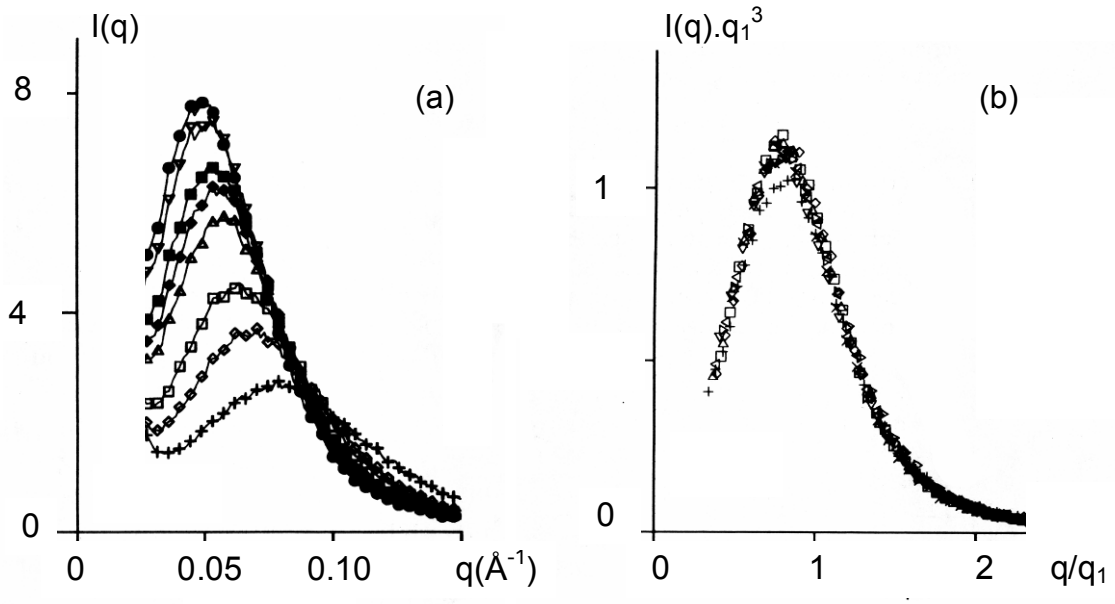

Fig. 22: SnO_2 based porous xerogels. (a) Scattering intensity curves corresponding to a nanoporous SnO_2 xerogel held at 400C during increasing periods of time from 4.5 min. (bottom) up to 62.5 min (top) [27]. (b) Same curves plotted as $[S(q,t)q_1^3/S_2]$ versus (q/q_1).

In the same work [27], the authors also demonstrated that, at lower temperatures (T=300C) and during the first stages of pore growth, the maximum of the scattering intensity remains at the same q value. This result is expected from the solution of the linear Cahn equation for spinodal composition [23].

The overall conclusion was that the Cahn model for spinodal decomposition and the statistical theory that predicts the dynamical scaling property of the structure function, derived for simple crystalline binary solid solutions, also applies to the structural transformations in nanoporous xerogels during isothermal annealing.

7.4. Fractal clusters in a homogeneous medium

Materials consisting of a concentrated set of fractal aggregates embedded in a homogeneous solid or liquid matrix may also exhibit the dynamical scaling property. In this case, Eqs (100), (101) and (102) are still expected to hold but the exponent in Eq. (100) and the quotient (a'/a) in Eq. (102) are the fractal dimension D instead of 3.

An experimental demonstration of the dynamical scaling property for a system consisting of zirconia-based fractal aggregates embedded in a liquid matrix was reported by Lecomte et al. [21]. These auhors performed the in situ SAXS study of the formation and growth of zirconia-based sols that was described in section 6.5.1. The scattering curves displayed in Fig. 17 exhibit an increasing

maximum that shifts progressively toward lower q for increasing periods of time. The fractal dimension derived from the scattering results was D=1.7. The same set of curves displayed in Fig. 17 is replotted in Fig. 23 using a $[I(q/q_m)q^{1.7}]$ versus (q/q_m) scale. The authors have here considered that the first normalized moment q_1 can be replaced as a reasonable approximation by the position of the maximum, q_m, and that I_2 is time independent. It is readily apparent that all different scattering curves merge in a single scaled one thus demonstrating the dynamical scaling property for the studied system.

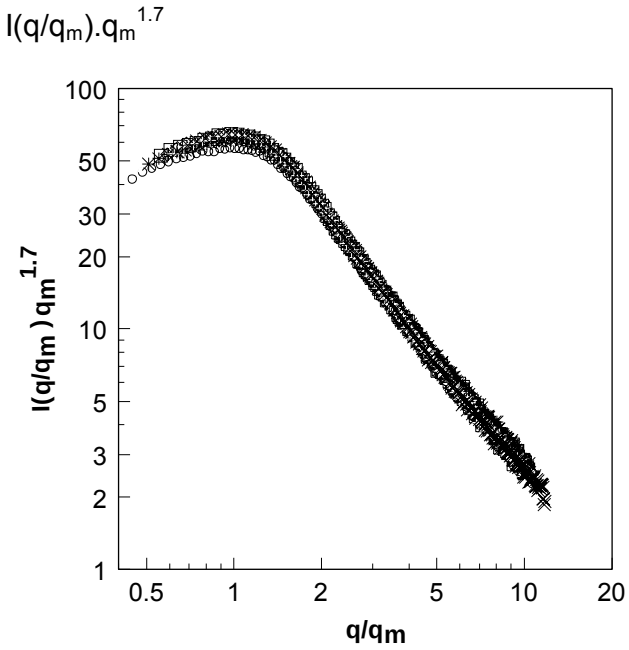

Fig. 23: Scattering intensity curves displayed in Fig. 17 here replotted as $[I(q)q_m^{1.7}]$ versus (q/q_m) [21], q_m being the q value corresponding to the maximum of the scattering curves.

This result together with those mentioned in the preceding sections suggest that the statistical model for nano-phase separation and the dynamical scaling property [24] exhibit universal features that allow for a unified and clear description of nano-phase separation and aggregation processes in a wide variety of materials. On the other hand, the experimental results displayed in Fig. 17, 18 and 23 illustrate the usefulness of in situ small angle X-ray scattering experiments for a direct verification of the correctness of general theories that predict the time variation of the structure function when applied to materials prepared by the sol-gel procedure.

8. Miscellaneous

8.1. Grazing incidence small-angle X-ray scattering (GISAXS)

8.1.1 Basic concepts

Thin films deposited on solid substrates, like those prepared by dip coating with liquid sol precursors, deserve the attention of many scientists because of their often interesting technological properties. These films usually have a thickness ranging from a few nanometers up to a few microns. Many films are not fully homogeneous. Some are composed of a matrix containing isolated nano-clusters spatially correlated or not and often they exhibit anisotropic features. Others are nanoporous. The features of the nano-clusters or nano-pores cannot be studied using the classical transmission small-angle X-ray scattering technique because the substrates are generally thick. Thus, for these mounted films, the grazing incidence small-angle X-ray scattering (GISAXS) technique is applied [28].

This technique probes a sample volume much larger than in classical transmission SAXS experiments, this feature being particularly useful for the analysis of very thin films.

The schematic geometry of a GISAXS setup is shown in Fig. 24a. The X-ray penetration depth Δy - the distance from the surface to the plane where the beam intensity I_0 is decreased by absorption down to I_0/e - defines the thickness of the film layer that is probed in GISAXS measurements. If the incidence angle α (Fig. 24a) is close to the critical angle for total X-ray reflection α_c (typically a few milliradians), the refracted beam travels parallel to the external surface and its penetration is very small (a few to about ten nanometers depending on the average film composition and density). If a thicker layer needs to be probed, the incidence angle α should be set slightly higher than α_c. For $\alpha>\alpha_c$ the penetration depth is $\Delta y=\sin\alpha/\mu$, where μ is the linear X-ray absorption coefficient.

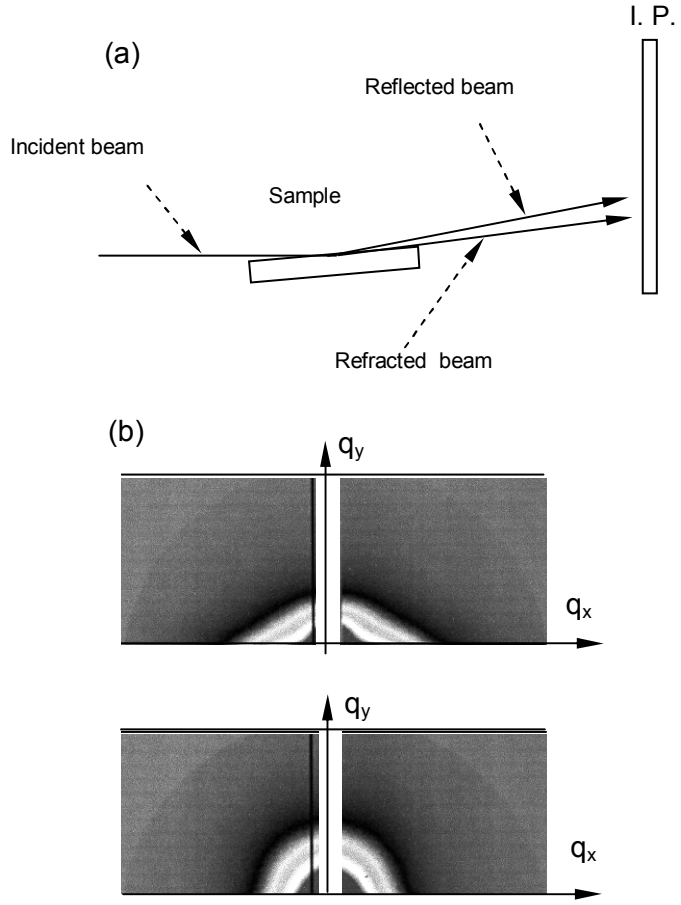

Fig. 24: Zn-based thin films. (a) Schematic GISAXS setup. (b) GISAXS patterns recorded with an image plate for In-doped ZnO-based films prepared by the pyrosol procedure [29]. Top: Film deposited on a glass substrate at 350C. Bottom: Film deposited on a glass substrate at 450C. A vertical beam-stopper attenuates the intense X-ray specular reflection.

Nanoheterogeneous thin films produced by sol dip coating can be well characterized by combined X-ray reflectivity and GISAXS measurements. Reflectivity measurements yield the thickness and average mass density of the films and GISAXS provides relevant information about their structure at a nanometric scale. If the films are very thin (~ a few nanometers thick) the scattering intensity is very

weak and thus only GISAXS setups installed in synchrotron beam lines allow for the recording of useful patterns within reasonable time periods.

8.1.2 GISAXS study of nanoporous In-doped ZnO thin films and metal clusters in glass surface layers.

The GISAXS technique was applied to a structural characterization of nanoporous ZnO-based thin films deposited on a glass substrate by the pyrosol method [29]. The films were deposited at different temperatures from 300C up to 450 C. Fig. 24b display two GISAXS patterns recorded with an image plate corresponding to films that were deposited at 350 and 450C. The intensity profiles of the GISAXS intensity were recorded along narrow strips close to the shadows of the beam-stopper along the x and y directions and, in the analysis, it was assumed that the nano-pores are not spatially correlated. We can notice that the pattern corresponding to the film deposited at 350 C is clearly anisotropic suggesting that the nano-pores are elongated with their major axis perpendicular to the external surface of the substrate. On the other hand, the GISAXS pattern for a deposition temperature T=450 C is isotropic so indicating a porous structure without preferred orientation.

The GISAXS pattern corresponding to the film deposited on a substrate at 350C was analyzed along the x and y directions. The Guinier plot along the x direction yielded a pore radius of inertia (Eq. 50), parallel to the surface of the film, equal to 13 Å. Along the y direction, perpendicular to the surface, a similar Guinier plot indicated a wide size distribution, with radii R_y ranging from 10 up to 35 Å. The same analysis corresponding to the isotropic film deposited at 450C indicated a wide dispersion in pore sizes. The clear differences observed in the two analyzed patterns demonstrated that the characteristics of the nano-porosity of the studied ZnO thin films strongly depend on the deposition temperature.

Many other thin films containing a variety of nano-objects were also characterized by GISAXS. For example, Cattaruzza et al [30] studied the formation by ion implantation of spherical Cu-Ni clusters in thin glass surface layers. The experimental GISAXS patterns that these authors obtained are isotropic and exhibit a peak due to the spatial correlation of the metal clusters. In order to determine the relevant structural parameters, the experimental GISAXS curves were modeled in the same way as in classical SAXS, using the form factor for spheres, a simple theoretical structure function as those described in section 6.2, and a single-mode analytical radius distribution function.

8.2. Anomalous scattering

The anomalous small-angle X-ray scattering technique (ASAXS) can be used to study three-phase materials, two of the phases being isolated nano-objects. In many cases these structures cannot be characterized using a simple two-electron density model. The ASAXS technique applies the known characteristic of the strong variation in the atomic scattering factor for X-ray wavelengths close to the λ_K or λ_L absorption edges. Anomalous scattering experiments require the determination of two or more scattering intensity curves using different X-ray wavelengths. One wavelength is chosen far from the absorption edge of the selected element and another very close to it. The difference between both curves yields particularly useful information when the selected “anomalous” atom is concentrated only in one of the isolated nano-phases.

ASAXS has been applied to the characterization of catalysts consisting of metal clusters embedded in nanoporous substrates [31]. The difference between the SAXS curves, corresponding to wavelengths far from and close to the metal absorption edge, only depends on the size, shape and spatial correlation of the metal clusters thus suppressing the strong contribution from nano-pores. In ASAXS measurements the intensity is usually expressed in absolute units and should be very precisely determined in order to perform properly the curve subtractions. In order to improve the quality of the final data, more than two scattering curves, using several X-ray wavelengths, are recorded. This is particularly necessary and useful if the metal is a minor component only occupying a very small fraction of the total sample volume.

8.3 SAXS setups

8.3.1. Classical cameras

The basic requirements of a classical experimental setup for small-angle X-ray scattering are (i) possibility of measuring the scattering intensity down to very small angles, (ii) low parasitic scattering from the slits and from the air irradiated by the incident beam, and (iii) intensity of the incident beam, and thus of the scattered intensity, as high as possible.

The simplest systems utilize a filtered X-ray Cu Kα beam, provided by a sealed or a rotating anode source, with a linear cross-section. The cross-section of the incident beam is defined by three sets of slits, as shown in Fig. 25a. Slit S_1 has a width similar to the apparent width of the source line and is located as close as possible to the tube exit window, S_2 defines the (small) divergence of the beam and S_3, a guard slit located as close as possible of the beam without touching it, suppresses the usually strong parasitic scattering produced by S_2. Typical widths of slit S_1 and S_2 are around 100 μm, their values depending on the minimum angle to be reached in the scattering measurements. A reduction of slit openings induces a decrease in the minimum angle to be reached but also diminishes the number rate of photons in the incident beam. A more detailed description of the geometry of the classical setup is given in [32].

In more complex setups, a cylindrically bent crystal monochromator is inserted close to the X-ray source in order to (i) suppress most of the white radiation only keeping the Kα emission and eventually a few harmonics, and (ii) focus the initially divergent incident beam at the detection plane.

A commercially available SAXS setup, named as Kratky camera, is used in many laboratories. In this camera, whose basic geometry is shown in Fig. 25b, a block system was designed in such a way to strongly reduce the parasitic scattering in one side of the incident beam down to very low scattering angles [32].

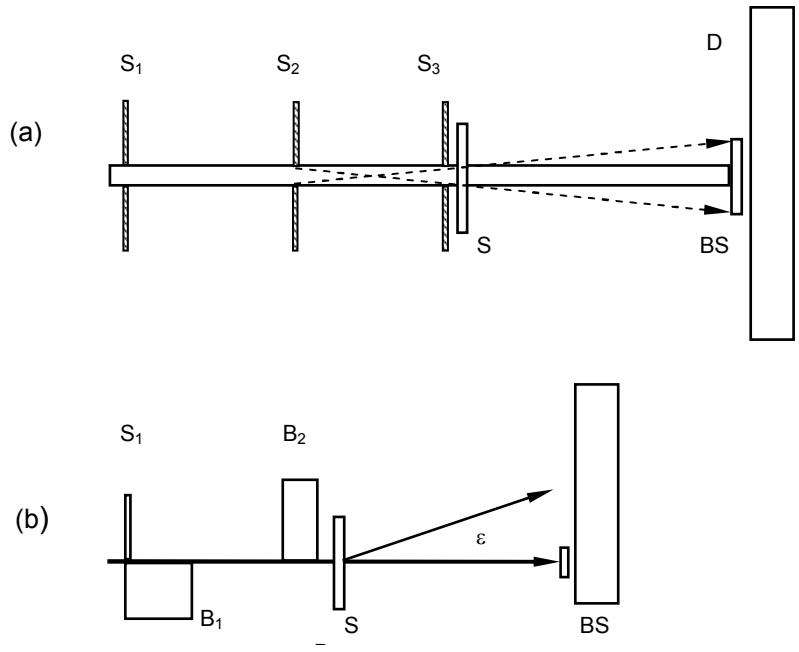

Fig. 25: Classical SAXS setups. (a) Standard slit setup with slit collimation. The dashed lines indicated the limit of the angular range with high parasitic scattering. (b) Kratky slit setup. The main components of both setups are slit sets (S_n), sample holder (S), beam-stopper (BS) and detector (D). B_1 and B_2 (metallic blocks) are components specific of the Kratky camera [32].

8.3.2 Synchrotron SAXS beam lines

Most the synchrotron laboratories around the world, with electron energy above 1 GeV, have one or more beam lines dedicated to small-angle X-ray scattering experiments. Some are equipped with a two-crystal monochromator that also focuses the beam. Others, in operation in several synchrotron facilities such as LURE (Orsay, France), Photon Factory (Tsukuba, Japan) and LNLS (Campinas, Brazil), utilize a one-crystal monochromator elastically bent for horizontal focusing. In these beam lines, the vertical width of the incident monochromatic beam is defined by horizontal narrow slits to allow reaching very small angles in the scattering measurements. Some SAXS beam lines are also equipped with a cylindrical mirror for vertical focusing.

A layout of the synchrotron SAXS beam line that is in operation from 1997 at LNLS, Campinas, Brazil, is shown in Fig. 26 [33]. The first optical element that the white synchrotron beam emerging from the 1.37 GeV electron storage ring hits is a triangular and elastically bent silicon crystal. When, in order to select the X-ray wavelength, the θ angle is changed, the silicon (111) Bragg reflected beam modifies its direction and thus the bench where the collimating slits, sample holder and detector are placed, is rotated accordingly. The monochromator-to-sample distance is kept constant at d_{ms}=180 cm and the sample-to-detector distance d_{sd} can be varied from 30 up to 200 cm. The useful wavelengths range from 1.30 to 1.90 Å. In one of the possible configurations, a vacuum path (under a pressure of about 10^{-2} Torr) starts at the monochromator exit and end just after the beam stopper, close to the detection plane, without any internal window. This vacuum path totally suppresses the parasitic scattering from air.

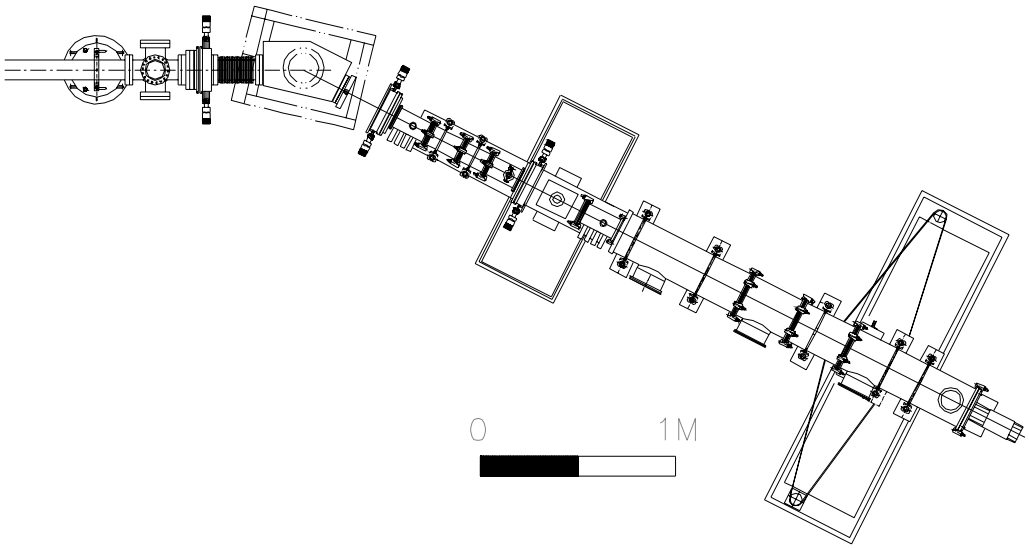

Fig. 26: Layout of the LNLS SAXS beamline [33]. From left to right: slit set, crystal monochromator, slits (2 sets), sample holder, and, at the end of the beam line, beam-stopper and gas detector or image plate. The vacuum path starts just after the monochromator and ends near the detector.

A sealed cell can be used for in situ studies of liquid solutions. This cell is filled and emptied externally, without breaking the vacuum of the beam path volume, and can be heated by water circulation for in situ SAXS studies at temperatures up to ~90C. Another camera can be inserted for studies of solid samples up to approximately 900C, thus allowing for in situ high temperature investigations of structural transformations under isothermal conditions. The high temperature

attachment is windowless over the whole incident beam path and also allows for simultaneous recording of SAXS and WAXS patterns.

8.4. Experimental procedures and data treatment

8.4.1.Sample thickness

Materials studied by classical transmission small-angle X-ray scattering are rather thin plates with parallel external faces or, in the cases of liquid samples, they are confined inside a cell with parallel and very thin windows. The maximum scattering intensity that a given sample may yield corresponds to an optimal thickness that depends on the chemical composition and the wavelength used. The SAXS intensity is proportional to the sample volume or, for a beam of constant cross-section, to the thickness, x, of the sample. Since the scattered beam is attenuated by a factor exp(-μx), where μ is the linear X-ray absorption coefficient, the scattered intensity is proportional to $x.e^{-\mu(\lambda)x}$, this function having a maximum for $x_{id}=1/\mu$. Since the variation of I(q) near the maximum is not very steep, sample thicknesses from about 1/3 to 3 times x_{id} are acceptable. Very thick samples should not be used in order to avoid an eventual too large relative contribution from harmonics in a crystal monochromatized beam or from the hard part of the white spectra in a Kα filtered beam, which may produce spurious effects in the scattering curves. Typical ideal sample thicknesses for CuKα radiation (λ= 1.54 Å) are about 20 μm for Cu, 130 μm for silica glass and ~1 mm for simple polymers and water.

8.4.2. Suppression of the parasitic scattering and normalization

The experimental scattering intensity curves obtained using classical or synchrotron setups are generally determined using a 1D or a 2D position sensitive detector. The resulting scattering curves need to be corrected for the effects from (i) the parasitic scattering produced by slits, sample holder windows and air, (ii) the non-homogeneous response of the detector and (iii) the continuous decay in the intensity of the incident beam associated with the decreasing electron current in the electron storage ring.

The parasitic scattering intensity is generally measured in an equivalent experimental condition but without the sample. In the case of colloidal particles in dilute liquid solutions it is preferable to subtract the scattering produced by the pure solvent because, by doing that, the scattering intensity coming from the density fluctuations in the liquid matrix is also suppressed.

In order to properly subtract the parasitic scattering, the total scattering intensity and the parasitic intensity curves should firstly be multiplied by the respective sample attenuation factor A (or divided by the transmittance). This suppresses absorption effects on both curves. The described subtraction and normalization, leading to the scattering intensity in relative (arbitrary) units I(q), is performed using the following equation

$$I(q) = \frac{1}{R(q)}\left\{\left[\frac{I(q)A}{i_0 \Delta t}\right]_T - \left[\frac{I(q)A}{i_o \Delta t}\right]_P\right\} \qquad (103)$$

where the sub-indexes T and P refer to the measurements of total and parasitic scattering, respectively, R(q) is the detector response function, i_0 a function proportional to the intensity of the incident X-ray beam (e. g. the electron or positron current in the synchrotron source) and Δt is the period of data collection.

8.4.3. Smearing effects

All theoretical equations for the scattering intensity presented in this chapter, $[I(q)]_{th}$, assume ideal experimental conditions, i. e. the incident X-ray radiation is monochromatic, the beam has a point-like cross-section and the scattering intensity is measured using a detector with a very small sensitive surface area. If, in a real scattering experiment, these conditions are not fulfilled, smearing effects on

the measured scattering intensity curve, $[I(q)]_{exp}$, may be significant and should be suppressed before further fine analyses.

In most of the SAXS experiments using classical X-ray sources, the predominant smearing effect comes from the rather long length of the linear beam cross-section and/or large width of the detector sensitive window. Synchrotron beam lines usually provide an incident beam with a point-like cross section at the detector plane. In this case, the main factor that may produce a relevant smearing effect is the eventual non-negligible lateral width of the detector window. For typical wavelengths and geometrical conditions, detector slits larger than 1 to 2 mm may produce significant smearing effects, particularly at very low q.

Smearing effects can be suppressed using ad-hoc and commercially available computer packages [34]. Unfortunately, all the developed mathematical procedures also strongly enhance the statistical dispersion of the experimental points. In order to minimize this drawback, the measured scattering intensity curves should be properly smoothed prior to the application of any desmearing program. An alternative method, employed for example in the GNOM package [10], is to mathematically smear the theoretical model function $[I(q)]_{th}$ and then fit the derived function to the as obtained (smeared) experimental curve $[I(q)]_{exp}$.

8.4.4. Scattering intensity in absolute units

The intensity of the incident X-ray beam in SAXS experiments is much higher than the scattered intensity and is difficult to be precisely determined. Therefore most of the published measurements of small-angle X-ray scattering are reported in relative units; e. g. by the I(q) function given by Eq. 103. Nevertheless, the determination of the SAXS intensity in absolute units may yield useful information from solution studies such as the molecular weight of macromolecules and the number density and average electron density of colloidal particles.

The scattering intensity in absolute units or scattering power can be expressed by the specific scattering cross section function given by

$$\frac{d\Sigma(q)}{d\Omega} = \frac{1}{V}\frac{\left(dI(q)/d\Omega\right)}{I_0} \cong \frac{I(q).D^2}{E_0.x.S} \qquad (104)$$

where V is the irradiated sample volume, I_o the photon flux of the incident beam per unit cross section area, E_0 the total photon flux of the incident beam (power per unit time), x the sample thickness and I(q) the number of photons per unit time counted by a small area S of the detector located at a distance D from the sample.

The determination of the total number of photons per unit time in the incident beam, E_0, requires special care because it cannot be precisely measured by directly using a common detector. A method that has been often applied in the past is based on the use of calibrated filters that strongly attenuate the incident beam. This method is not precise enough because of the negative effects related to the strong contribution of hard X-ray harmonics. Another procedure evaluates the intensity of the direct beam by comparing the experimental scattering intensity yielded by the sample to that produced by precisely calibrated standard solid samples, whose scattering intensity is a priori known in absolute units. This method requires a periodic re-calibration of the standard sample.

A third method compares the experimental scattering intensity from the sample to the intensity produced by the statistical fluctuations in electron density of water [35]. The scattering intensity in absolute units can then be expressed as

$$\left(d\Sigma/d\Omega\right)_{sample} = \frac{\left[I(q)\right]_{sample}}{\left[I(q)\right]_{water}}\left[r_e^2 kT\left(\rho_w^2 \chi_w\right)\right] \qquad (105)$$

where $\left[r_e^2 kT\left(\rho_w^2 \chi_w\right)\right]$ is the known scattering cross-section corresponding to the statistical density fluctuations of water, k being the Boltzmann constant, T the absolute temperature and ρ_w and χ_w the average electron density and the isothermal compressibility coefficient, respectively, of water. Both measurements of I(q), corresponding to the sample and to water, should be performed under identical experimental conditions and properly normalized.

Acknowledgment

The author acknowledges S. Ciccariello, J. Teixeira, J. M. Sanchez, N.J.O. Silva and G. Kellermann for useful remarks and comments.

References

1. G. Porod. Small-Angle X-ray Scattering. O. Kratky and O. Glatter, editors. Chapter 2. Academic Press (London, 1982).
2. P. Debye and A. M. Bueche. J. Appl. Phys. 20, 518 (1949).
3. G. Porod. Kolloid Z. 124, 83 (1951).
4. S. Ciccariello. J. A. J. Appl. Cryst. 24, 509 (1991).
5. W. Ruland. J. Appl. Cryst. 4, 70 (1971).
6. S. Ciccariello. J. Appl. Cryst. 35, 304 (2002).
7. C. G. Shull and L.C. Roess. J. Appl. Phys. 18, 295 (1947).
8. A. Guinier and G. Fournet. Small-Angle Scattering of X-rays. Chapter 2. Wiley (New York, 1955).
9. A. Craievich, O. L. Alves and L.C. Barbosa. J. Appl. Cryst. 30, 623 (1997).
10. D. I. Svergun. J. Appl. Cryst. 25, 495 (1992).
11. C. Walker and A. Guinier. Acta Met. 1, 568 (1953).
12. A. F. Craievich, G. Kellermann, LC. Barbosa and O. L. Alves. Phys. Rev. Lett. 89, 235503 (2002).
13. G. Beaucage. J. Appl. Cryst. 28, 717 (1995).
14. M. S. Tokumoto, S.H. Pulcinelli, C.V. Santilli and A.F. Craievich. J. Non-Cryst. Solids. 247, 176 (1999).
15. D. E. Rodrigues, A. B. Brenan, C. Betrabet, B. Wang and G.L. Wilkes. Chem. Mater. 4, 1437 (1992).
16. S.K. Sinha, T. Freltoft and J. Kjems. Kinetics of Aggregation and Gelation. Editors F. Family and D.P. Landau, pp. 87-90. North Holland (Amsterdam, 1984).
17. S. H. Chen and J. Teixeira. Phys. Rev. Lett. 57, 2583 (1986).
18. J. Teixeira. J. Appl. Cryst. 21, 781 (1988).
19. P. Riello, A. Minesso, A. F. Craievich and A. Benedetti. J. Phys. Chem. B. 107, 3390 (2003).
20. G. Beaucage, T. Ulibarri, E.P. Black and D.W. Shaeffer. Hybrids Organic-Inorganic Composites, ACS series, 97, 585 (1995).
21. A. Lecomte, A. Dauger and P. Lenormand. J. Appl. Cryst. 33, 496 (2000).
22. N. J. O. Silva, K. Dahmouche, C.V. Santilli, V.S. Amaral, L.D. Carlos, V. de Zea Bermudez and A.F. Craievich,. J. Appl. Cryst. 36, 961 (2003).
23. J. W. Cahn. J. Chem. Phys. 42, 93 (1965).
24. J. L. Leibowitz, J. Marro and M. K. Kalos. Acta Met. 30, 297 (1982).
25. H. Hennion, D. Ronzaud and P. Guyot. Acta Met. 30, 599 (1982).
26. A.F. Craievich and J.M. Sanchez. Phys. Rev. Lett. 47, 1308 (1981).
27. C.V. Santilli, S.H. Pulcinelli and A. F. Craievich. Phys. Rev. B 51, 8801 (1995).
28. G. Goerigk, H. G. Haubold, O. Lyon and J. P. Simon. J. Appl. Cryst. 36, 425 (2003).
29. M. S. Tokumoto, R. Smith, C.V. Santilli, S. H. Pulcinelli, A.F. Craievich, E. Elkaim, A. Traverse and V. Brois. Thin Solid Films, 416, 284-93 (2002).

30. E. Cattaruzza, F. d' Acapito, F. Gonella, A. Longo, A. Martorana, G. Mattei, C. Maurizio and D. Thiaudiere. J. Appl. Cryst. 33, 740 (2000).

31. H. G. Haubold, X. G. Wang, G. Goerigk, and W. Schilling. J. Appl. Cryst. 30, 653 (1997).

32. O. Kratky. Chapter 3. Small-Angle X-ray Scattering. O. Kratky and O. Glatter, editors. Academic Press (London, 1982).

33. G. Kellermann, F. Vicentin, E. Tamura, M. Rocha, H. Tolentino, A. Barbosa, A. F. Craievich and I. Torriani. J. Appl. Cryst. 30, 880 (1997).

34. B. J. Jungnickel, M . Soliman and E. Meister. Acta Cryst. A 54, 675 (1998).

35. D. Orthaber, O. Glatter and P. Schurtemberg. J. Appl. Cryst. 33, 218 (2000).

SAXS. Basic Aspects

Aldo F. Craievich

Institute of Physics

University of São Paulo

Brazil

(craievich@if.usp.br)

Content

Basic theory and setups for SAXS experiments

Basic reference

“Small-angle X-ray scattering by nanostructured materials”. A. F. Craievich. Handbook of Sol-Gel Science and Technology, Vol II Chapter 8, Kluwer Publishers (2005)

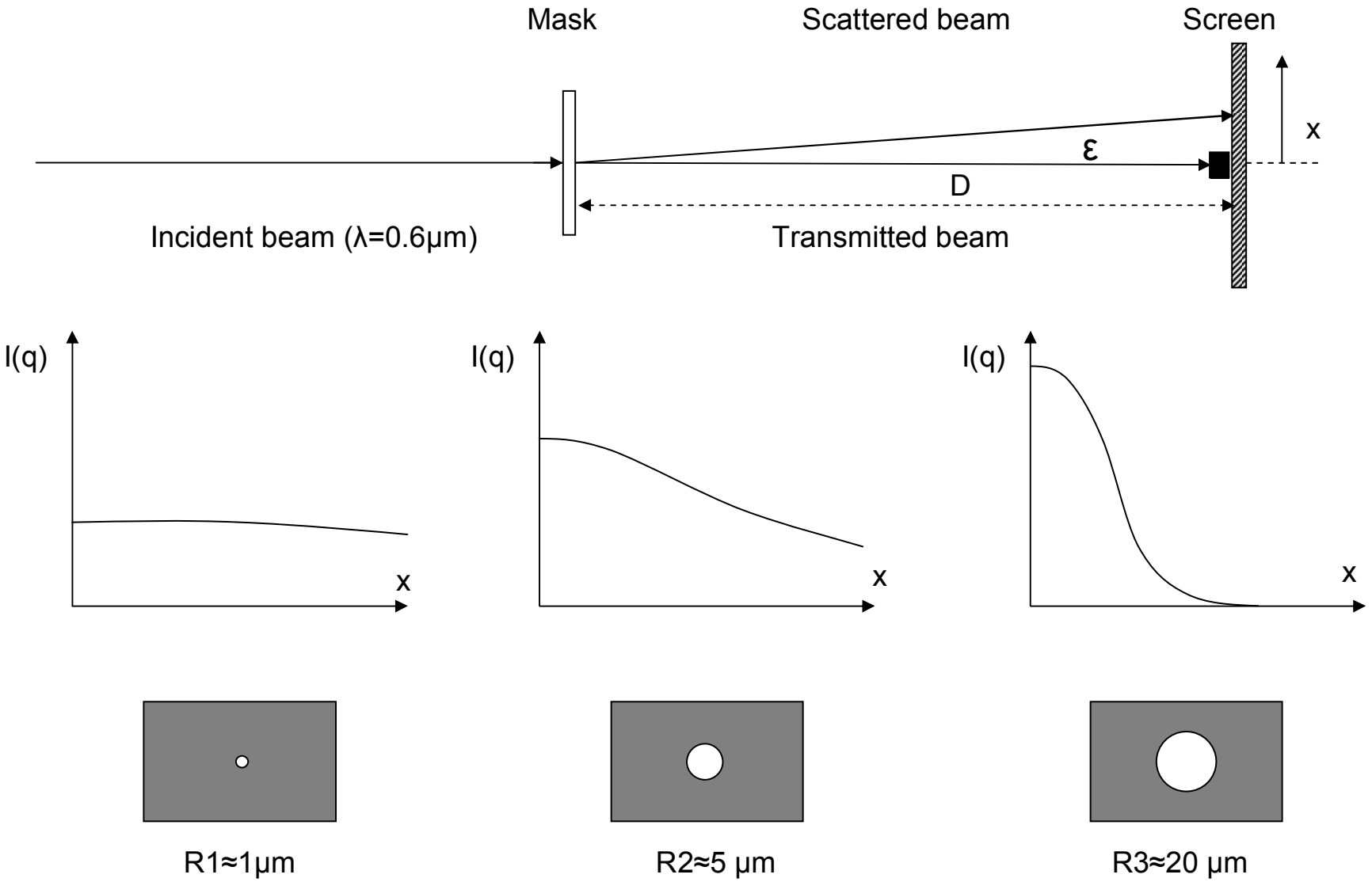
Mask
Scattered beam
Screen
x
ε
D
Incident beam (λ=0.6μm)
Transmitted beam
I(q)
x
I(q)
x
I(q)
x
R1≈1μm
R2≈5 μm
R3≈20 μm

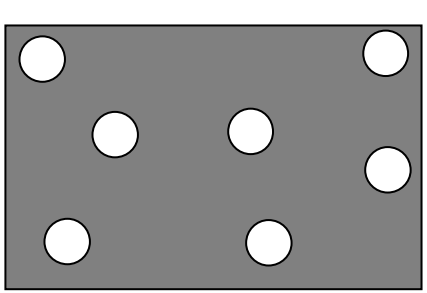

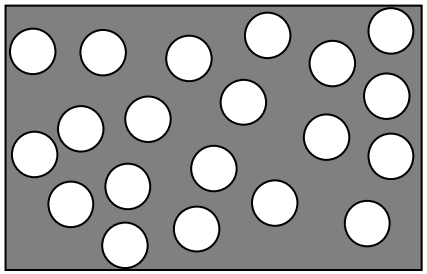

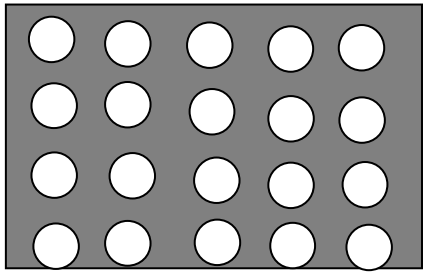

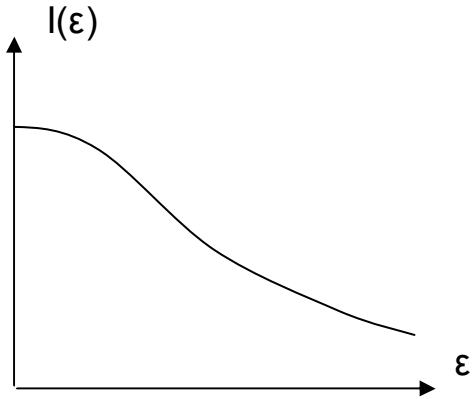
I(ε)
ε

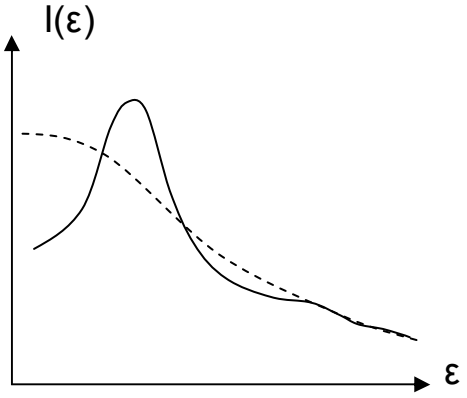
I(ε)
ε

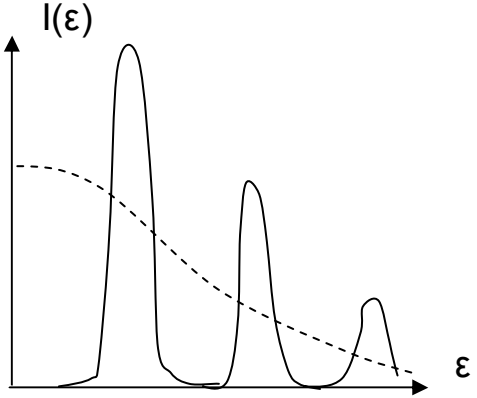
I(ε)
ε

Scattering of x-rays by an electron

$$I_e(2\theta) = I_0 r_e^2 \left(\frac{1+\cos^2 2\theta}{2}\right)$$

$$I_e(2\theta) = I_0 r_e^2$$

$$\Delta s = AB + BC = -(\hat{Q}_0.\vec{r} - \hat{Q}.\vec{r}) \qquad dA(q) = A_e \rho(\vec{r}) d\vec{r} e^{i\Delta\varphi}$$

$$\rho(\vec{r}) = \int [\frac{A(\vec{q})}{A_e}] e^{i\vec{q}.\vec{r}}\, d\vec{q}$$

$$\Delta\varphi = -2\pi \frac{(\hat{Q} - \hat{Q}_0).\vec{r}}{\lambda} = -(\vec{Q} - \vec{Q}_0) = -\vec{q}.\vec{r}$$

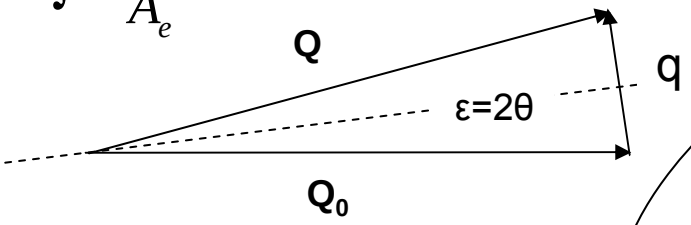

$$\Delta s = AB + BC = -(\hat{Q}_0.\vec{r} - \hat{Q}.\vec{r})$$

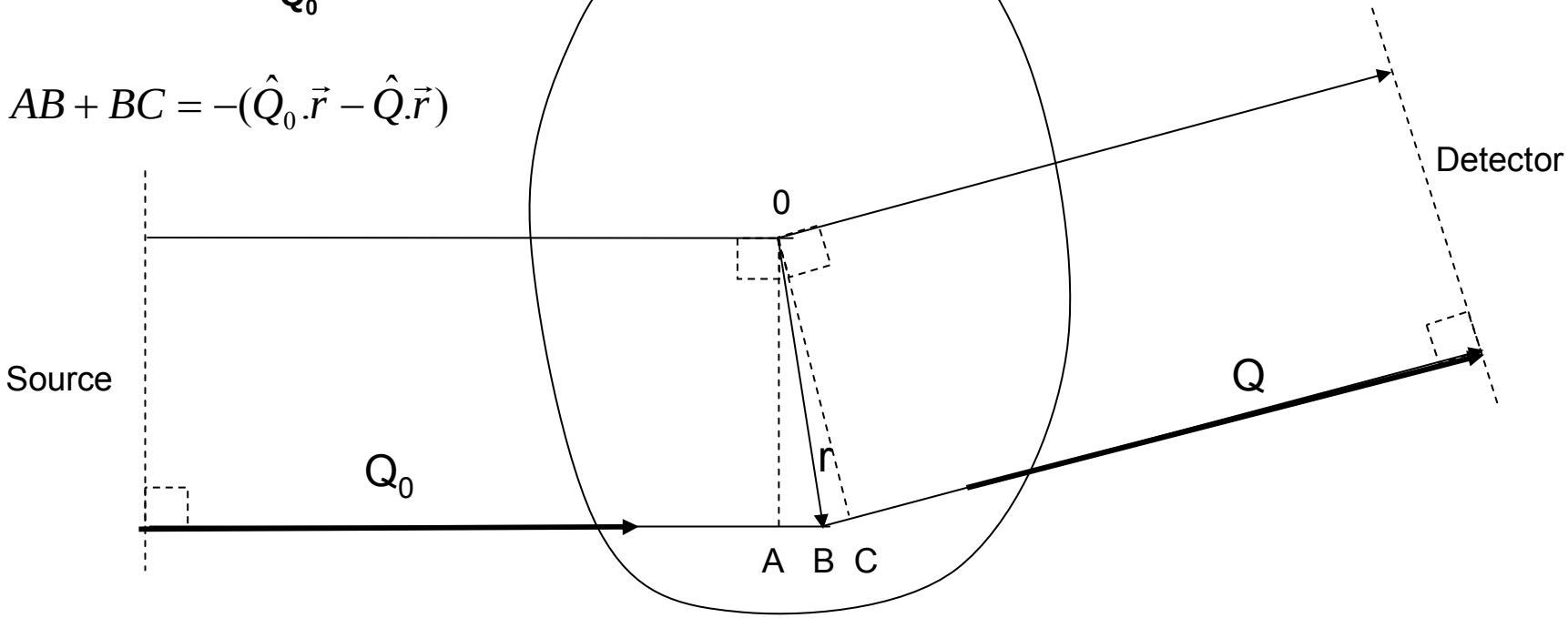

(4)

$$\frac{A(\vec{q})}{Ae} = \int_V \rho(\vec{r}) e^{-i\vec{q}.\vec{r}}\, d\vec{r} \qquad \rho(\vec{r}) = \int [\frac{A(\vec{q})}{A_e}] e^{i\vec{q}.\vec{r}}\, d\vec{q}$$

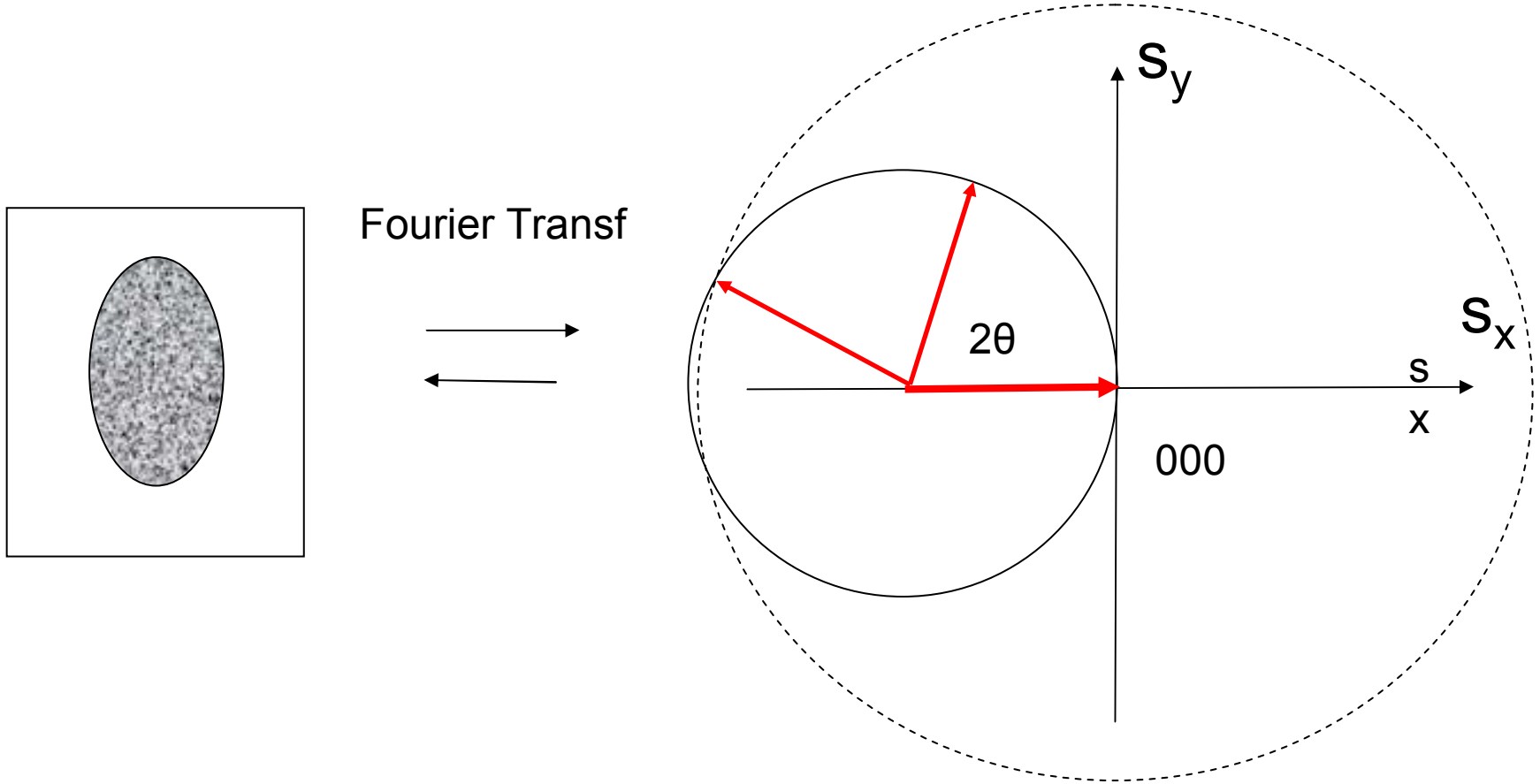
Fourier Transf
S_y
S_x
2θ
s
x
000

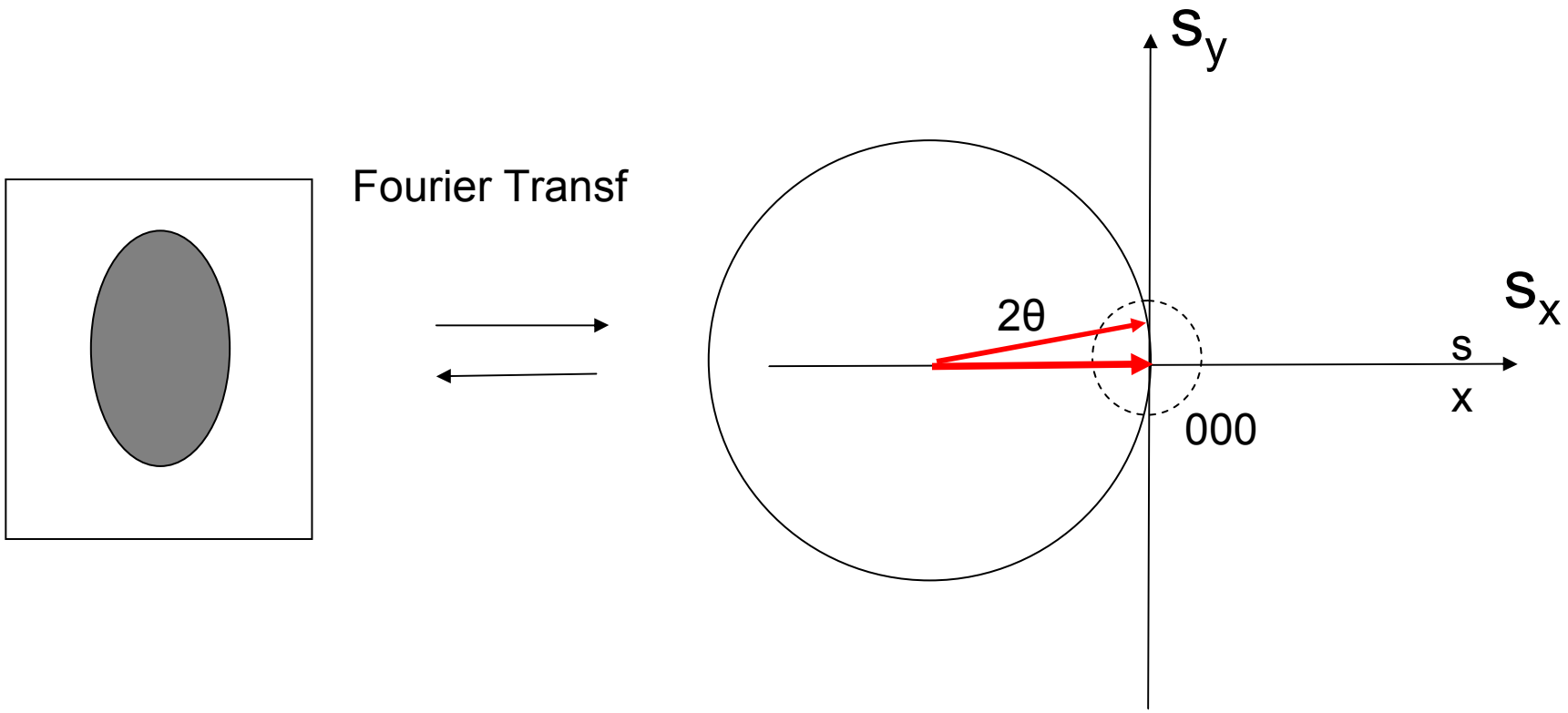
Fourier Transf
S_y
S_x
2θ
s
x
000

- Nanostructured materials:
  macroscopic objects composed of nanometric building blocks

1 nm

- Supported thin films

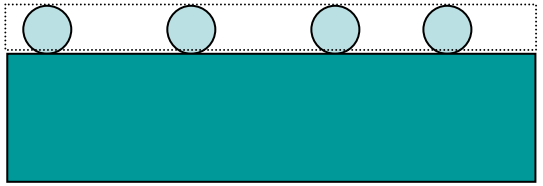

- Volume nanostructured materials

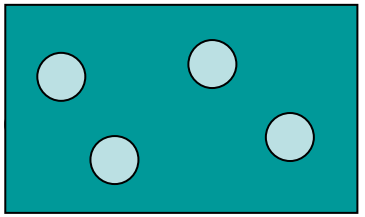

-Properties of nanostructured materials: They strongly depend on the shape and size of the nanometric building blocks.

SHAPE

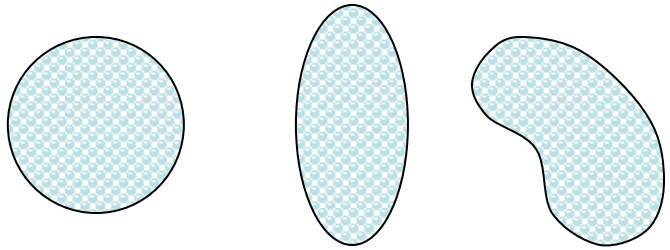

and

SIZE

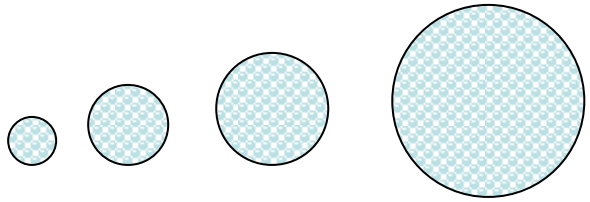

... are relevant structural characteristics.

-Properties of nanostructured materials: They strongly depend on the shape and size of the nanometric building blocks.

SHAPE

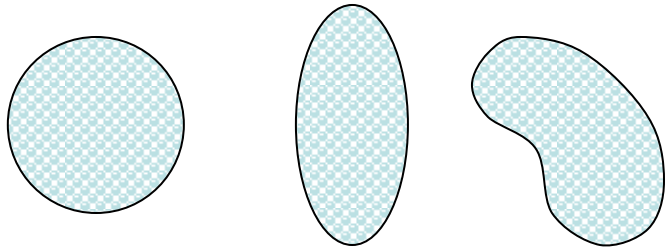

Folding-unfolding of proteins

and

SIZE

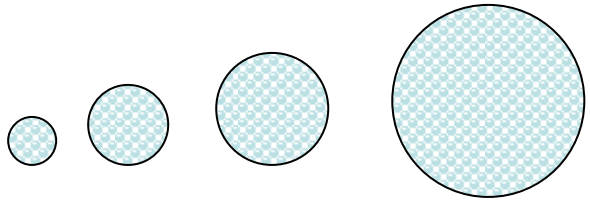

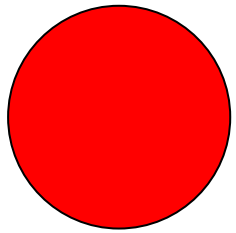

... are relevant structural characteristics.

$$\gamma(\vec{r}) = \frac{1}{I_e}\int I(\vec{q}).e^{i\vec{q}.\vec{r}}\,d\vec{q} \qquad \left|A(q)\right| = \left[I(q)\right]^{1/2}$$

$$\rho(\vec{r}) = \rho_0 + \Delta\rho(\vec{r})$$

$$\frac{\mathrm{A}(\vec{\mathrm{q}})}{A_e} = \int_V \rho_0\, e^{-i\vec{q}.\vec{r}}\,d\vec{r} + \int_V \Delta\rho(r)e^{-i\vec{q}.\vec{r}}\,d\vec{r} \qquad \frac{\mathrm{A}(\vec{\mathrm{q}})}{\mathrm{A_e}} = \int_V \Delta\rho(r)e^{-i\vec{q}.\vec{r}}\,d\vec{r}$$

$$I(\vec{q}) = I_e \int_V\int_V \Delta\rho(\vec{r}_1).\Delta\rho(\vec{r}_2).e^{-iq.(\vec{r}_1-\vec{r}_2)}.d\vec{r}_1 d\vec{r}_2$$

$$\vec{r}_1 - \vec{r}_2 = \vec{r}$$

$$I(\vec{q}) = I_e \int_V\int_V \Delta\rho(\vec{r}_2+\vec{r}).\Delta\rho(\vec{r}_2).e^{-i\vec{q}.\vec{r}}\,d\vec{r}_2 d\vec{r}$$

$$\boxed{I(\vec{q}) = I_e V \int_V \gamma(\vec{r})e^{-i\vec{q}.\vec{r}}\;\,d\vec{r}}$$

$$\gamma(\vec{r}) = \frac{1}{V}\int_V \Delta\rho(\vec{r}').\Delta\rho(\vec{r}'+\vec{r}).d\vec{r}' = \overline{\Delta\rho(\vec{r}').\Delta\rho(\vec{r}'+\vec{r})}$$

Small-angle scattering by a macroscopically isotropic material

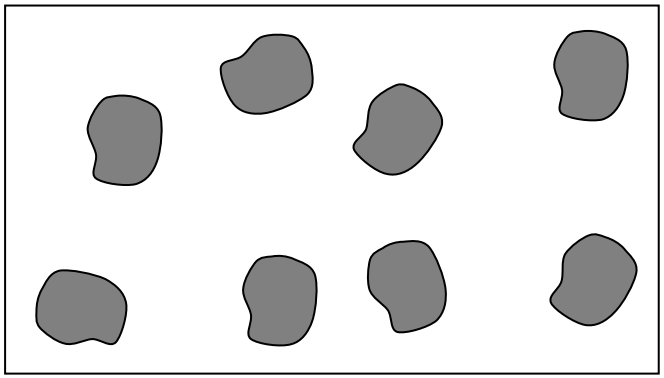

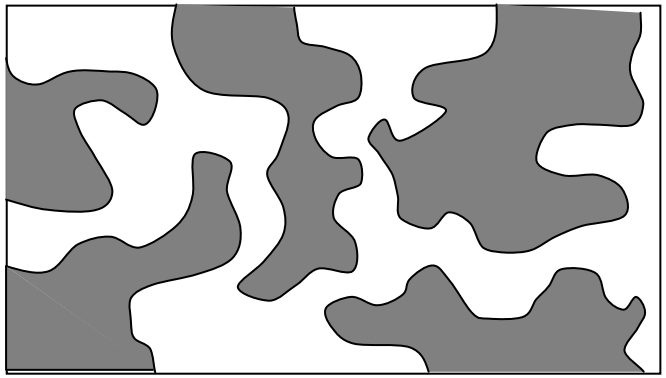

$$\left\langle e^{-i\vec{q}.\vec{r}} \right\rangle = \frac{\sin qr}{qr}$$

$$\gamma(r) = \frac{1}{8\pi^3 V I_e} \int_0^\infty 4\pi q^2 I(q) \frac{\sin q.r}{q.r} dq$$

$$\gamma(0) = \frac{1}{V} \int_V \Delta\rho(\vec{r}).\Delta\rho(\vec{r}).d\vec{r} = \overline{\Delta\rho(\vec{r})^2}$$

$$I(q) = I_e V \int_0^\infty 4\pi r^2 \gamma(r) \frac{\sin q.r}{q.r} dr$$

$$\gamma(0) = \frac{1}{8\pi^3 V I_e} Q$$

$$Q = \int_0^\infty 4\pi q^2 I(q) dq$$

Small-angle scattering by an arbitrary two electron density model

The reduced correlation function

The integral of the scattering intensity in reciprocal space

Asymptotic behavior of scattering curves at high q. Porod equation

$$\gamma(r) = \varphi_1\varphi_2\left(\rho_1 - \rho_2\right)^2 \gamma_0(r) \qquad I(q) = I_e V \varphi_1\varphi_2\left(\rho_1 - \rho_2\right)^2 \int_0^\infty 4\pi r^2 \gamma_0(r) \frac{\sin q.r}{q.r} dr$$

$$\gamma_0(r) = 1 - \frac{S/V}{4\varphi_1\varphi_2} r + \ldots \qquad \gamma_0(r) = \frac{1}{8\pi^3 V I_e \varphi_1\varphi_2\left(\rho_1 - \rho_2\right)^2} \int_{Vq} 4\pi q^2 I(q) \frac{\sin q.r}{qr} dq$$

$$Q = \int_0^\infty 4\pi q^2 I(q) dq$$

$$Q = 8\pi^3 V I_e \varphi_1\varphi_2\left(\rho_1 - \rho_2\right)^2$$

$$\gamma(r) = \varphi_1\varphi_2\left(\rho_1 - \rho_2\right)^2 \left(1 - \frac{S}{4V\varphi_1\varphi_2} r\right) \qquad I(q) = I_e V \varphi_1\varphi_2\left(\rho_1 - \rho_2\right)^2 \int_0^\infty 4\pi r^2 \left(1 - \frac{S.r}{4V\varphi_1\varphi_2}\right) \frac{\sin qr}{qr} dr$$

$$I(q) = \frac{2\pi I_e \left(\rho_1 - \rho_2\right)^2 .S}{q^4}$$

Porod equation

Small-angle scattering of a dilute system of isolated nano-objects.
General equations

The reduced correlation function for a single isolated object

$$I(q) = \sum_{i=1}^{N} I_1(\vec{q}) = N\left[\frac{1}{N}\sum_{i=1}^{N} I_1(\vec{q})\right] \qquad I(q) = N\left\langle I_1(\vec{q})\right\rangle$$

$$\gamma_0(r) = 1 - \left(S_1/4V_1\right)r \qquad \gamma_0(r) = \gamma(r)\Big/\left[(V_1/V)(\rho_1 - \rho_2)^2\right]$$

$$\int_V 4\pi.r^2\gamma_0(r).dr = V_1$$

$$I_1(q) = I_e(\rho_1 - \rho_2)^2 V_1 \int_0^{D_{\max}} 4\pi r^2 \gamma_0(r)\frac{\sin q.r}{q.r}dr$$

$$I(0) = I_e N(\rho_1 - \rho_2)^2 V_1^{\,2}$$

$$V_1 = 8\pi^3\frac{I(0)}{Q}$$

Asymptotic trend of the scattering intensity at small q. Guinier equation

Dilute and monodispersed system (identical nano-objects)

$$I(q) = I_e N(\rho_1 - \rho_2)^2 V_1 \int_0^{D_{\max}} 4\pi r^2 \gamma_0(r) \frac{\sin qr}{qr} d\vec{r}$$

$$I(q) = I_e N(\rho_1 - \rho_2)^2 V_1 \int_0^{D_{\max}} 4\pi r^2 \gamma_0(r).(1 - \frac{q^2 r^2}{6})]dr \qquad (\sin qr/qr) = 1 - (q^2 r^2/6) + \ldots$$

$$I(q) = I_e N(\rho_1 - \rho_2)^2 V_1^2 \left[1 - \frac{q^2}{6}\frac{1}{V_1}\int_0^{D_{\max}} 4\pi r^2 \gamma_0(r) dr\right] = I_e N(\rho_1 - \rho_2)^2 V_1^2 \left[1 - \frac{q^2}{6} R_g^2\right]$$

$$R_g^2 = \frac{1}{V_1}\int_0^{D_{\max}} 4\pi r^2 \gamma_0(r) dr \qquad R_g = \left[\frac{1}{V}\int_V r^2 d\vec{r}\right]^{1/2} = \overline{r^2}$$

$$R_g = \left\{\frac{\int_V \rho(\vec{r}).r^2.d\vec{r}}{\int_V \rho(\vec{r}).d\vec{r}}\right\}^{1/2}$$

$$I(q) = I_e N(\rho_1 - \rho_2)^2 V_1^2 .e^{-\frac{R_g^2 q^2}{3}}$$

Guinier equation

$$R_g = \sqrt{3/5}R$$

$$R_g = \sqrt{(D^2/8) + (H^2)/12}$$

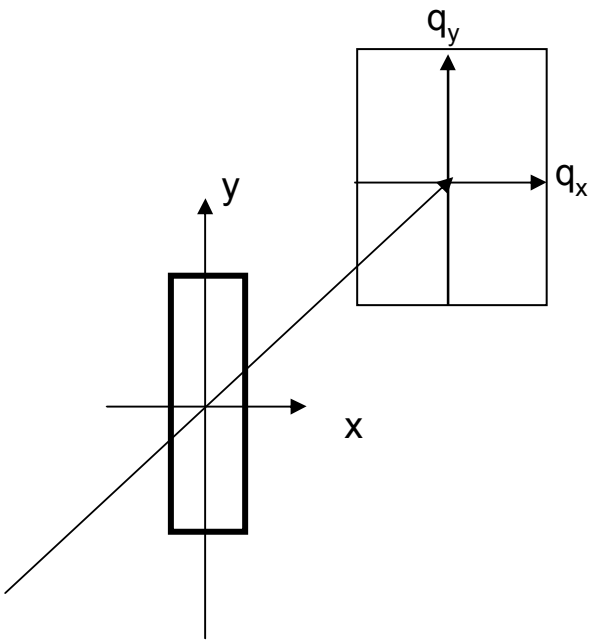

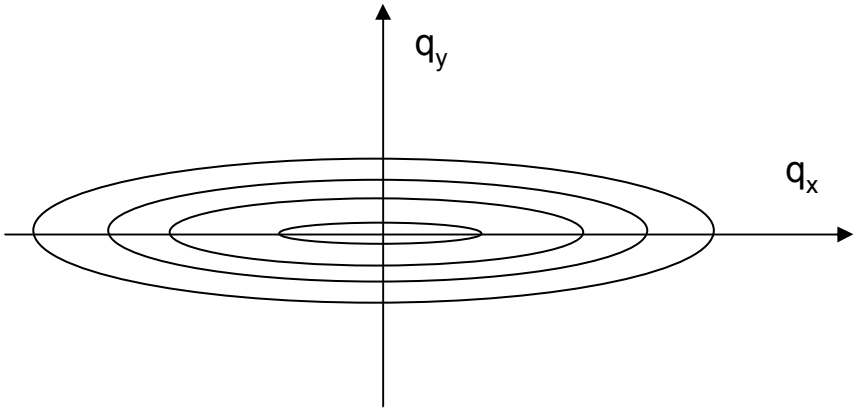

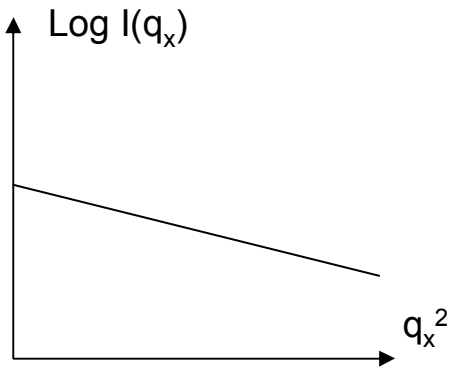

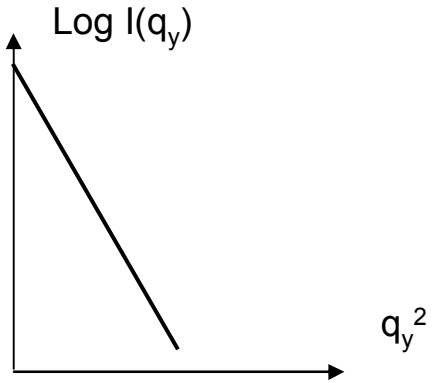

$$I_1(q_D) = N(\rho_1 - \rho_2)^2 V_1^2 e^{-R_D^2 . q_D^2}$$

$$R_D = \frac{1}{V}\int_V r_D^2 . d\vec{r} = \overline{r_D^2}$$

Dilute and isotropic system of very anisotropic nano-objects

$$qI(q) \propto e^{-\frac{1}{2}R_c^2 q^2}$$

$$q^2 I(q) \propto e^{-R_t^2 q^2}$$

$$R_t = T/\sqrt{12}$$

Dilute and isotropic system of polidispersed nano-objects

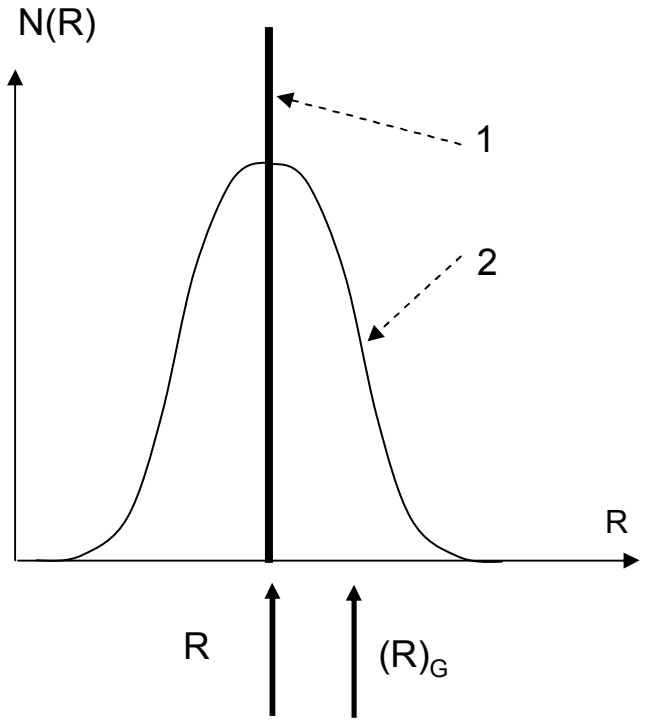

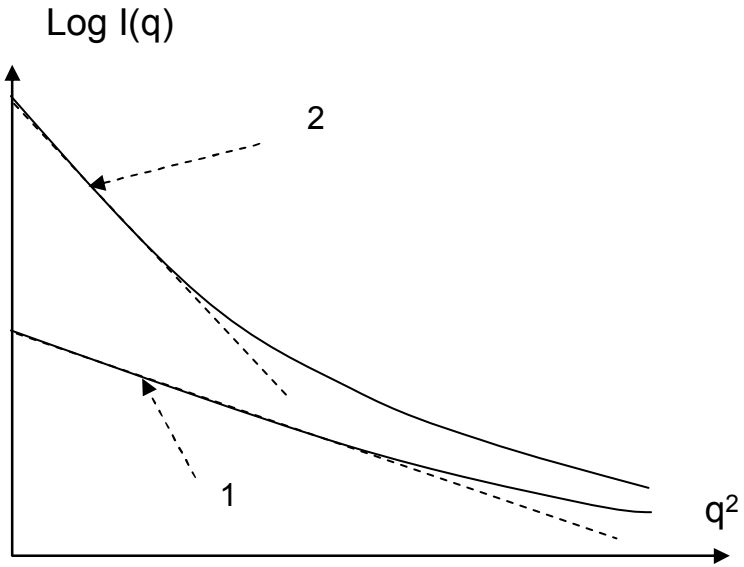

$$I(\vec{q}) = I_e(\rho_1 - \rho_2)^2 \int N(R_g)..V_1^2(R_g).e^{-\frac{R_g^2 q^2}{3}} dR_g$$

$$I(q) = NI_e(\rho_1 - \rho_2)^2 .\{V_1^2\} e^{-\frac{\{R\}_G^2 q^2}{3}}$$

$$I(q) = NI_e(\rho_1 - \rho_2)^2 \left[\frac{1}{N} \int N(R_g)..V_1^2(R_g).dR_g - \frac{q^2}{6N} \int N(R_g)..V_1^2(R_g).R_g^2 dR_g \right]$$

$$\{V_1^2\} = \frac{1}{N} \int N(R_g).V_1^2(R_g) dR_g$$

$$\{R\}_G = \left[\frac{1}{N} \int N(R_g).V_1^2 R_g^2 dR_g \right]^{1/2}$$

Spherical nano-objects embedded in a homogeneous matrix

$$I(q) = \int N(R).I_1(q,R)dR$$

$$I_1(q) = I_e(\rho_1 - \rho_2)^2 V_1 \int_0^R \left[1 - \frac{3r}{R} + \frac{1}{16}\left(\frac{r}{R}\right)^3\right] 4\pi.r^2 \frac{\sin qr}{qr} dr$$

$$\gamma_0(r) = 1 - \frac{3r}{R} + \frac{1}{16}\left(\frac{r}{R}\right)^3$$

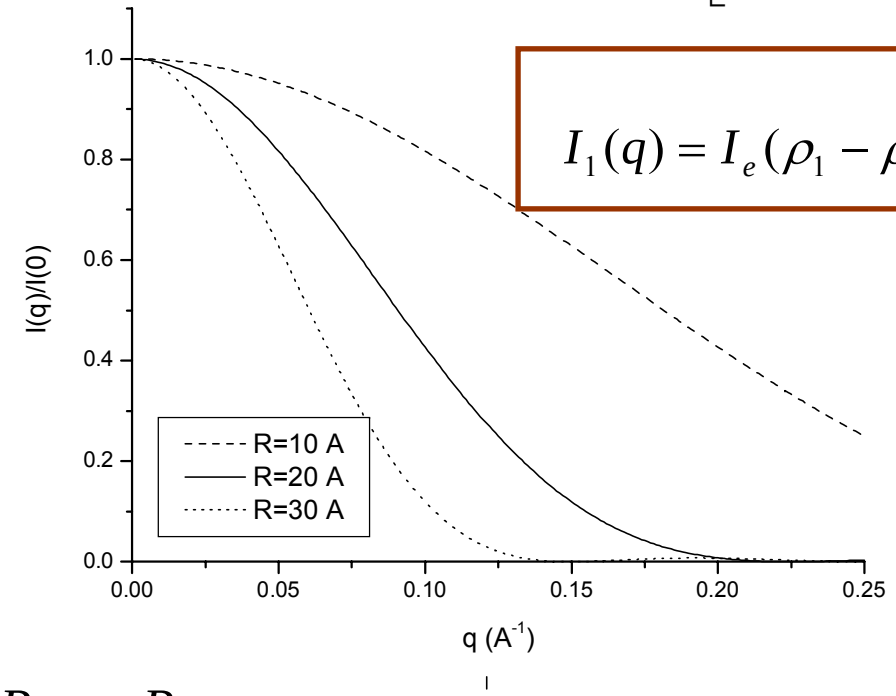

$$I_1(q) = I_e(\rho_1 - \rho_2)^2 . \left(\frac{4\pi R^3}{3}\right)^2 [\Phi(q)]^2$$

$$\Phi(q) = 3\frac{\sin qR - qR\cos qR}{(qR)^3}$$

$$I(q) = I_e(\rho_1 - \rho_2)^2 \left(\frac{4\pi}{3}\right)^2 \int N(R).R^6 \left[3\frac{\sin qR - qR\cos qR}{(qR)^3}\right]^2 dR$$

$$D(R) = \frac{4\pi}{3} R^3 .N(R)$$

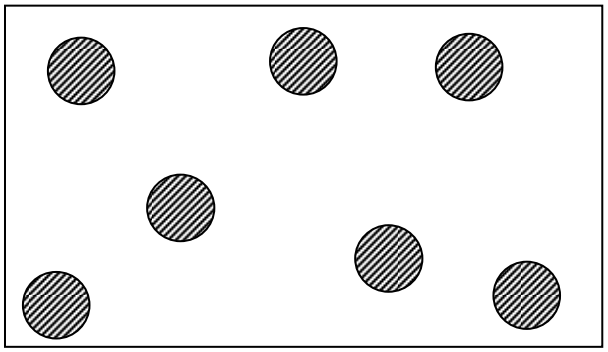

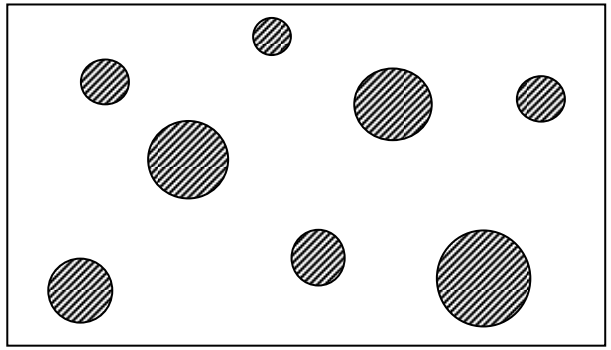

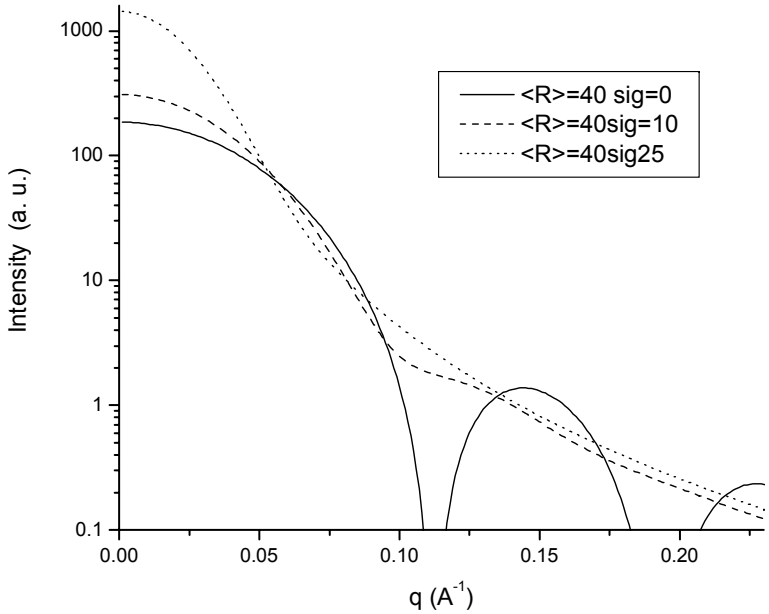
<R>=40 sig=0
<R>=40sig=10
<R>=40sig25
Intensity (a. u.)
1000
100
10
1
0.1
0.00
0.05
0.10
0.15
0.20
q (A-1)

$$I_1(q) = I_e\left[\sum_{i=1}^{n}(\rho_i - \rho_{i+1})\int_0^R 4\pi r^2 \frac{sin.qr}{qr}\right]^2$$

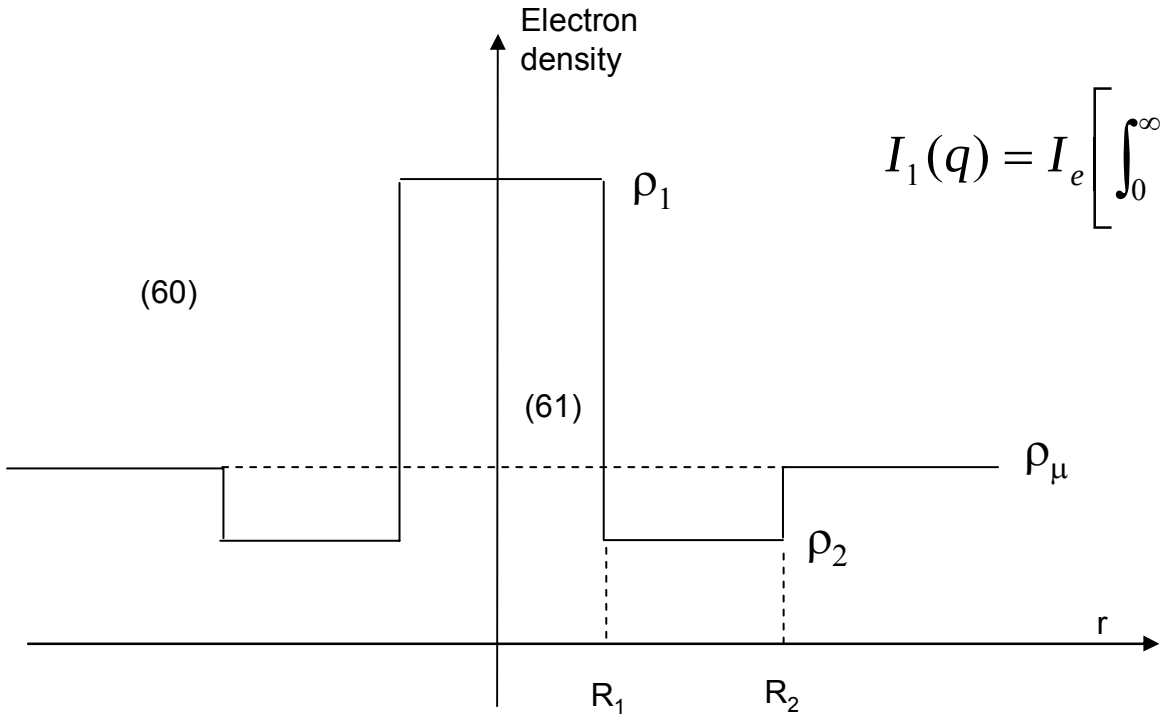

$$I_1(q) = I_e\left[\int_0^\infty 4\pi r^2 \rho(r)\frac{\sin q.r}{q.r}dr\right]^2$$

$$I_1(q) = I_e\left[\sum_{i=1}^{n}(\rho_i - \rho_{i+1})(4/3)\pi R_i^3 3\frac{sinqR_i - qR_1\cos qR_i}{(qR_i)^3}\right]^2$$

Nanoclusters of atoms. Debye equation

$$A_1(\vec{q}) = A_e \sum_{i=1}^{n} f_i(q) e^{-i\vec{q}.\vec{r}_i} \qquad I_1(\vec{q}) = I_e \sum_{i=1}^{n}\sum_{j=1}^{n} f_i(q) f_j(q) e^{-i\vec{q}(\vec{r}_i - \vec{r}_j)}$$

$$I(q) = N.I_1(q) = NI_e \sum_{i=1}^{n}\sum_{j=1}^{n} f_i(q) f_j(q) \frac{\sin q.r_{ij}}{qr_{ij}}$$

$$S_1(q) = \frac{1}{n}\sum_{i=1}^{n}\sum_{j=1}^{n} \frac{\sin q.r_{ij}}{qr_{ij}} = \left[1 + (1/n) \sum_{i,j(i\neq j)} \frac{\sin q.r_{ij}}{qr_{ij}}\right] \qquad I_1(q) = I_e n.f^2 S_1(q)$$

Polydispersed nano-objects with irregular shapes

$$I(q) = G.e^{-\frac{1}{3}R_g^2 q^2} + B.\left(\frac{1}{q^*}\right)^P \qquad q^* = \frac{q}{\left[erf\left(qR_g / 6^{1/2}\right)\right]}$$

$$I(q) = N(\rho_1 - \rho_2)^2 v^2 .e^{-\frac{1}{3}R_g^2 q^2} + 2\pi N(\rho_1 - \rho_2)^2 S.\left(\frac{1}{q^*}\right)$$

Small-angle scattering of a concentrated set of nano-objects
The hard sphere model

$$I(q) = NI_1(q)S(q)$$

$$S(q) = 1 + \frac{1}{V_p}\int_0^\infty [g(r) - 1] 4\pi r^2 \frac{\sin qr}{qr} dr$$

$$S(q) = 1 - 8\left(\frac{V_1}{V_p}\right)\Phi(qR)$$

$$\Phi(q) = 3\frac{\sin(qR) - 2qR\cos(qR)}{(qR)^3}$$

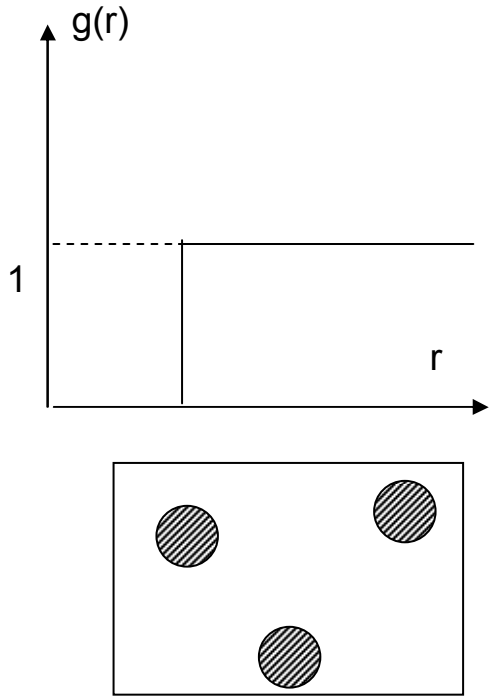

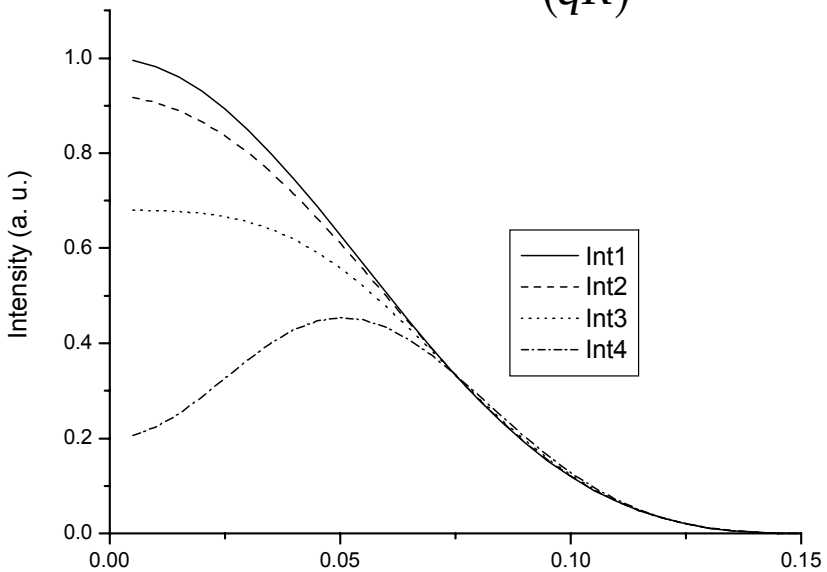

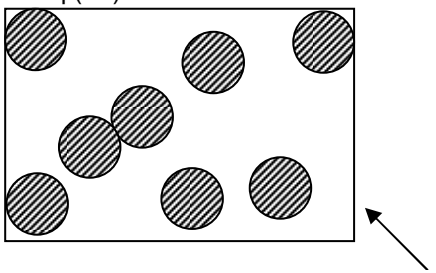

Spherical nano-objects embedded in a solid matrix

$$I(q) = N.I_1(q).S(q)$$

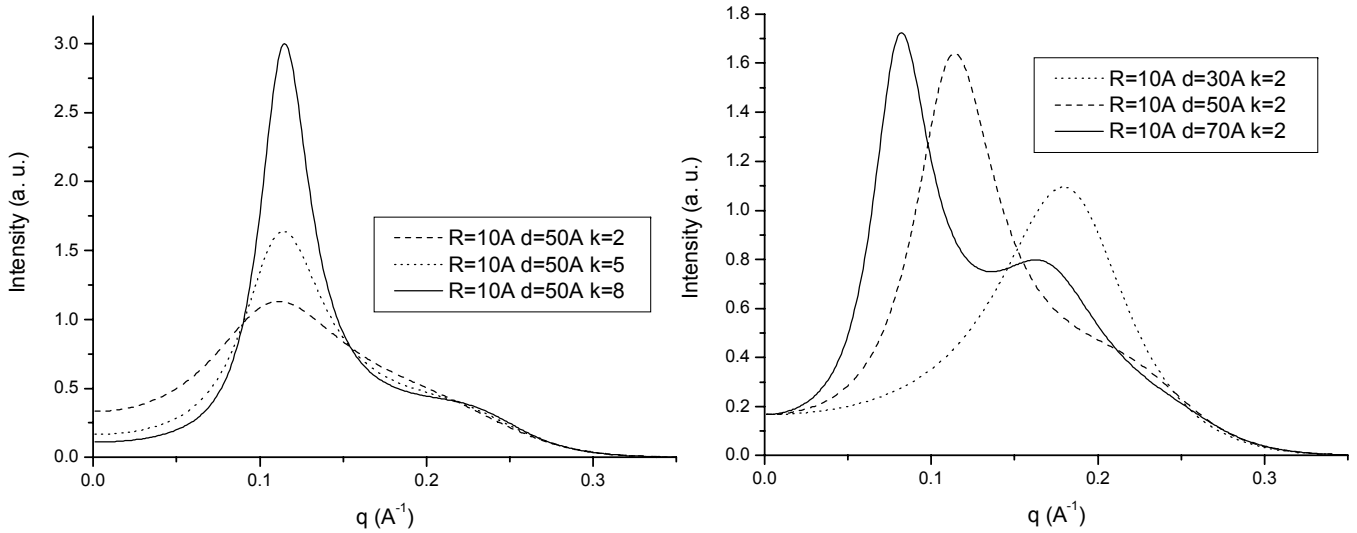

$$S(q) = \frac{1}{1 + k\Phi(qd)}$$

$$\Phi(qd) = 3\frac{\sin(qd) - qd\cos(qd)}{(qd)^3}$$

$$d = \frac{2\pi}{q_{\max}}$$

(79)

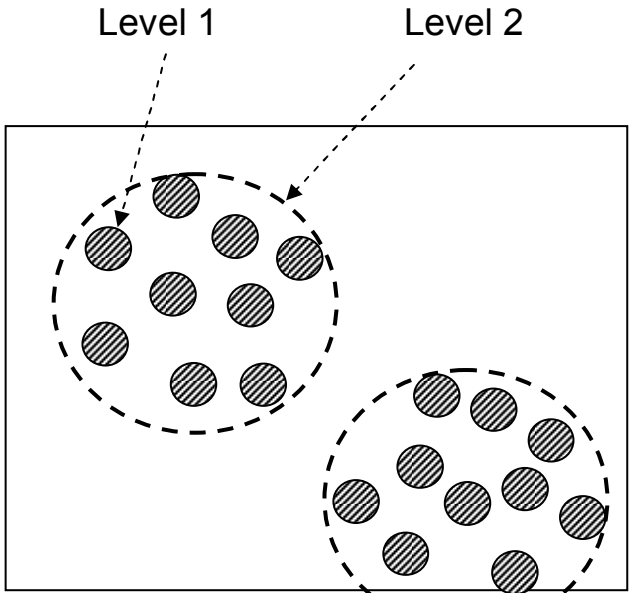

(80)

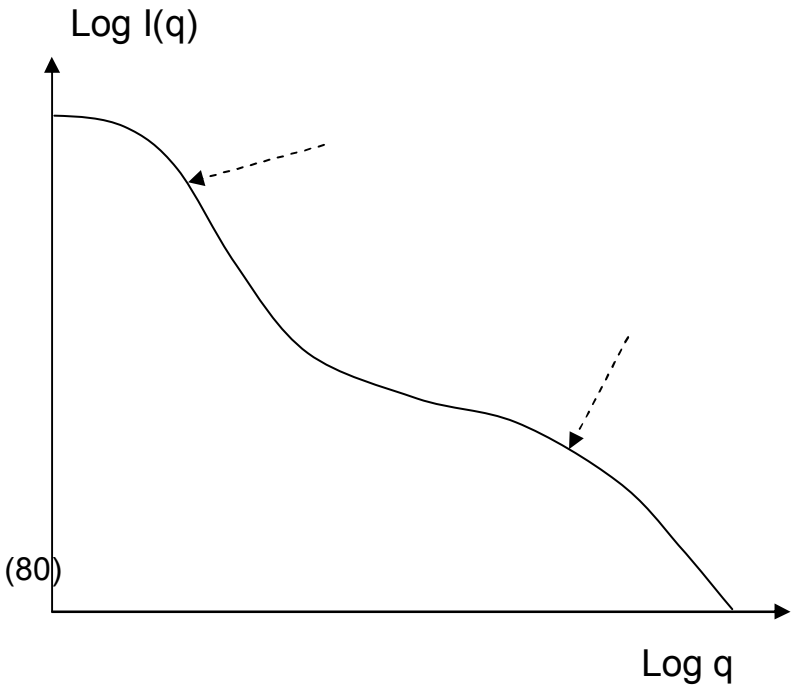

$$I(q) = \left[G_1 . e^{-\frac{1}{3} R_{g1}^2 q^2} + B_1 . e^{-\frac{1}{3} R_c^2 q^2} \left\{ \left[erf\left(qR_{g1} / 6^{1/2} \right) \right]^3 / q \right\}^4 \right] . + . \left[G_2 . e^{-\frac{1}{3} R_{g2}^2 q^2} + B_2 . \left\{ \left[erf\left(qR_{g2} / 6^{1/2} \right) \right]^3 / q \right\}^4 \right]$$

$$I(q) = \sum_{i=1}^{n} \left[G_i . e^{-\frac{1}{3} R_{gi}^2 q^2} + B_1 . e^{-\frac{1}{3} R_{g(i+1)}^2 q^2} \left\{ \left[erf\left(qR_{gi} / 6^{1/2} \right) \right]^3 / q \right\}^4 \right]$$

Spinodal decomposition

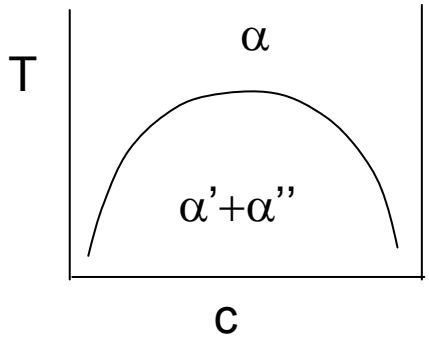

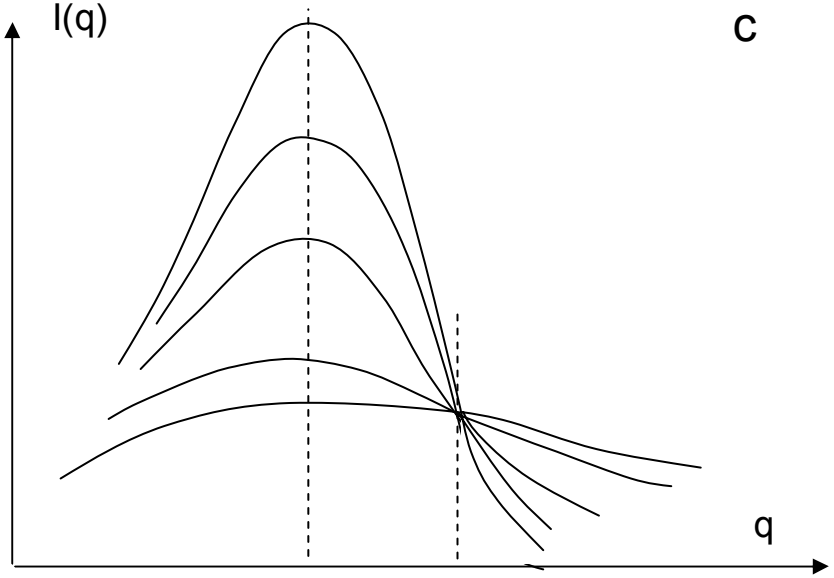

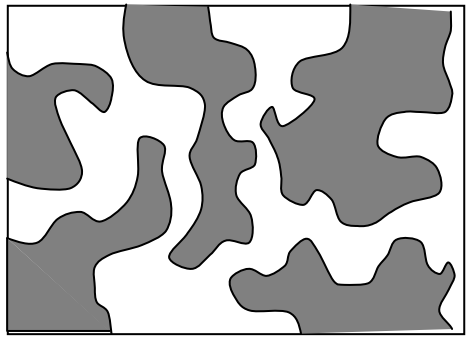

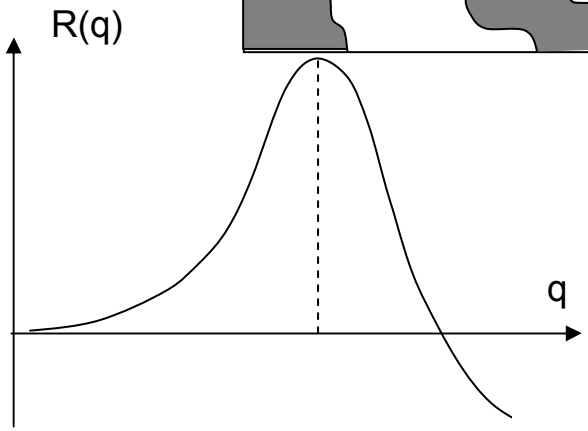

$$I(q,t) = I(q,0).e^{2R(q)t}$$

$$q_c = \sqrt{2}.q_m$$

Nanophase separation and dynamical scaling property.

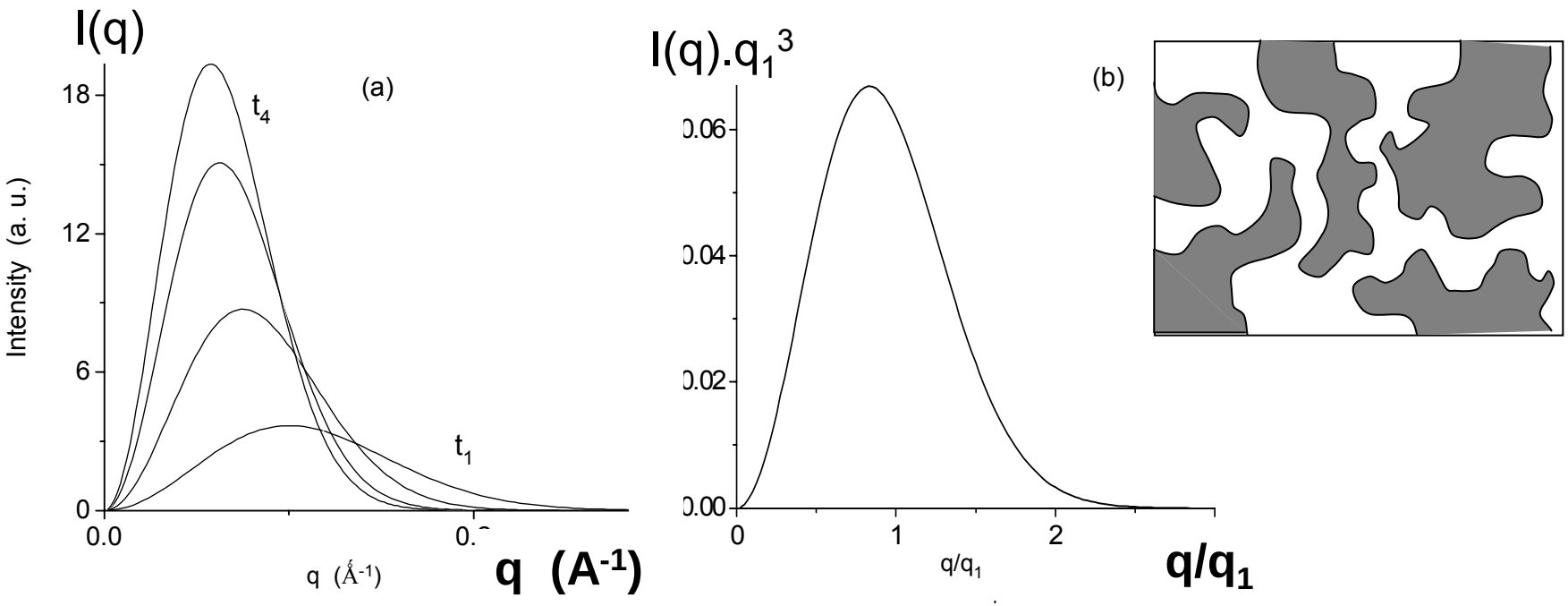

$$I(q,t) = N.I_1(q).S(q.t) \propto S(q,t)$$

$$q_n(t) = \left[\frac{\int_0^\infty q^n(t).I(q,t)dq}{\int_0^\infty I(q,t)dq} \right]^{1/n}$$

$$F(x) = I(q,t).[q_1(t)]^3$$

a) Different scattering intensity curves from a system in advanced stages of nanophase separation, for increasing periods of isothermal annealing from t_1 to t_4. (b) Scaled structure function.

Fractals

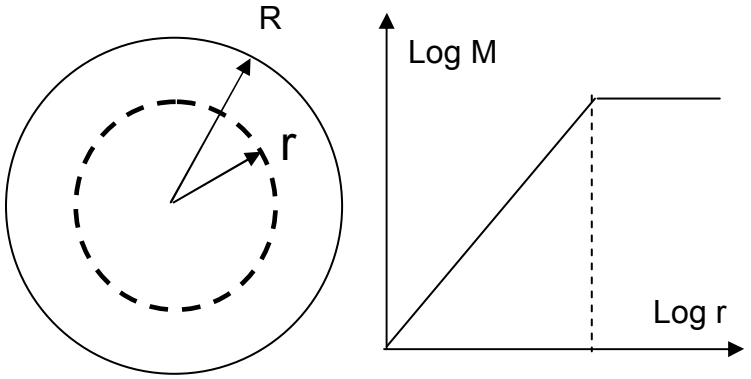

Homogeneous object Slope 3

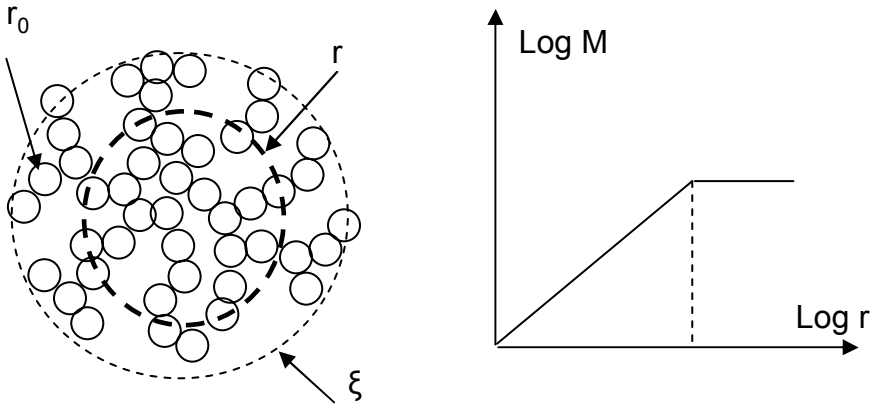

Fractal object Slope D

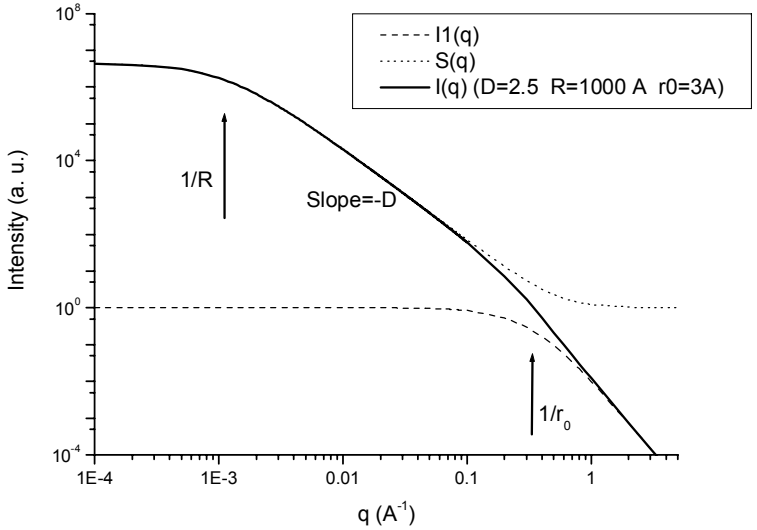

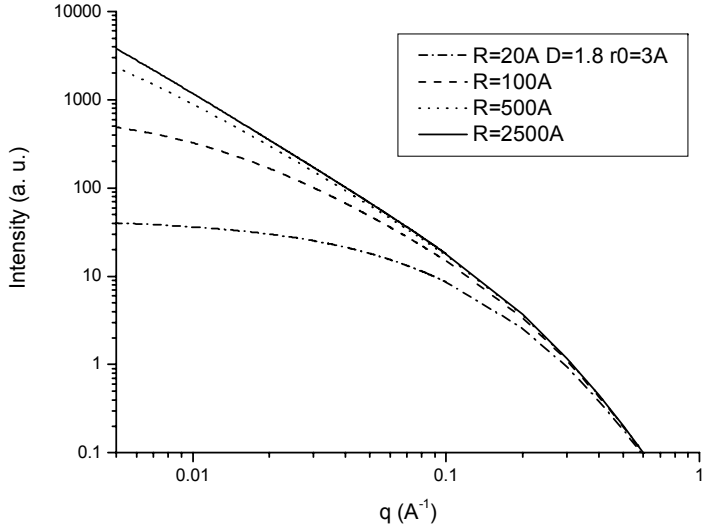

$$\frac{M}{V} = \rho$$

$$M = \rho V = Kr^3$$

$$\log M = A + 3\log r$$

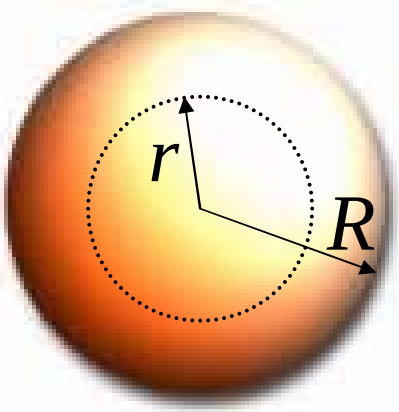

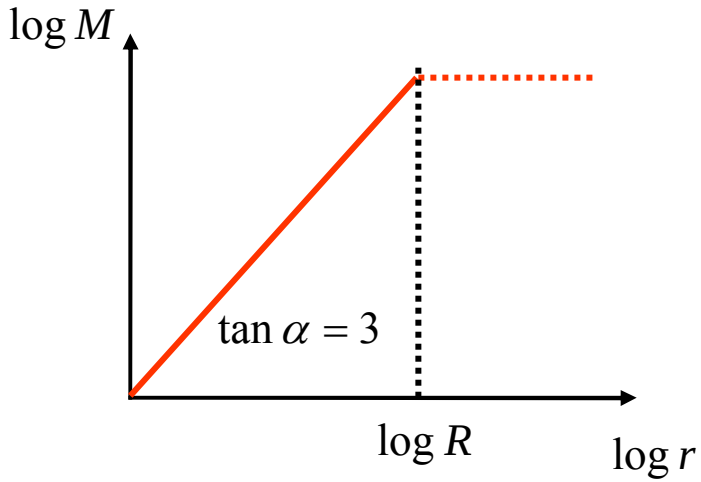

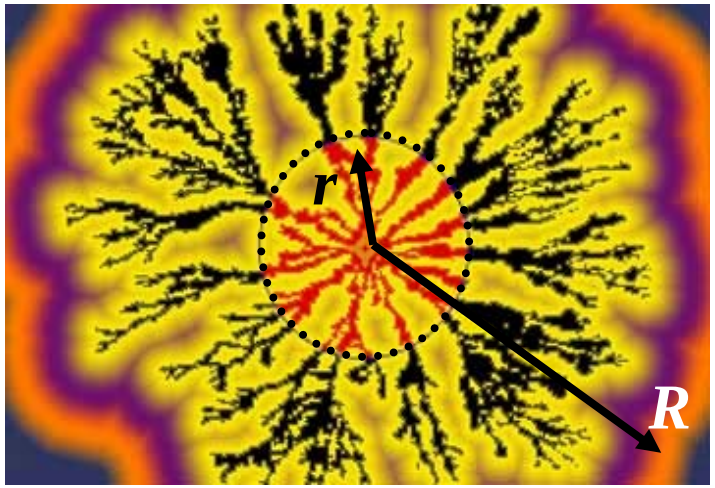

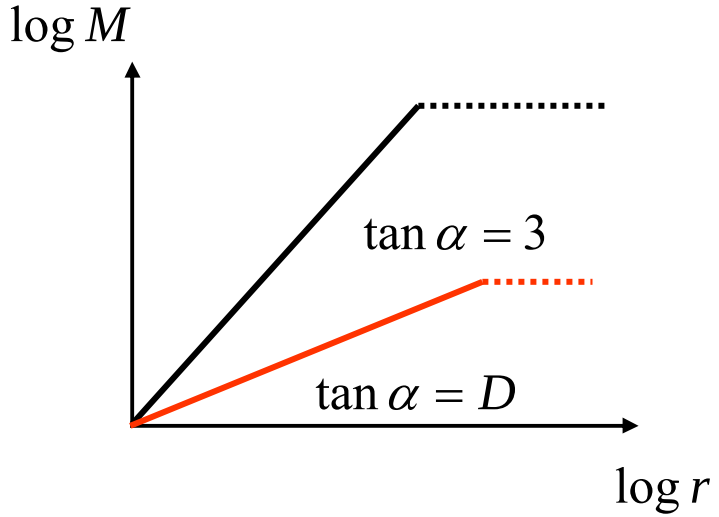

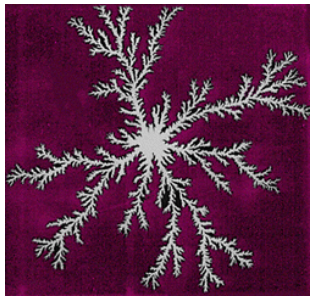

$$M = Kr^D$$

$$\log M = K + D\log r$$

Determination of the fractal dimension in real space

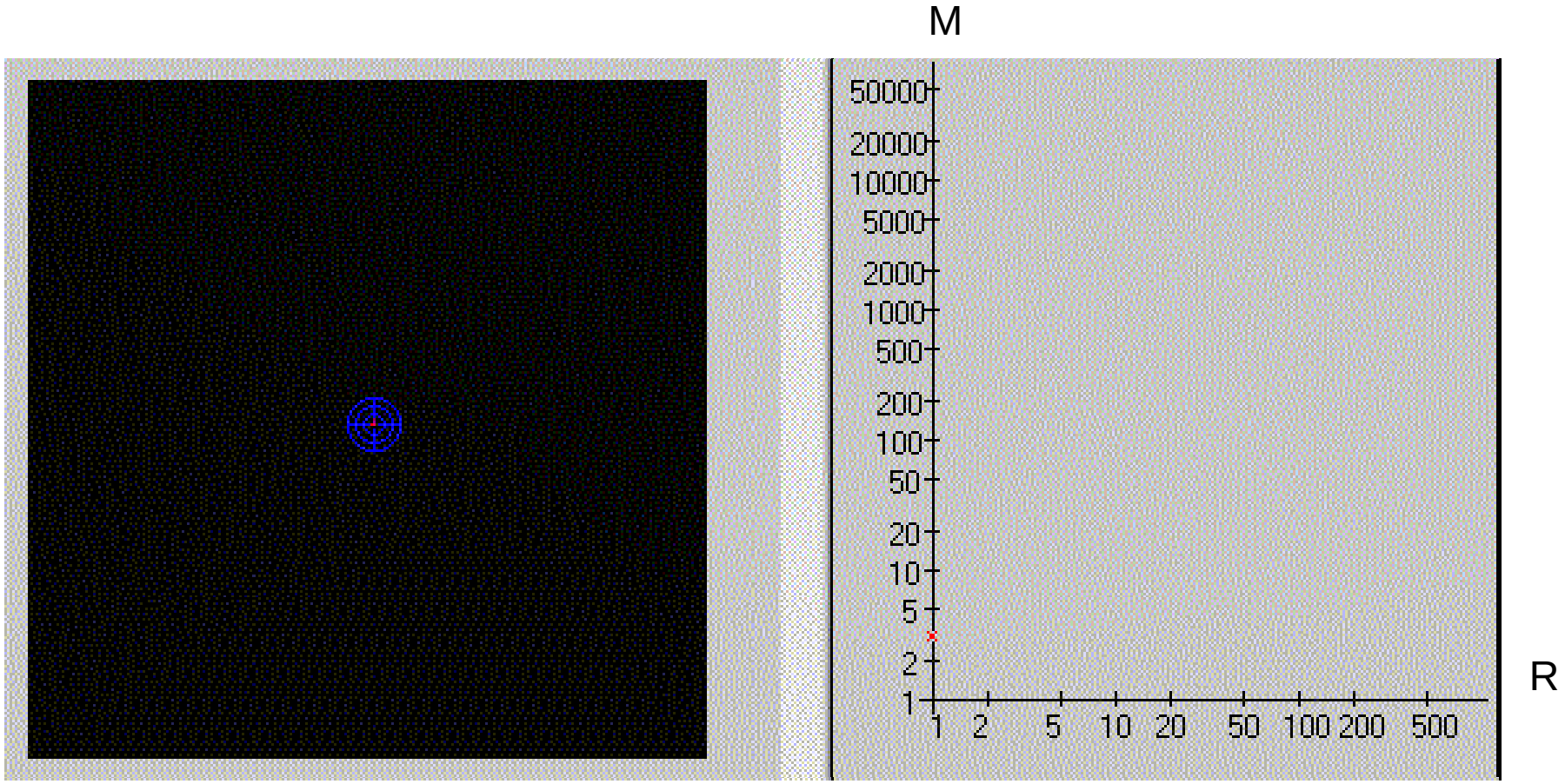

movie

$$M = \rho.V = a.R^2$$

$$\log M = \log a + 2.\log R$$

Determination of the fractal dimension in real space

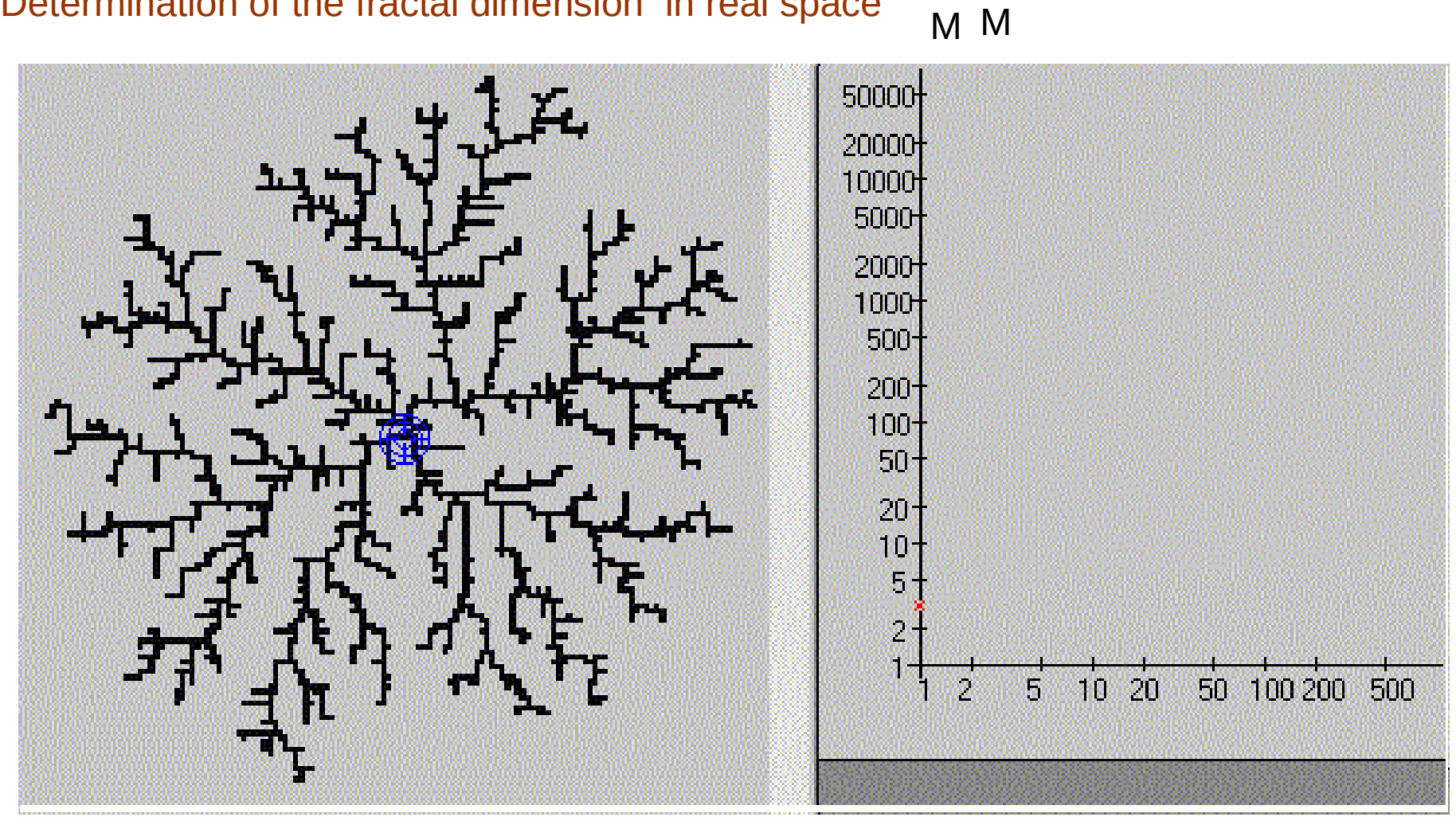

movie

$$M = \rho.V = a.R^D$$

$$\log M = \log a + D.\log R$$

Aggregation of colloidal particles
Models of growth and results of calculations of the fractal dimension using computer simulation

Mechanism of growth	Fractal dimension (3D)	Fractal dimension (2D)
Eden		2
Witten Sanders	2.45	1.65-1.70
Witten Sanders linear trajectory	2.97	1.92-1.95
Tip-to-tip	1.43	1.26
Self-avoiding walk	1.66	1.33
Cluster-cluster random walk	1.75-1.80	1.44-1.48
Cluster-cluster ballistic	1.81-1.95	1.50-1.54
Ideal linear polymer	2.00	
Swollen linear polymer	1.66	
Ideal branched polymer	2.16	
Dense particle	3.00	
Diffusion limited cluster-cluster aggregation (DLCA)	1.78	
Reaction limited cluster-cluster aggregation (RLCA)	2.11	

$$N(r) = \left(\frac{r}{r_0}\right)^D$$

$$\frac{N}{V} g(r) = \frac{N}{V} + \left(\frac{D}{4\pi r_0^D} r^{D-3}\right) e^{-r/\xi}$$

$$S(q) = 1 + \frac{D}{r_0^D} \int_0^\infty r^{D-1} e^{-\frac{r}{\xi}} \frac{\sin qr}{qr} dr$$

$$I(q) = \frac{A}{\left(1 + r_0^2 q^2\right)^2}$$

$$S(q) = 1 + \frac{1}{\left(qr_0\right)^D} \frac{D.\Gamma(D-1)}{\left[1 + 1/(q^2\xi^2\right]^{(D-1)/2}} \sin\left[(D-1)\tan^{-1}(q\xi)\right]$$

$$I(q) = \frac{A}{\left(1 + r_0^2 q^2\right)^2} . \left\{1 + \frac{1}{\left(qr_0\right)^D} \frac{D.\Gamma(D-1)}{\left[1 + 1/(q^2\xi^2)\right]^{(D-1)/2}} \sin\left[(D-1)\tan^{-1}(q\xi)\right]\right\}$$

$$I(0) = \Gamma(D+1) . \left(\frac{\xi}{r_0}\right)^D$$

For particles: ξ~Rg

$$S(q) = S(0)\left\{1 - \left[\frac{D(D+1)}{6}\right]\xi^2 q^2\right\} \cong S(0).e^{-\frac{R_g^2 q^2}{3}}$$

$$R_g = \left[\frac{D(D+1)}{2}\right]^{1/2} \xi$$

$$1/\xi << q << 1/r_0$$

$$I(q) \propto q^{-D}$$

Determination of the fractal dimension from results of SAS experiments

$$I(q) = N I_1(q) S(q)$$

$$S(q) = 1 + \frac{1}{(r_0 q)^D} \frac{D\Gamma(D-1)\cdot\sin\left[(D-1)\cdot\tan^{-1}(q\xi)\right]}{\left[1+\frac{1}{(\xi q)^2}\right]^{(D-1)/2}}$$

$$I_1(q) = \frac{A}{\left[1+(r_0 q)^2\right]^2}$$

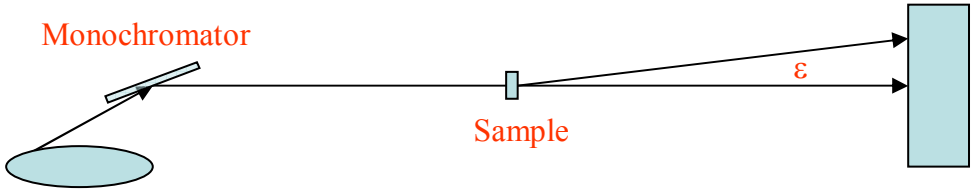

$q = (4\pi/\lambda)\sin(\varepsilon/2)$
for small ε: $q = (2\pi/\lambda)\varepsilon$

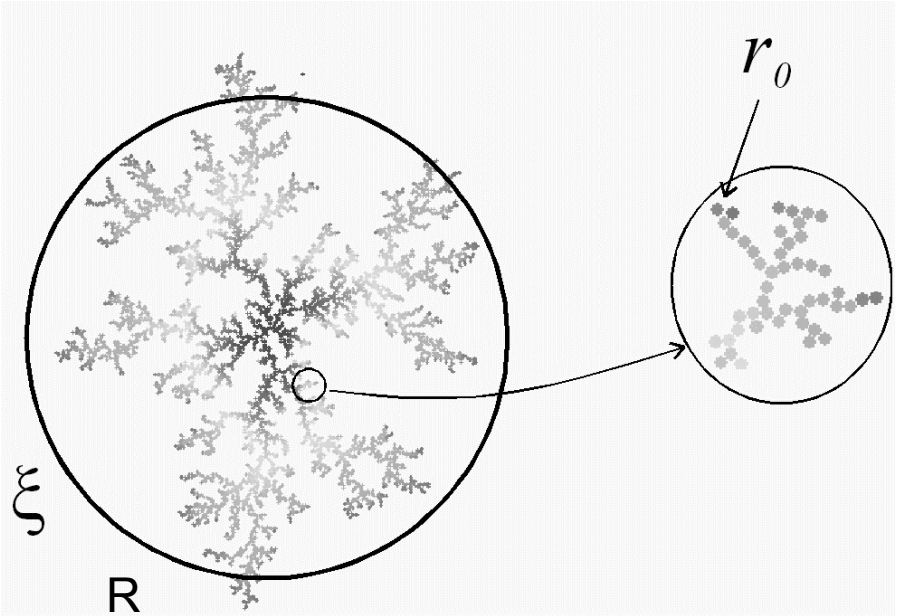

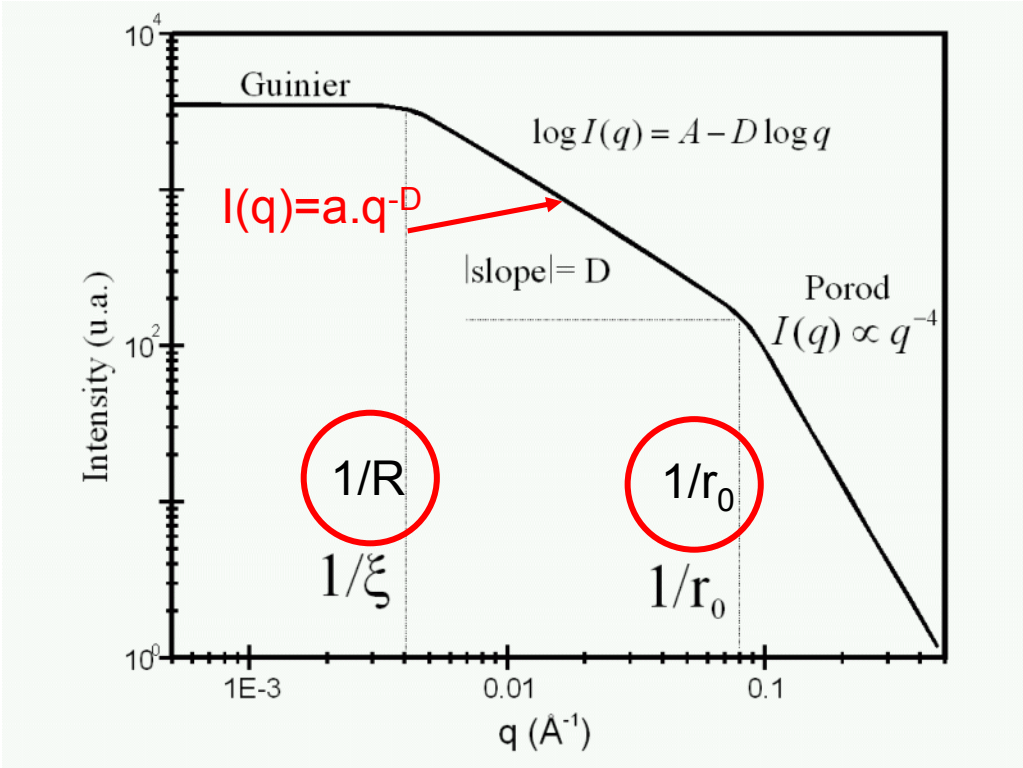

Effects on SAXS curves by the variation of D from 1.8 up to 2.5

$$I(q)=NI_1(q)S(q)$$

D

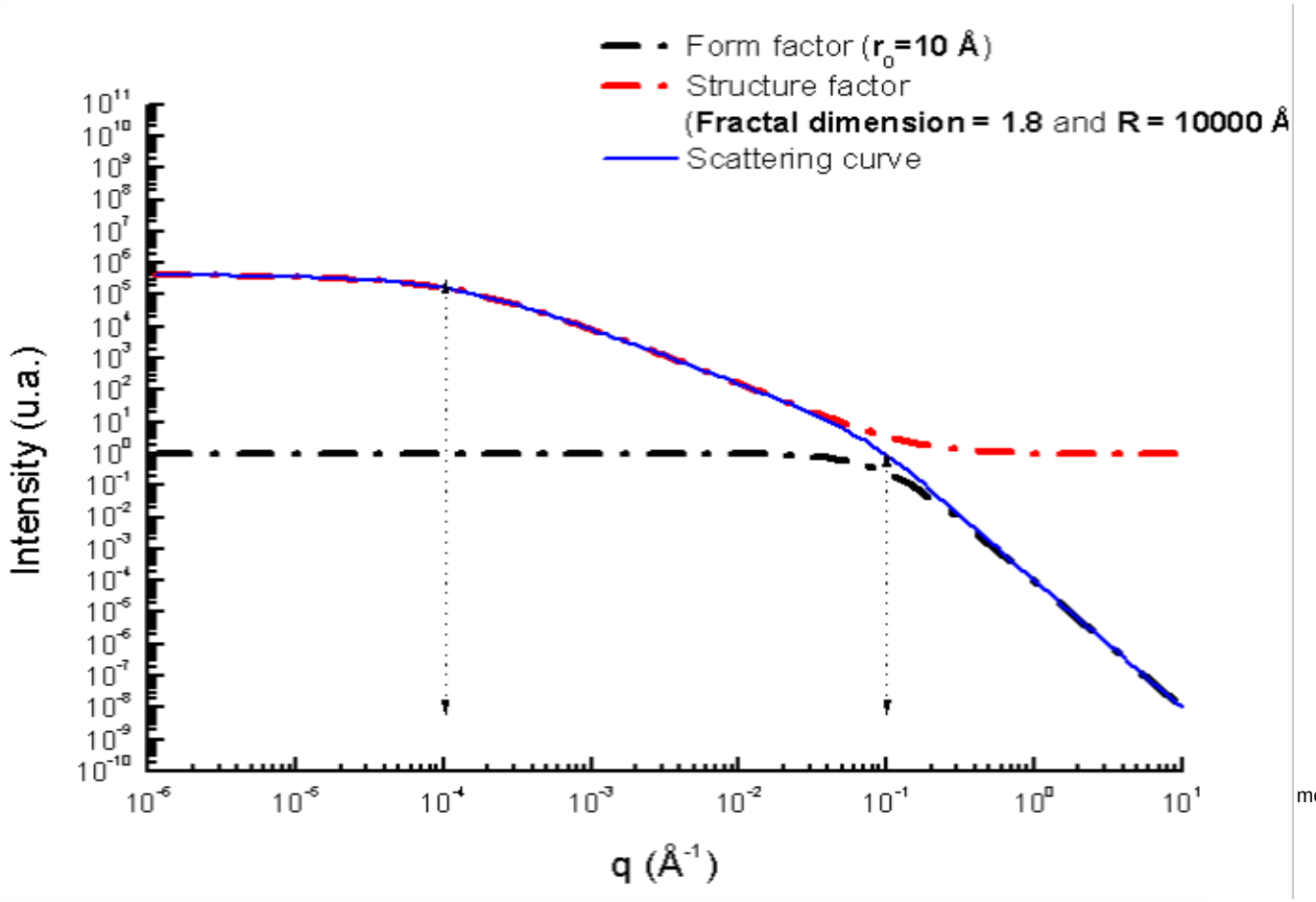

movie

1/R

1/r_o

Effects on SAXS by the variation of the overall size of the aggregate from 1000 up to 500000Å

$$I(q)=NI_1(q)S(q)$$

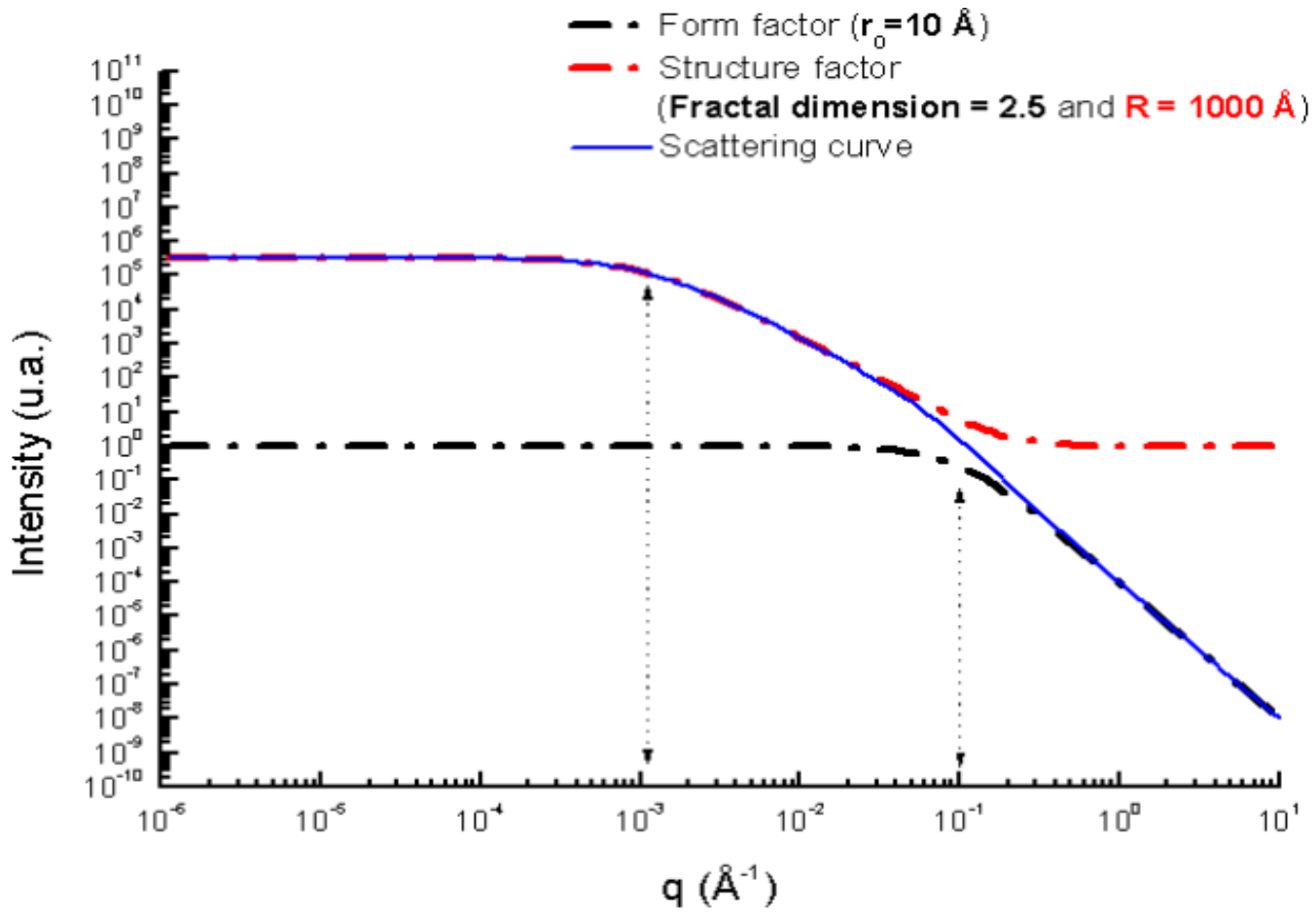

movie

1/R

1/r_o

Effects on SAXS curves produced by the variation of the size of the building block units (r_0) from 100 Å down to 1 Å

$$I(q)=NI_1(q)S(q)$$

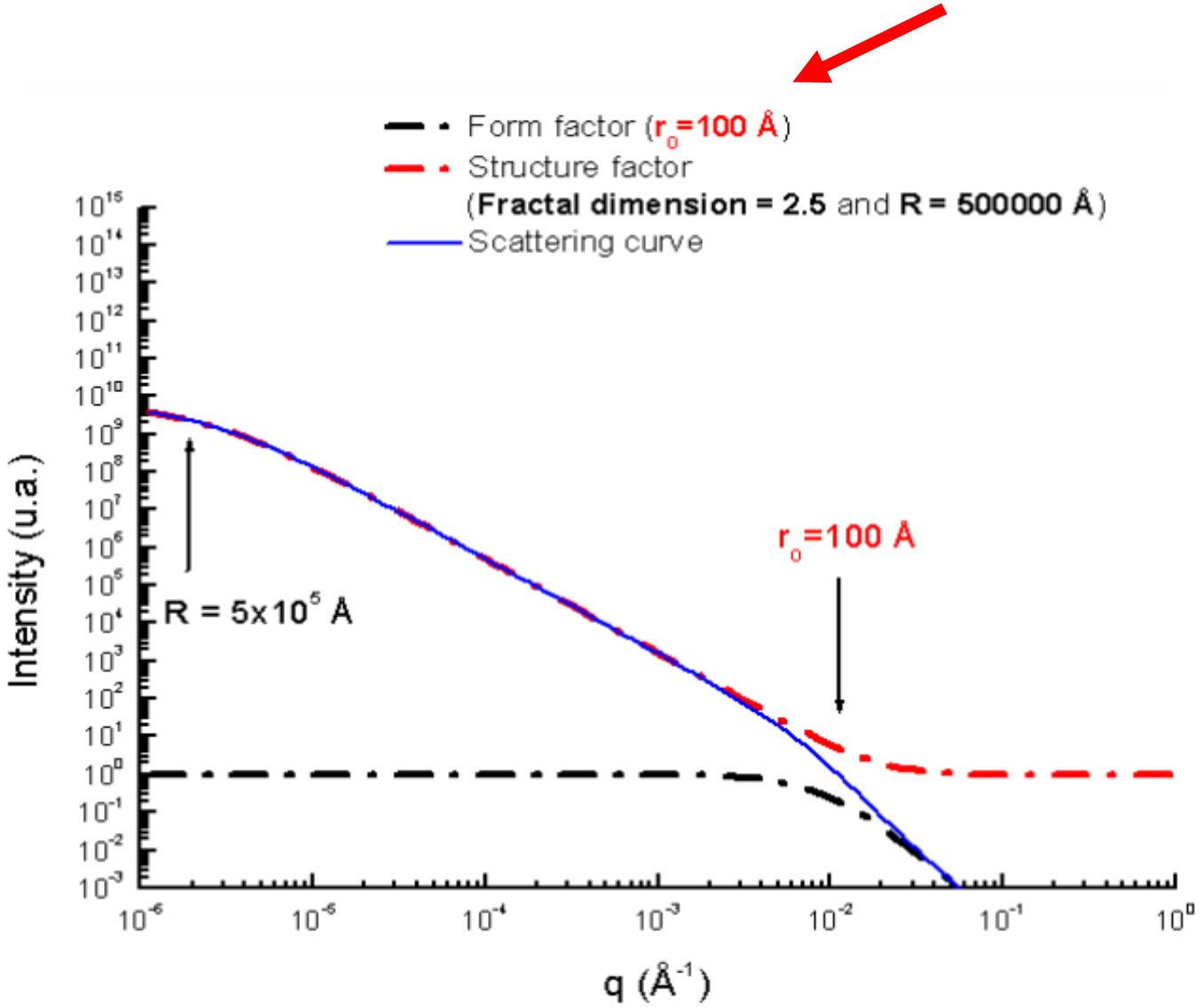

movie

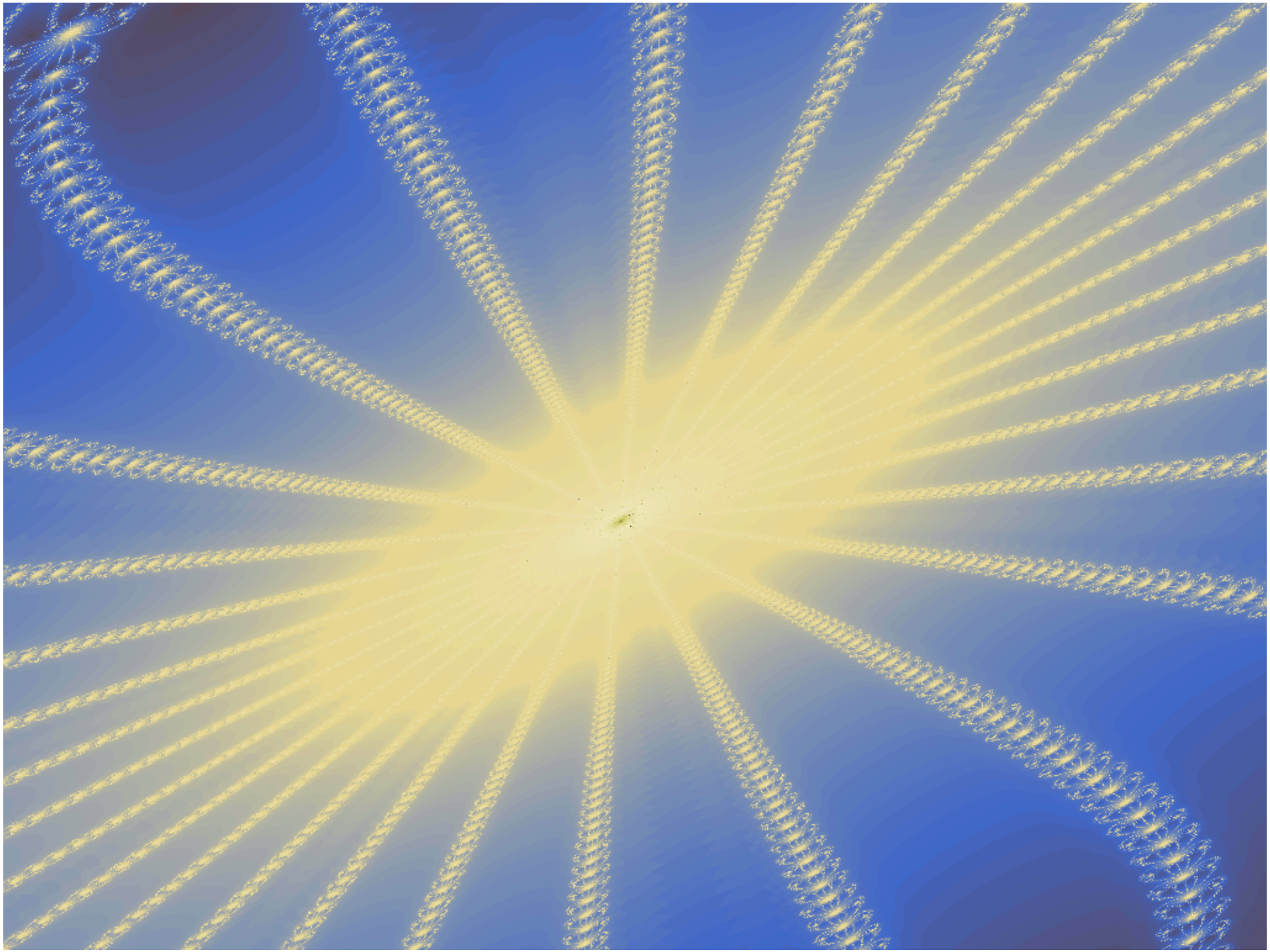

Proteins in solution (D. Svergun)

- Restauration of structural models *ab initio* using only results of small-angle scattering experiments
- Characterization of proteins in solution using SAXS and (high resolution) crystallographic data obtained by single crystal XRD
- Example of application: Phosphoenolpyruvate carboxykinase (PEPCK)

Bead models

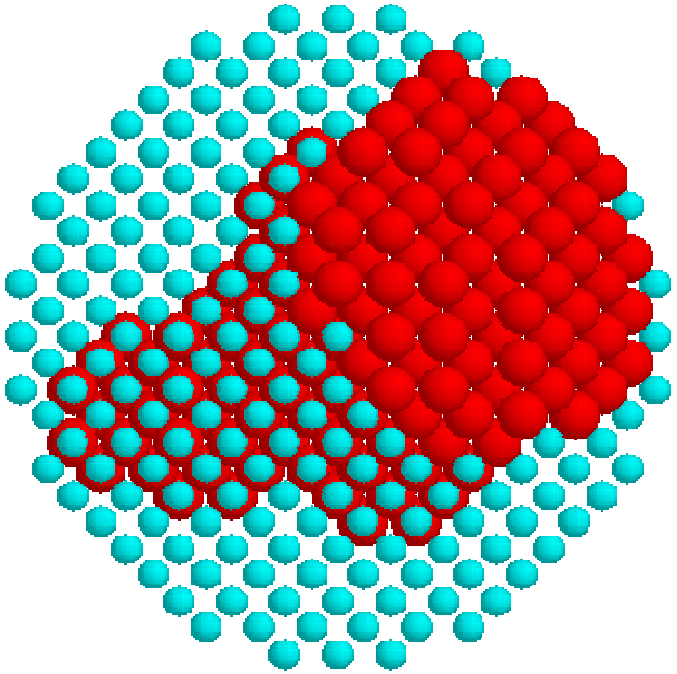

Position(j) = X(j) = 1 or 0

- $M \approx (D_{max}/r_0)^3 \approx 10^3 >> N_s$ parameters, too many for conventional minimization
- No unique shape restoration unless constrained
- Able to describe complex shapes

Chacón, P. *et al.* (1998) *Biophys. J.* **74,** 2760-2775.

Svergun, D.I. (1999) *Biophys. J.* **76**, 2879-2886

Ab initio program DAMMIN

Using simulated annealing, finds a compact dummy atoms configuration X that fits the scattering data by minimizing

$$f(X) = \chi^2[I_{\exp}(s), I(s, X)] + \alpha P(X)$$

where χ is the discrepancy between the experimental and calculated curves, *P(X)* is the penalty to ensure compactness and connectivity, $\alpha > 0$ its weight.

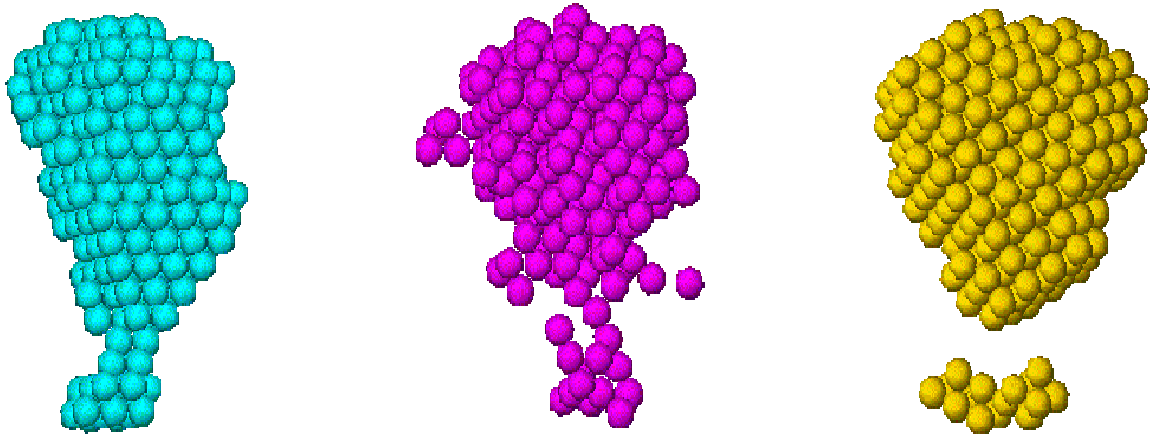

compact

loose

disconnected

Local and global search

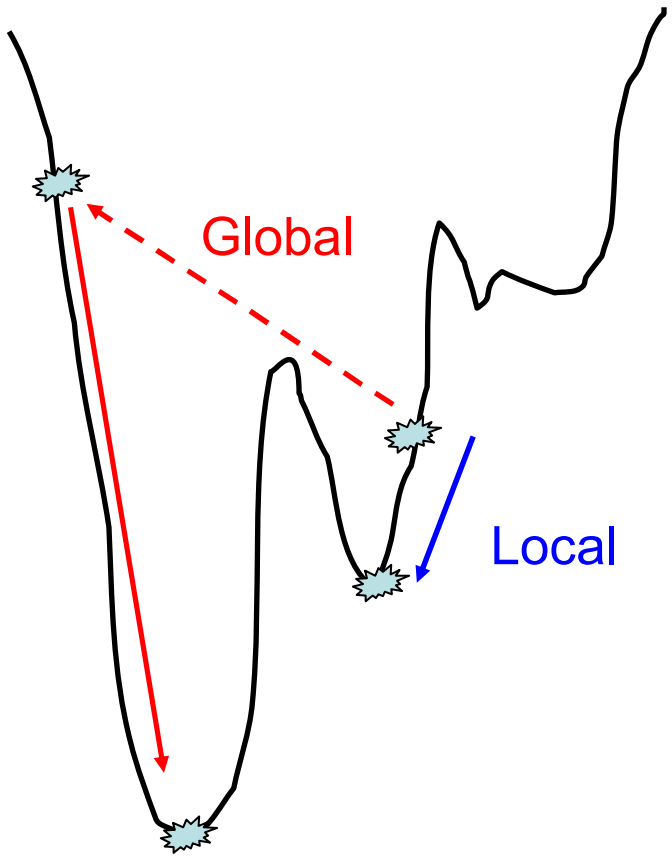

- Local search always goes to a better point and can thus be trapped in a local minimum
- To avoid local minima, global search must be able go to a worse point

Simulated annealing

Aim: find a configuration of *M* variables *{x}* minimizing a function *f(x)* of these variables.

1. **Start from a random configuration *x* at a "high" temperature *T*.**
2. **Make a small step (random modification of the configuration) *x* $\rightarrow$ *x'* and compute the difference $\Delta = f(x') - f(x)$.**
3. ***If* $\Delta < 0$, accept the step; if $\Delta > 0$, accept it with a probability $e^{-\Delta/T}$**
4. ***Make another step from the old (if the previous step has been rejected) or from the new (if the step has been accepted) configuration.***
5. ***Anneal the system at this temperature, i.e.* repeat steps *2-4* *"many"***
   (say, 100M* tries or *10M* successful tries, whichever comes first) times,then decrease the temperature *(T' = cT, c<1).
6. ***Continue cooling the system until no improvement in f(x)* is observed.**

A shape determination movie

- The next slides present the shape determination of the myosin head subfragment S1
- The evolution of the dummy atoms configuration is displayed of the right (only particle atoms are shown), the fit to the experimental data is illustrated on the left
- The scattering data are provided by B.Mendelson (USCF)

S1 shape reconstruction

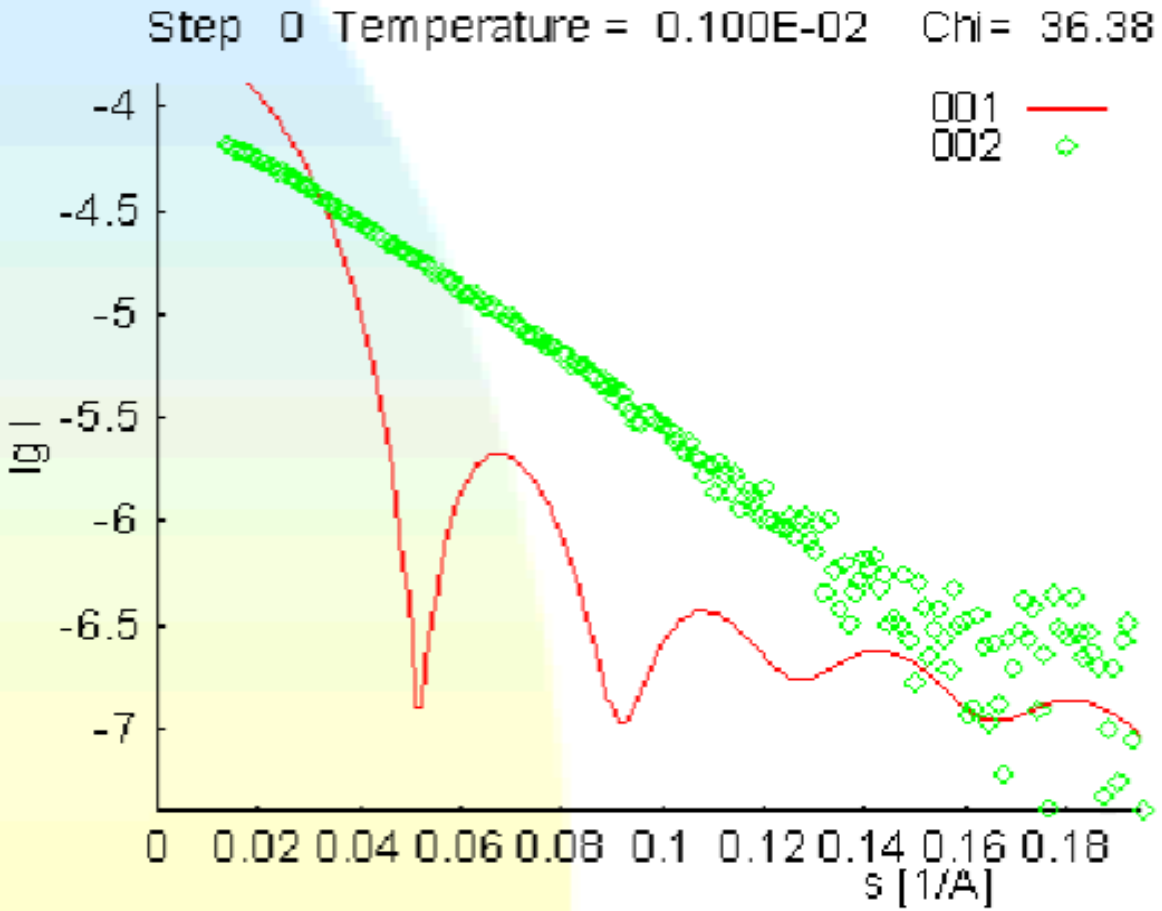

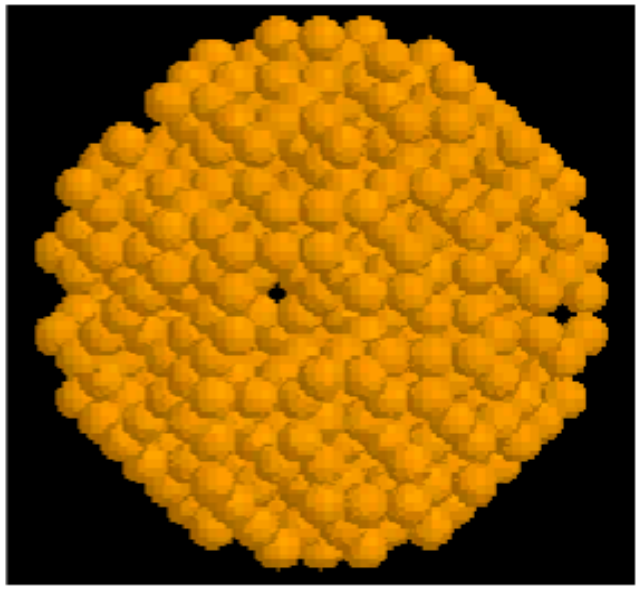

movie

S1 shapes restored by *DAMMIN*

Red: atomic model

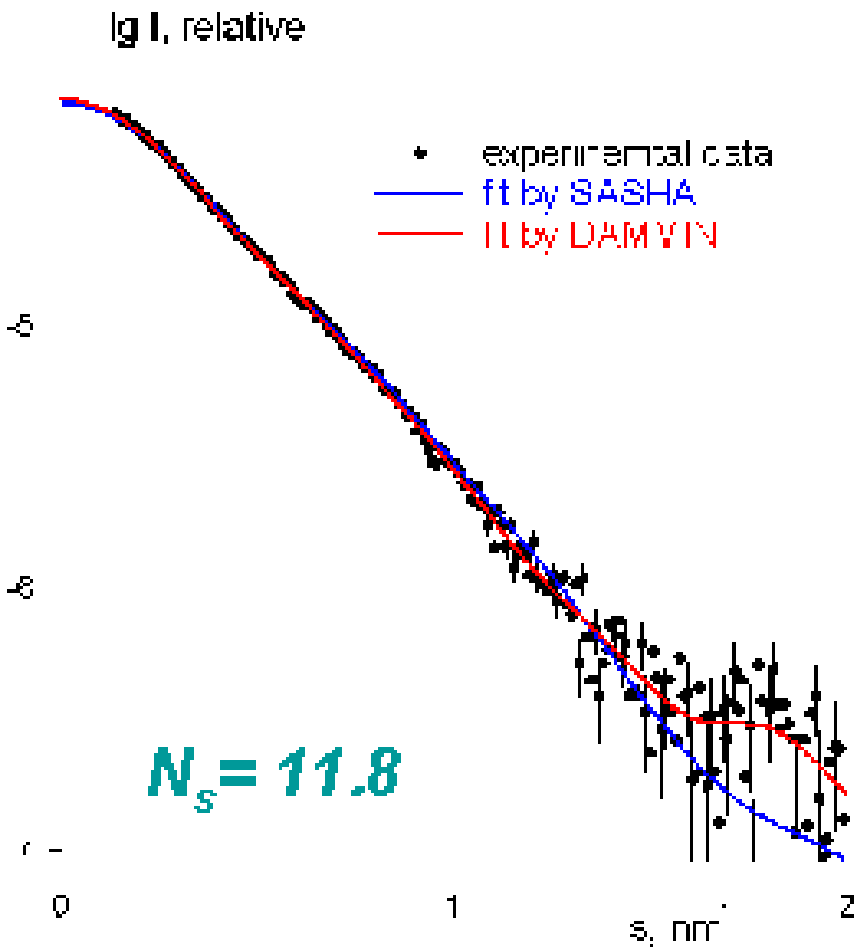

$N_s = 11.8$

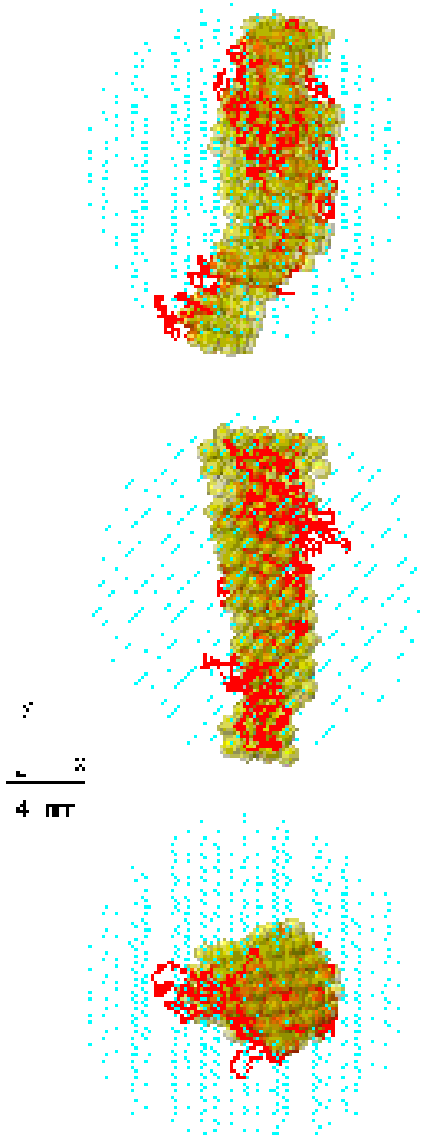

Number of parameters: M=2729

SAXS. Basic Aspects

Aldo F. Craievich

Institute of Physics

University of São Paulo

Brazil

(craievich@if.usp.br)